JIMMA UNIVERSITY

JIMMA INSTITUTE OF TECHNOLOGY

SCHOOL OF GRADUATE STUDIES

FACULTY OF MECHANICAL ENGINEERING

SUSTAINABLE ENERGY ENGINEERING STREAM

Design of a small-scale solar-stirling power system with a beam-down focus for rural electrification.

A Thesis submitted to the School of Graduate Studies of Jimma Institute of Technology, in partial fulfillment of the requirement for the degree of Master of Science in Sustainable Energy Engineering

By:

Oda Tadese

June 2023

Jimma, Ethiopia

JIMMA UNIVERSITY

JIMMA INSTITUTE OF TECHNOLOGY

SCHOOL OF GRADUATE STUDIES

FACULTY OF MECHANICAL ENGINEERING

SUSTAINABLE ENERGY ENGINEERING STREAM

Design of a small-scale solar-stirling power system with a beam-down focus for rural electrification.

By:

Oda Tadese

A Thesis submitted to the School of Graduate Studies of Jimma Institute of Technology, in partial fulfillment of the requirement for the Degree of Master of Science in Sustainable Energy Engineering

Principal Advisor: Prof. A.Venkata Ramayya (Ph.D.)

Co-advisor: Eshetu Tadese (MSc.)

June 2023

Jimma, Ethiopia

DECLARATION

I, the undersigned, declare that this thesis entitled ” Design of a small-scale solar-stirling power system with a beam-down focus for rural electrification.” is my original work and has not been presented for a degree in any University and that all the source of materials used for the thesis has been duly acknowledged.

Oda Tadese Katelo	_____	_____
Name	Signature	Date

As research Adviser, I certify this thesis paper prepared by Oda Tadese Katelo, entitled “Design of a small-scale solar-stirling power system with a beam-down focus for rural electrification.” and recommend and would be accepted as a fulfilling requirement for the Degree Master of Science in sustainable energy.

Prof. A. Venkata Ramayya (Ph.D.)	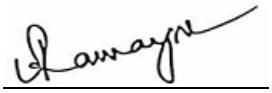	16-09-2023
Advisor	Signature	Date
Eshetu Tadesse (MSc.)		14-09-2023
Co-advisor	Signature	Date

The thesis has been submitted for the examination with my approval as University advisor.

APPROVAL

As members of the Examining Board of The Final MSc, Open Defense, We certify that we have read and evaluated the Thesis Prepared by: Oda Tadese entitled: Design of small scale solar-stirling power system with a beam-down focus for rural electrification. We recommend that it be accepted as fulfilling the Thesis requirement for the Degree of Master of Science in Sustainable energy engineering.

Prof. A. Venkata Ramayya (Ph.D.)		16-09-2023
Advisor	Signature	Date
Eshetu Tadesse (MSc.)		14-09-2023
Co-advisor	Signature	Date
Tarekegn Limore (MSc.)		
SEE chair	Signature	Date
Dr. Addisu Bekele		Sep. 05, 2023
External Examiner	Signature	Date
Sewagegn Tarekegn		Sep 15 | 2023.
Internal Examiner	Signature	Date

Final approval and acceptance of the Thesis are contingent upon the submission of the final copy of the Thesis to the Council of Graduate Studies (CGS) through the Departmental Graduate Committee (DGC) of the candidate's major Department.

ACKNOWLEDGMENT

Above all, I would like to acknowledge the almighty God for his unlimited grace, mercy, and protection throughout my life. Next, I am pleased to express my deepest gratitude to my advisor, Prof. A. Venkata Ramayya (Ph.D.), for his positive attitude, continuous support, encouragement, and excellent supervision. He has been a source of inspiration, and it was a great experience to work with him; I would also like to thank my co-advisor Mr. Eshetu Tadese (MSc.), for his guidance and encouragement. And all sustainable energy engineering staff members who were beside me, I said thank you!

Finally, I would like to extend my special thanks to my family and all my friends for their entire support and encouragement. Unless in their support, it would have been impossible for me to achieve this work.

ABSTRACT

In Ethiopia, off-grid rural electrification using renewable energy is a highly attractive energy option as a result of the scattered settlement of rural populations. Solar thermal energy has become very promising in recent years due to its abundance and clean energy in nature. This thesis presents the performance analysis of a solar thermal system consisting of a point-focus beam-down system and a Stirling engine to power rural areas. The estimation of solar radiation was performed based on the sunshine hour model using the Angstrom-Prescott correlation. The predicted solar radiation data from different databases were compared and the study area was found to have enough solar radiation potential. The energy demand assessment for households of specified rural villages (in Goroba) was made.

Microsoft Excel, EES, and Edraw max 7.9 are used for design calculation and analysis of the overall Beam-Down performance. The analysis is based on a theoretical design. Performance curves under varying operating temperatures and ambient conditions are presented. United Stirling 4-95 MKII Stirling engine of 25 kW rated power with 20MPa and hydrogen as working fluid is selected for the energy conversion unit. On the other hand, the heat flux and the temperature distribution at the final focal point of the concentrator and systems modeling are performed through Tonatiuh v_ 2.2.4.and Solidworks_2014, respectively. The result of Tonatiuh v_2.2.4 simulation shows that the flux distribution on the focal plane varies with the number of rays. For 1000W/m^2 of DNI and the number of rays at 10^8, the average flux is 56.65 kW/m^2. According to this simulation, the error decreases as the average heat flux as well as total power, increases.

From the design process, the total output power that goes to the storage battery is estimated at 303.32kWhe, and the levelized cost of energy is about 0.11US$/kWhe. Therefore, the proposed system can be recommended as a viable option for rural electrification.

***Keywords**: Beam-down, Collector, CSP, Energy, Solar-Stirling system.*

TABLE OF CONTENTS

LIST OF TABLES

LIST OF FIGURES

NOMENCLATURE

A_a	Aperture area	m^2
b	Arc length	m
C_p	Specific heat capacity at constant pressure	J/(kg.K)
C_v	Specific heat capacity at constant volume	J/(kg.K)
D	Diameter	m
Et	Equation of time	Minute
f	Focal length	m
g	Acceleration due to gravity	m/s^2
h	Heat transfer coefficient	W/m^2 K
I	Solar irradiance	W/m^2
l	Length	m
m	Mass flow rate	Kg/sec.
N_L	Daylight hour	Hrs.
$\vec{S}$	Sun vector	-
$\overrightarrow{N}$	Normal vector	-
$P_{\text{net.}}$	Net power	W
$P_{act.}$	Actual power	W
$P_{trac.}$	Tracking power	W
Q	Rate of heat supply	KJ
Q_u	Useful heat	W
Q_{sun}	Total heat from the sun	W
Q_{loss}	Heat losses	W
F_a	Aerodynamic force	N
T	Temperature	K, ^{0}C
R_r	Rim radius	m
r_1	Inner radius	m
r_2	Outer radius	m
W	Work done	W
v_w	Wind speed	m/s
v_s	Swept volume	m^3

Symbols

δ	Inclination angle	Degree
α	Altitude angle	Degree
ω	Hour angle	Degree
ϕ	Local attitude	Degree
θ_Z	Zenith angle	Degree
γ	Azimuth angle	Degree
ζ	Acceptance angle	Degree
ϕ_r	Rim angle	Degree
ς	Tracking angle	Degree
$\eta_{opt.}$	Optical efficiency	(%)
η_{vol}	Volumetric efficiency	(%)
η_o	Overall efficiency	(%)
$\eta_{th.str}$	Stirling thermal efficiency	(%)
K	Thermal conductivity	W m^{-1} K^{-1}
β	Coefficient thermal expansion	1/K
σ	Stefan Boltzmann constant	W m^{-2} K^{-4}
ρ	Density	Kg/m^3
ε	Emissivity	-

Subscripts

amb.	Ambient	*u*	Useful
conv.	Convective	*a*	Aperture
rad.	Radiation	*Act.*	Actual
loss.	Losses	*h*	hot
rec.	Receiver	*c*	Cold
thr.	Thermal	*max.*	Maximum
opt.	Optical	*ann.*	Annual
b	Beam	*d*	Diffused
Sc	Solar constant	*w*	Wind
Hi	Heliostat	*T*	Tower
e	East	***n***	North
z	Normal		

Abbreviations

AC	Alternating Current
BDOE	Beam-Down Optical Experiment
CLFR	Concentrating Linear Fresnel Reflector
CPC	Compound Parabolic Collector
CSP	Concentrated Solar Power
CST	Concentrated Solar Thermal
CR	Concentration Ratio
DC	Direct Current
DNI	Direct Normal Irradiance
EES	Engineering Equation Solver
FOE	Final Optical Element
GHI	Global Horizontal Irradiance
HTF	Heat Transferring Fluid
LFC	Linear Fresnel Collector
MCRT	Monte-Carlo Ray-Tracing
NSRDB	National Solar Radiation Data Base
PV	Photovoltaic
SCR	Secondary Central Reflector
WISDOM	Weizmann Institute of Solar Dedicated Comprehensive Master-code

CHAPTER ONE

1. INTRODUCTION

1.1. Background of Study

The planet receives more than 150,000 TW of energy from the sun. As much as half of the solar radiation reaches the earth's surface. At the same time, the remaining is being reflected and radiated by the atmosphere and clouds. This energy supply is supposed to meet the world's large energy demand [1]. Currently, the world trend toward the use of solar energy is rapidly increasing. The global installed capacity for solar-powered electricity reached 227 GWe at the end of 2015. The Concentrated Solar Power (CSP) remains with very limited capacity (4 GW today and 70 to 256 GW in 2040) according to the IEA scenarios, i.e., less than 3% of global capacity. Spain is the leader in CSP deployment with 2,362 MW installed capacity in 2016, followed by the USA with 1,804 MW [2].

Some African countries have a high potential to receive enough solar radiation as a result of their geographical location. For instance, in terms of potential, South Africa has the highest potential with a CSP of 43275 TWh/year, followed by Kenya with a potential of 15399 TWh/year, and Ghana with a CSP of 229 TWh/year [3]. Although not as much higher as the mentioned sub-Saharan countries, Ethiopia also has high solar resources. As shown in Figure (1.1), The average value of global horizontal irradiation (GHI) is about 2,000 kWh/m²/year [4].

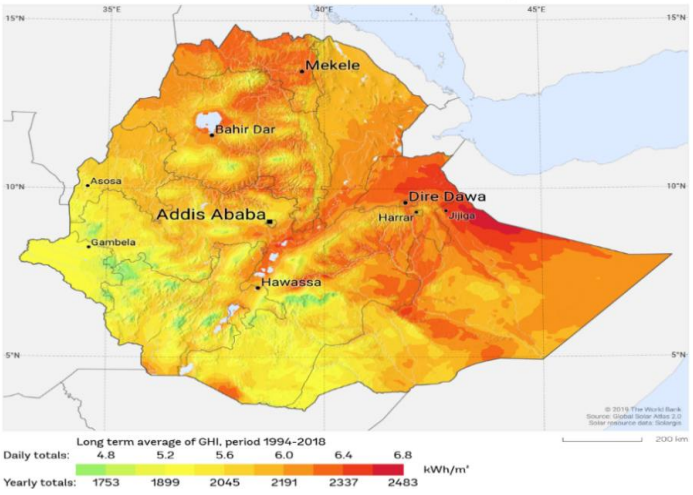

Figure 1.1: GHI in Ethiopia. (© 2022 The World Bank, Solar resource data: Solargis)

Solar energy can be used to generate electricity in two ways: directly and indirectly. In the direct method, photovoltaic (PV) modules are used to convert solar irradiation into electricity. While the thermal energy is harnessed using concentrated solar power (CSP) in the indirect method [5]. Concentrating solar power (CSP), systems use mirrors or lenses to focus direct beam solar radiation to produce useful energy such as heat and electricity [6]. There are two main categories of CSP technologies based on the distribution of concentrated solar radiation on the receiver. Line-focusing and point-focusing technologies [7]. Again, according to the sun tracking mechanisms, CSP can be classified into single and two axes tracking technologies [8].

This study is mainly focused on the design and optical performance analysis of a point-focus beam-down system in power production, which is one category of point-focusing technology. The system aimed to concentrate the available solar radiation in a single point to generate electricity. It will consist of three purposely designed collector mirrors, a secondary parabolic dish reflector, a tertiary reflector (CPC), and a Stirling engine.

Finally, the research presents the aim to accomplish the objectives by following all the procedural requirements, which include a Literature Review, sample collection, data analysis, software simulation, and discussion of results obtained from input data. After all, validation shall be undertaken, and a recommendation.

1.2. Motivation

Every human activity depends on energy. In the current world, electricity and fossil fuels are the main sources of energy to meet the energy demand. The worst thing is other biomass and firewood are the main sources of energy for most rural areas of our country. However, this has a negative economic, social, and environmental impact. For instance, the price of electricity and fossil fuels is rapidly increasing each year; the climate is changing as a result of pollution. All this makes the life of a human being complicated which directs the way to find an alternative source of energy called renewable energy. Renewable energy is sustainable, reliable, and clean energy. It may provide remote rural areas the option of producing their energy rather than using traditional sources of energy.

But, the cost of renewable technology energy technology is too high, especially for developing countries like Ethiopia. Again, concentrated solar power (CSP) plants are usually developed on a large scale. However, applying those in multi-generation at a small and micro-scale as an

alternative for powering remote rural and off-grid applications can reduce the extreme impact of the conventional source of power.

1.3. Statement of Problem

In Ethiopia, off-grid rural electrification using renewable energy is a highly attractive energy source for the rural population due to the scattered rural settlements [9]. Solar energy is one of the most common renewable energy sources, which is openly available and a clean energy source. Ethiopia has very high solar resources as a result of being located near the equator, and which average value of global horizontal irradiation (GHI) is about 2,000 kWh/m²/year [4]. However, despite the abundant solar resources in the country, as of now, only 14 MW has been installed, representing 0.3% of the country's total energy capacity [10]. Solar energy can be converted into electricity either within a photovoltaic cell (PVC) or concentrated solar power (CSP) system [11].

photovoltaic technology is limited due to the high initial investment cost and a decrease in collector performance over time due to overheating, dust accumulation, and solar radiation fluctuation, which results in approximately 25% overall losses [12]. Concentrated solar power (CSP) is classified as Line focusing and point-focusing technologies [13], [14]. They utilize lenses and mirrors to focus solar irradiation on a small area. The heat absorbed from solar radiation is then utilized in thermodynamic cycles to generate electricity [1], [14], [15]. In general, using CSP for off-grid rural electrification is most challenging because they are not suitable for small-scale, are expensive, and occupy large areas [5].

Many studies have been conducted to improve the design and development of CSP systems for rural electrification by considering optical performance, cost, and environmental issues. The literature confirms no specific work reported on the Design of small-scale Stirling power systems with a point focus Beam-Down for rural electrification. But, certain related work has been studied over the last few years. (See section 2.2).

In this research, an especially designed CSP system based on three trapezoidal heliostat collectors with a secondary dish reflector was proposed as an alternative system. The system will be designed to meet the partial energy demand, and it can easily be adaptable for rural electrification.

1.4. Objectives

1.4.1. *General Objective*

The general objective of this research is to design a small-scale Stirling power system with a beam-down focus for rural electrification.

1.4.2. *Specific objective*

- To determine the available solar radiation resource in the study area.
- To Design the elements of the solar power system unit, particularly; trapezoidal heliostat mirrors, a secondary parabolic reflector, and the CPC.
- To carry out the performance analysis of the designed solar power unit.
- To simulate the whole system and analyze the solar heat flux distribution at the focal point by using ray-tracing software (Tonatiuh).
- To size a suitable storage battery for a system designed.

1.5. Scope of the study

This study mainly focuses on analytical and numerical methodologies. It covers the forecasting of solar resources in the study area; and the design and performance analysis of the proposed beam-down system using mintab19, EES, and Microsoft Excel. Solar heat flux distribution, thermal effect analysis on the Stirling engine receiver using tonatiuh V2.2.4 and solid work_2014, sizing storage battery, and finally, economic feasibility study are all parts of this work.

1.6. Significance of the Study

The significance of this research is to accelerate the capability of using thermal energy from the sun, for rural electrification. The proposed system aims to achieve better performance and reliability, as well as better off-grid power access for the rural population. It generates electricity from solar radiation by using a Collector mirror integrated with a secondary dish reflector, tertiary reflector (CPC), and a Stirling engine. The power generated is stored in the storage battery, which is, in turn, used for different applications at any time.

The study targets to solve community-based problems. Since it provides green energy and cost-effective CSP technology, it will minimize grid electric and fossil fuel energy consumption. It will open an opportunity for further application of the concentrated solar power (CSP) system in

locations with high solar energy potential. So, it is a promising energy alternative, especially for the rural population. Finally, the result of the study can be used as a framework for future expansion plans by policy-maker.

CHAPTER TWO

2. LITERATURE REVIEW

Recently there has been a significant increase in the use of solar energy in a variety of applications. The reason for this is; the ongoing search for an alternative source of power as a result of the recognized scarcity of fossil fuels. It has grown in popularity as the cost of fossil fuels continues to rise. Solar energy is one of the most common renewable energy sources because it is a free and clean source of energy. Very soon, it will be expected to be the main optional energy source [16]. However, there are challenges associated with converting this solar energy source into continuous electrical power: In comparison to other energy sources, such as fossil fuels (MW/m^2), solar radiation reaching the earth's surface is diffuse (approximately $1000W/m^2$ max.): The sun shines intermittently in a daily cycle that is greatly affected by local weather conditions and follows a seasonal variation; The sun's position in the sky (azimuth and elevation) and thus the angle of incidence of direct beam radiation change continuously; Solar radiation cannot be directly stored; it must first be converted into heat, electricity, or chemical energy [17]. Therefore, finding high-efficiency advanced solar energy collector technology is highly suggestible.

2.1. An Overview of CSP Technologies

Solar energy collectors are special kinds of heat exchangers that transform solar radiation energy into the internal energy of the transport medium. Solar collectors are classified as non-concentrating and concentrating. Both non-concentrating and concentrating collectors have some areas to intercept and absorb solar radiation. whereas the latter has reflecting concave surfaces for focusing the beam of sunlight on a smaller receiving area, thus increasing the flux density. Concentrating solar collectors are appropriate for high-temperature applications [18].

Currently, there are four CSP technologies readily available for the collection of solar energy, as shown in Figure 2.1. These can be categorized into two groups, namely line concentrators and point concentrators. Line concentrators work by focusing the sun’s rays along a single focal line and thus only require a single-axis tracking mechanism. Point concentrators work by concentrating the sun’s rays on a single focal point and therefore require a two-axis tracking mechanism. Line concentrators technologies are the parabolic trough collector (PTC) and the linear Fresnel collector (LFC), while the point concentrators are the solar dish concentrators and the solar towers [14].

Point concentrators have the advantage of achieving much higher concentration factors than line concentrators.

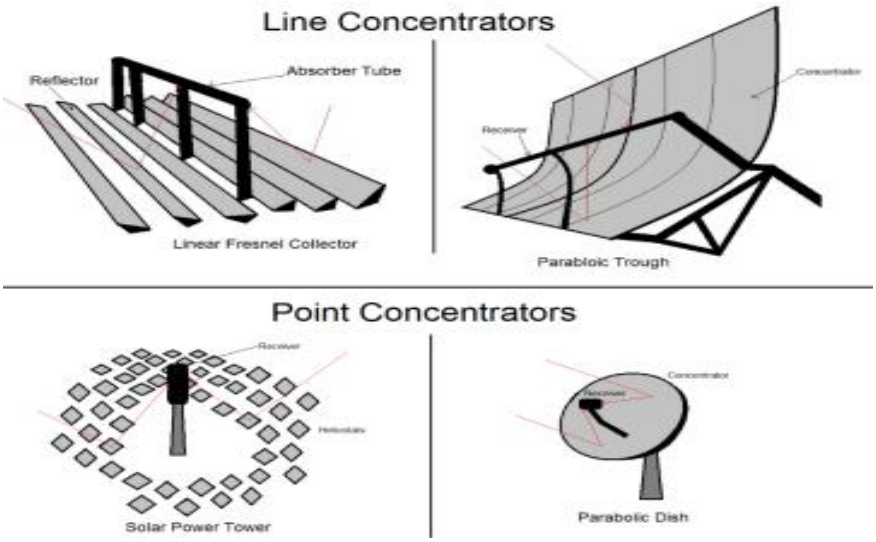

Figure 2.1: Types of CSP technologies [19].

Line concentrators only track the sun via a single degree of freedom-generally, varying the horizontal plane the reflector makes with the ground. Other arrangements are also possible such as vertical tracking, tilted tracking, and combinations of vertical and tilted tracking. Point concentrators differ by making use of an earth surface coordinate system to track the sun. The receiver's local horizon is taken as the central plane. The sun's movement is then tracked around the receiver via the azimuth angle in the horizontal direction, while the sun's variation in altitude is tracked via the change in zenith angle.

2.1.1. *Comparison of CSP technology*

The CSP systems can be distinguished and categorized according to their technologies or optical arrangement of concentrating reflectors. Currently, CSP technologies can be categorized into three primary types of systems: linear concentrators, dish/engine systems, and power towers. The characteristics, levels of development, scope of applications, and outlook of CSP technologies are all different. A brief comparison of performance data for various forms of CSP technologies is illustrated. (See Table 1.1).

Table 1.1 Performance data of various CSP technologies [20],[21].

CSP types	Operating temp. [^{0}C]	Installed Capacity [MW]	Concentration ratio	Average annual efficiency [%]	Land use [total area/power]
Trough	200-400	50-600	50-90	10-15	3.9
Fresnel	50-300	30-150	25-100	8-11	0.8-1
Power tower	300-1000	10-600	300-1000	17-35	-
Dish- striling	120-1500	5-25	1000-3000	25-30	1.2-1.6

2.1.2. *Historical development of the "Beam-Down" Reflector*

The concept of a tower "beam down" reflector was first proposed in 1995. It works by reflecting light downward from a heliostat's focal point using a hyperbolic mirror. Close to the ground, a CPC is installed, which collects the solar rays reflected by the hyperbolic mirror and concentrates them into a solar receiver on the ground level. To demonstrate the validity of this theory, work on a pilot station for 1MW of thermal power at WIS solar facilities began at the beginning of 1996. Finally, a hyperbolic mirror of more than 70m^2, with 850 trapezoidal facets, was planned and constructed. After more than 15 years, it was the largest optical concentrator in the world. (See Figure 2.2).

All the simulation models have been integrated into a program package named WISDOM (Weizmann Institute Solar Dedicated Comprehensive Master code). The general opinion of the solar scientific community is that this package, which is in continuous improvement, is one of the powerful unitary packages currently existing for solar optical modeling [22].

Figure 2.2: Beam down the solar field at Weizmann Institute of Science [23].

2.1.3. *Beam down optics*

The system comprises a heliostat field, a secondary reflector, a possible tertiary reflector, and a receiver. The design has two foci corresponding to the upper and lower focus of the solar system. Generally, it is represented by:

$$z = f(x,y) = \frac{(x^2 + y^2)/R}{1+[1-(1+k)(x^2 + y^2)/R^2]^{1/2}} \tag{1.1}$$

Where: R is the vertex curvature radius of the surface, and k is the conic constant. When k >1, the equation speaks for a hyperboloid surface of two sheets [24].

Two different quadratic surfaces are possibly used for the secondary reflector: hyperbolic and parabolic. As shown in Figure 2.3, the hyperbolic shape guarantees a convex secondary reflector placed below the upper focus, while the parabolic one is concave and installed beyond the aim point and so requires a higher tower, i.e., twice as much as the installation height and larger radius due to optical error amplification caused by higher optical path [25].

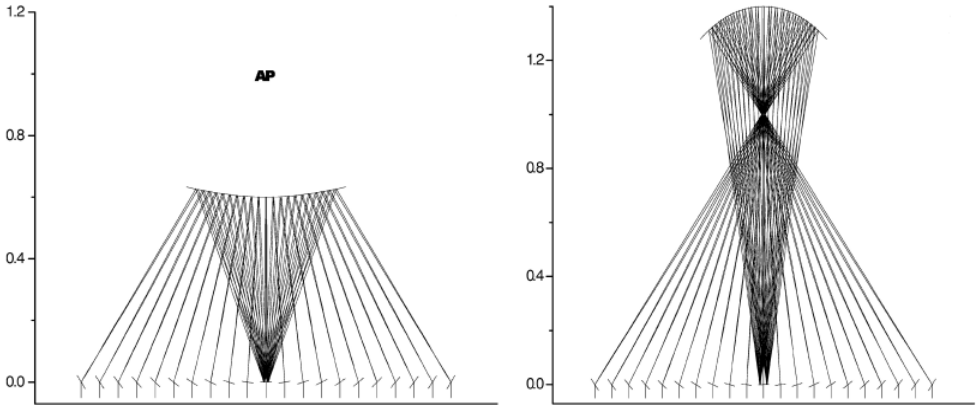

Figure 2.3: Secondary reflector possible geometries [25].

2.2. Related Works

The output of the solar power system is highly dependent on the efficiency of its collectors. Many studies have been conducted to improve the optical efficiency of the solar concentrator. Certain previous reports related to the proposed solar system are mentioned as follows.

Calvet *et al*. [26] State that the Institute of the Masdar built a new solar platform focused on the research and development of thermal energy storage technologies and concentrated solar power (CSP). Modern solar irradiance assessment tools, a beam-down CSP plant with 100 kW that has been customized for research purposes, one independent hot-oil loop of 100 kW, and novel thermal energy-storing devices are among the features of the facility. The goal of this plan is to provide CSP solutions that are affordable, to advertise and put these technologies to the test in harsh desert environments, and to ultimately create local knowledge. The objective of this article is not to report the experimental findings, but rather to provide a summary of the various possibilities of the Solar Platform of the Masdar Institute.

Fontani *et al*. [27] Investigate the optical approach to design a beam-down heliostat plant. Developing the optical design of a beam-down heliostats field; takes a lot of time and energy. To analyze the impact of solar divergence and the interaction of light with surfaces, one must use optical design software. Particularly to shape the field, the receiver's surface must have a uniform irradiance. This study presents a three-step process devoted to constructing the beam-down field based on real technical limits. The technique is used in a successful field simulation to learn more about its many phases.

Diago *et al*. [28] studied where should beam-down heliostat central rays intersect the axis of the final optical element axis. To achieve this, a beam-down solar system is designed to maximize the power collected through the final optical element concentrator. The power that goes to the outlet of the last optical element is investigated as a function of its facet reflectivity and the height of the center ray convergence point of the beam down's central reflector. A configuration that maximizes the energy fed to the solar receiver during the experimental campaign of the CSP on the Demo project is chosen and implemented at the beam-down installation at the Masdar Institute Solar Platform.

Taramona *et al*. [29] Conducted a study on the design of a flat beam-down linear Fresnel reflector. A linear beam-down solar field is made up of two reflections that concentrate solar irradiation on heavy materials on the ground. Several rows of identical size linear Fresnel reflectors direct the solar irradiation to a secondary mirror with a hyperbolic form that redirects solar concentration toward the ground receiver.

In this article, the fundamental constraint of the previously proposed hyperbolic secondary reflector is overcome. A new secondary reflector is proposed, consisting of several fixed flat mirrors positioned at the same height. A model is developed and validated using Monte-Carlo Ray Tracing software to calculate the optimum layout of this new solar field, the efficiency, and the concentration; relative errors of less than 15% were obtained. In order to facilitate the design of the flat beam-down linear Fresnel reflector, two new dimensionless parameters are suggested. Without any simulation, the concentration, optical efficiency, and receiver breadth can be easily calculated as functions of dimensionless parametric quantity. This innovative solar field can attain concentration ratios of up to 31 and optical efficiencies of up to 60%, achieving comparable concentrations while having a higher optical efficiency than a field utilizing a hyperbolic reflector.

Canavarro *et al*. [30] state that the standard concentrating solar thermal (CST) mono-tower technology, which uses one receiver placed on top of a tower to which all heliostats aim, is considered one of the best and most promising technologies for various CST- driven applications, such as CST power plants, solar metallurgical processes, thermochemical production of solar fuels, and recycling of waste materials. However, there are several technical problems, such as optical performance/tolerances, system dimensions, operation and maintenance issues, etc., with this technology. The so-called beam-down technology is an alternative to the standard CST mono-

tower technology, which uses a special mirror on top of the tower in place of a receiver to direct incident radiation from the heliostat field onto a receiver/reactor put closer to the ground and possibly deliver highest concentrations at the receiver.

In this study, a novel method for enhancing the optics of beam-down systems is presented. It is then applied to the optical design of a particular system, and the optical behavior of this design is demonstrated at two sites: Évora (Portugal) and Hurghada (Egypt). To minimize optical losses between each optical step, the method employs etendue-matching. Ray tracing simulations were run to examine the optical behavior of the system created as an example utilizing the etendue-matching method.

Diago *et al*. [31] Present how to maximize the net power of a faceted beam-down solar concentrator. In order to maximize the net power recovered by an upward-facing solar receiver, the beam-down solar concentrator at the Masdar Institute Solar Platform (Abu Dhabi, United Arab Emirates) is optimally connected with a final optical element (FOE). The FOE is constructed as a converging reflecting path with a hexagonal cross-section to further concentrate the solar flux onto the solar receiver. They develop effective methods for optimizing the orientation of the tower's central reflectors while also considering the geometry and dimensions of the FOE. The net power collected by the receiver and optimized dimensions of the FOE designs are presented as a function of FOE internal surface reflectivity and inlet height relative to the ground. Setups with a receiver aperture of 3m above ground that are optimized simultaneously with an 85% reflective FOE absorb 20% more power from the center reflector than equivalent setups without a FOE. With inlet-to-outlet lengths of less than 2 m, such optimal FOE designs are still viable. The findings could be used to build further beam-down projects using planar central reflectors.

Mokhtar *et al* [32] Presented the performance analysis of the beam-down optical experiment (BDOE), with full concentration. The analysis is based on radiation flux distribution data taken on March 21, 2011, using an optical thermal flux measurement system. In conjunction with the experimental results, a hypothetical thermal receiver design is utilized to determine the optimum receiver aperture size as a function of receiver losses and flux distribution. The overall output from the plant is calculated for various operating temperatures and three different control strategies, namely, the constant mass flow of the heat transfer fluid (HTF), constant outlet fluid temperature, and real-time optimal outlet fluid temperature. It was found that depending on temperature, the

optimum receiver aperture size (radius) varied between 1.06 and 1.71m. The optical efficiency of the BDOE ranged from 32% to 37% as a daily average (average over the ten sunshine hours). The daily average mean flux density ranged between 9.422 kW/m^2 for the 1.71m receiver and 20.9 kW/m^2 for the 1.06 m receiver. Depending on the control parameters and assuming an open receiver with solar absorptivity of 0.95 and long wave emissivity of 0.10. The average receiver efficiency varied from 71% at 300 ^{0}C down to 68% at 600 ^{0}C. The overall daily average thermal efficiency of the plant was between 28% and 24%, respectively, for the aforementioned temperatures. The peak of useful power collected in the HTF was around 105 kW at 300 ^{0}C mean fluid temperature and 89 kW at 600 ^{0}C.

Hernández *et al*. [33] This research presents a brand-new solar particle receiver design. In contrast to current technologies, the receiver is positioned at ground level, avoiding the need for a tower. Fresnel and beam-down optics are used to concentrate solar radiation on the solar receiver. The receiver is made up of several horizontally connected fluidized beds, each of which has a stage through which the gas flows in turn. The receiver presents a modular design, which allows the installation of several units in a series configuration to achieve a gradual increase in the gas and particle temperature. A Fresnel field of heliostats and a beam-down reflector are sized according to the standard Fresnel dimensions; as an example of the suggested design. A well-mixed fluidized bed model is used to determine the temperatures of the gas and the particles. With a 140m total length, a beam-down mirror 18m above the Fresnel reflectors, and a reflective Fresnel area of 9072m^2, the temperature of the gas and particles reaches approximately 800 ^{0}C.

L. Lifeng *et al.* [33] proposed a rotating tower reflector (TR) in a beam-down optical system to alternate concentrated solar irradiation on an array of solar receiver-reactors, realizing multi-step solar thermochemical redox cycles. Monte Carlo ray-tracing simulations are used to investigate the optical and radiative properties of the proposed system both analytically and numerically. They study the influence of the geometrical and optical parameters of the system on the optical and radiative performance. The receiver-reactor array must be accommodated by tilting the TR axis, which lowers optical efficiency. They demonstrate that for a baseline system with the receiver-reactor placed south of the tower, the annual optical efficiency declines from 46% to 37% when the TR's axis tilt angle increases from 2° to 20°. The optical analysis carried out in this study presents a generic formulation for predicting the required gain of thermal-to-chemical efficiency

of the receiver-reactor array to improve the overall solar-to-chemical efficiency of the solar thermochemical plant.

Khlief *et al*. [34] Conduct the optical analysis of several reflectors used in solar beam-down towers. The reflective solar tower concept is based on the reflection of solar radiations from heliostats towards the reflective mirror at the top of the tower, which is then diverted to one of its foci on the ground. This new layout would allow the energy collection to be positioned at ground level, avoiding the heavy tower top setup. For the suggested beam-down solar tower located at Universiti Teknologi Petronas, three reflective shapes are examined, i.e., ellipsoidal/concave, hyperboloid/convex, and a flat surface. A comparison study is conducted utilizing the lightXlab simulation platform to explore the influence of focal point distance on radiation spread at ground level, as well as the impact of the angle change of the second reflector on radiation concentration and beam travel. The results of the simulation showed that the flat surface reflector has superior and better control over the other two reflectors in terms of beam concentration and beam travel.

2.3. Research Gaps

Conventionally, the solar tower systems concentrate the solar light onto the receiver located on the tower top, while the beam-down system can concentrate light near the ground level. The energy conversion system consists of a receiver (molten salt), a pipe harness, and another system with huge thermodynamic cycles that work under different principles to generate electricity. Several studies have been conducted to improve the effectiveness of Beam-down systems for different purposes [29],[27]. For instance, in certain earlier research, the standard heliostat collectors, which have substantial shading and blocking effects, are utilized. Furthermore, as mentioned above, solar radiation is converted to useful energy through complex thermodynamic cycles. As a result, the system is too complex, high cost, and occupies a vast space (i.e., it is mostly built on a large scale). The proposed system will be expected to overcome this problem by directly applying the purposely designed heliostat primary collectors, upside down secondary dish reflector on top of the towers, tertiary collector (CPC), and Stirling engine.

CHAPTER THREE

3. METHODOLOGY

3.1. Description of Study Area

The study was carried out in Bule Hora (formerly Hagere Mariam, older, alternative names were Alga and Kuku) town in southern Ethiopia. It is located on the paved Addis Ababa-Moyale highway in the West Guji Zone of the Oromia region at 470 km distance from Addis Ababa. It is the largest town in this zone, mainly inhabited by the Guji Oromo, with a population density of 36.92 per square kilometer. Bule Hora is located at a coordinate latitude of 5°35′N and longitude of 38°15′E and an altitude of 1716 meters above sea level.

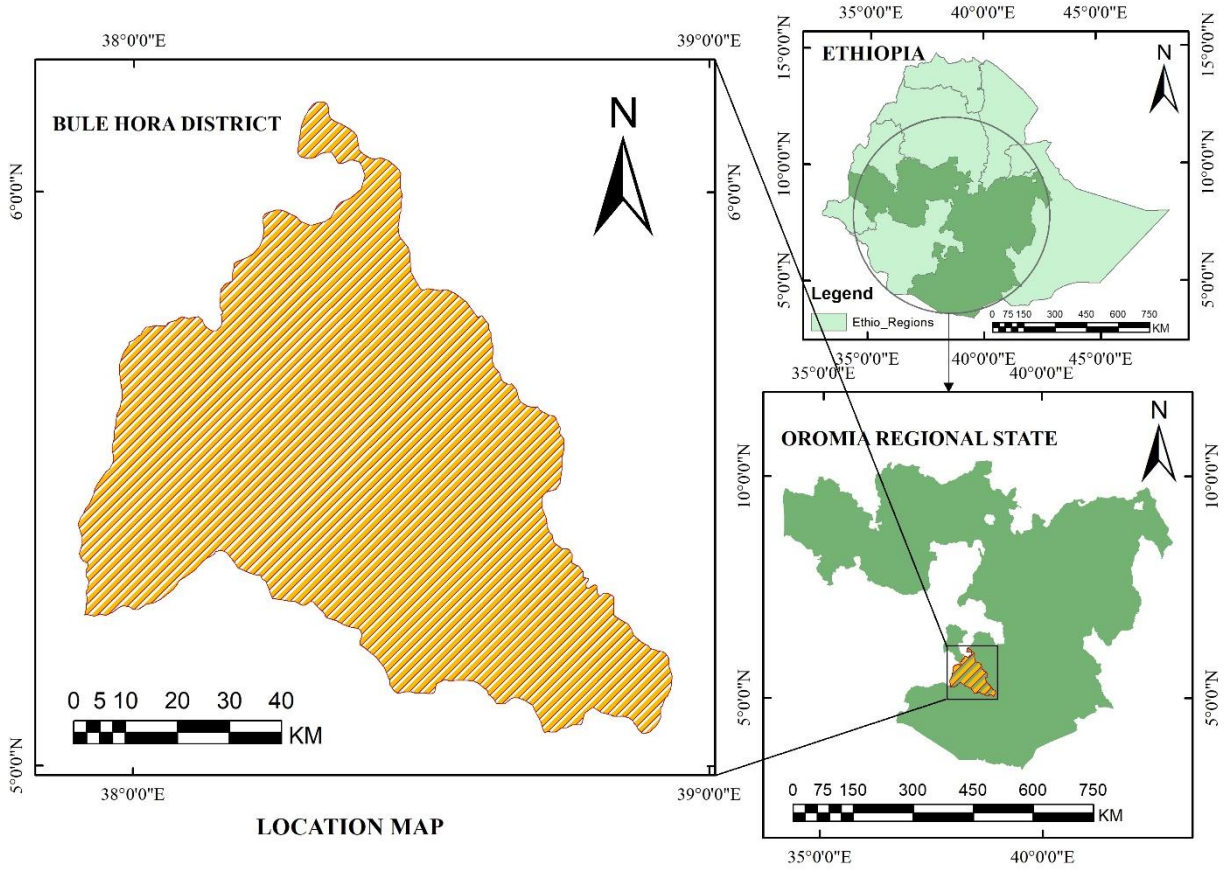

Figure 3.1: Location map of the Study area.

3.2. Data Collection and Analysis

To accomplish the objectives of this research, data (primary and secondary) are gathered from literature and other related sources. ArcMap_10.3 was used to locate the area with good solar radiation potential. Solar radiation and weather data were estimated using open-source software depending on site latitude and longitude. By keeping this in mind, the sunshine hour data was gathered using the *Meteonorm*, *New_locclim* online software. The global solar radiation was calculated by Angstrom-Prescott's (1940) correlation, and the result was examined with the data generated from the *Retscreen*, *Solargis*, *NSRDB*, and *PVGIS*.

Data analysis is accomplished with *Microsoft Excel*, *EES*, and *Edraw_max.7.9* software. Heat flux distribution at the engine receiver, ray-tracing analysis of the collectors, and system design modeling were conducted by using *Solidwork_2014* and *Tonatiuh v_2.2.4* software. Figure (3.2) presents the general outline under which the objective of this research was achieved.

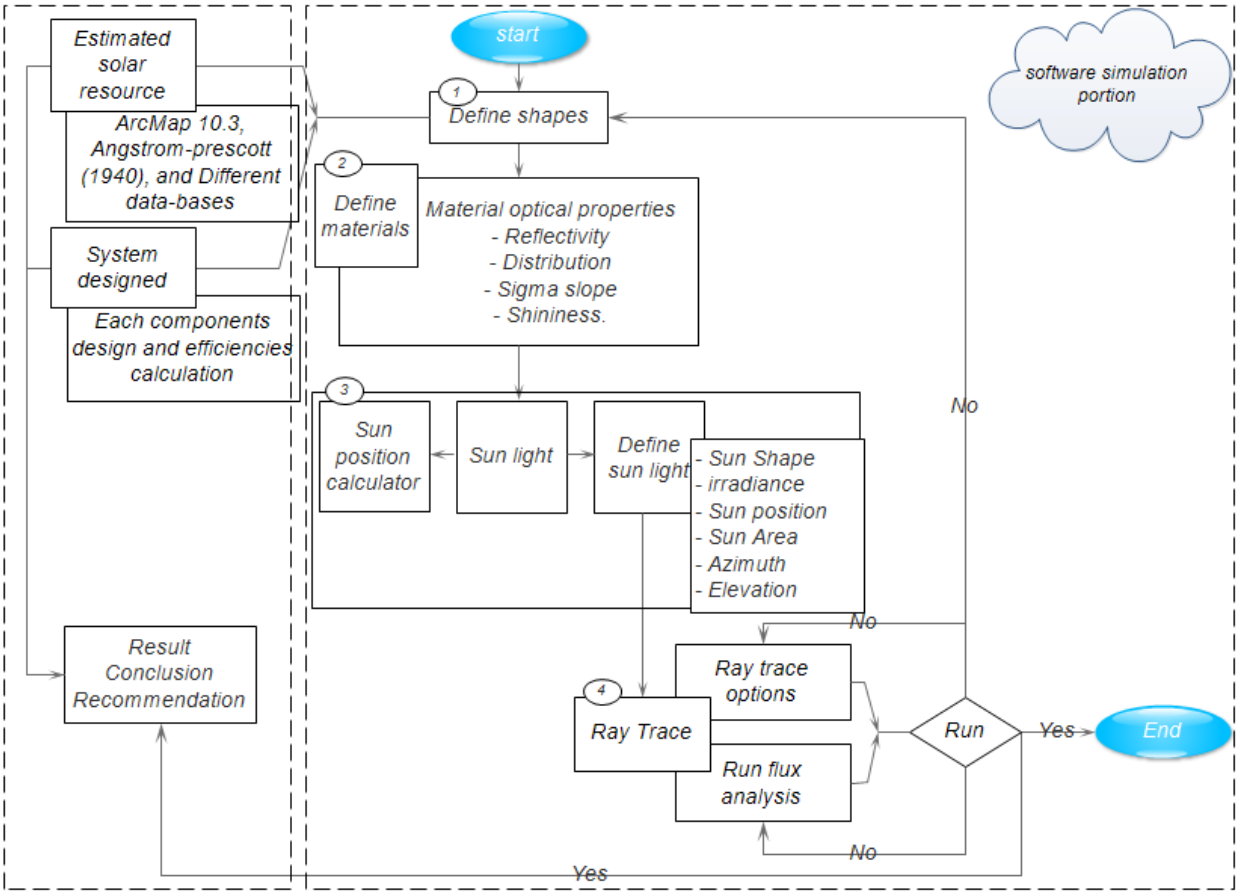

Figure 3.2: The general outline of the research.

3.3. System Description

Primarily a specially designed collector (trapezoidal heliostat) collects the direct solar radiation (DNI) from the sun onto a secondary parabolic dish. Three of them track the sun independently. The secondary dish reflector is hung on top of the towers below the common focal point of the primary collectors. Since it is a point focus, it collects solar radiation into a single point. To maximize the collected radiation, a tertiary reflector or compound parabolic collector (CPC) is installed. The CPC is also used to maintain the focal point of the secondary collector at a constant position. So, the light beam from the secondary dish reflector is projected down on a heat receiver of the Stirling engine through CPC, which is further converted to electricity.

Generally, the proposed system completely rejects the huge and complex energy conversion cycles that are common for conventional LFC or power tower systems. Again, unlike the conventional, a receiver is located near the ground. Figure (3.3) illustrates more about the working principle of the proposed system.

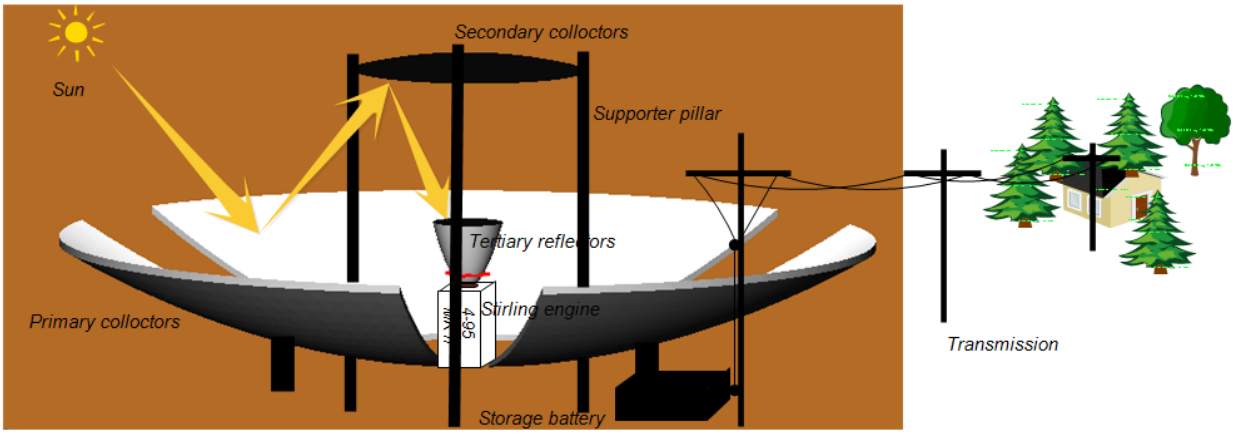

Figure 3.3: 3D-Model of Small-scale Beam-down solar system.

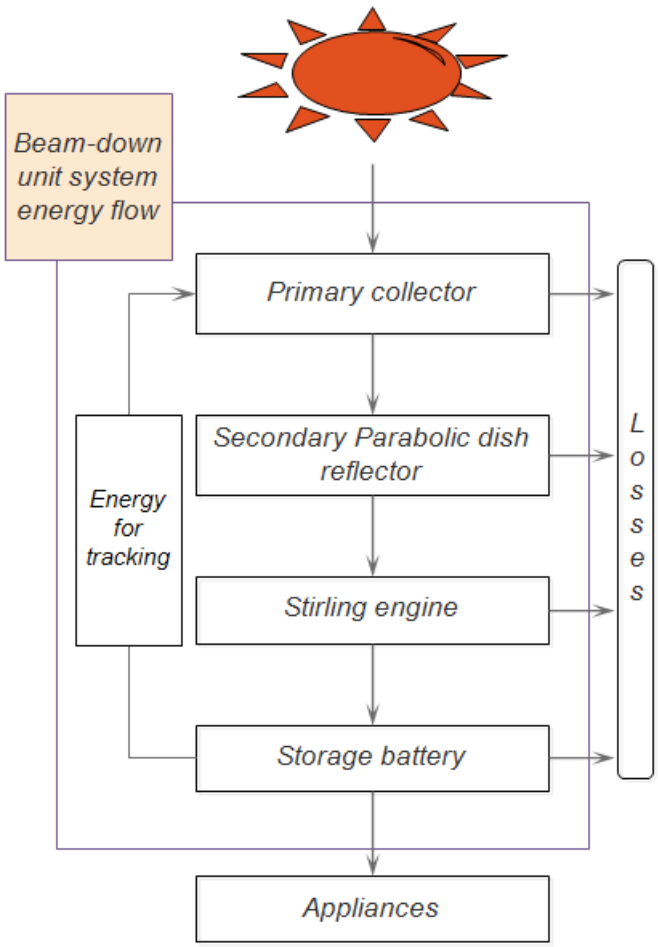

Figure 3.4: Energy flow block diagram.

3.4. Solar Radiation Components

The declination is the angular distance of the sun north or south of the earth's equator. The *declination angle*, δ, for the Northern Hemisphere (reverse the declination angle sign for the Southern Hemisphere) is given by equation (3.1)[35]. March 21, or the spring equinox, was selected as a design point day for this particular study.

$$\delta = 23.45\sin\left[\frac{N+284}{365}\times 360^{0}\right] \Rightarrow 23.45\sin\left[\frac{(59+21)+284}{365}\times 360^{0}\right] = 17.96^{0} \qquad (3.1)$$

Where: N is the day of the year ($1 \leq N \leq 365$)

Table 3.1: Day number and recommended average day for each month [18].

Months	Days Number	Average Day of the Month		
		Date	***N***	**δ (degree)**
January	*i*	17	17	-20.92
February	31+*i*	16	47	-12.95
March	59+*i*	16	75	-2.42
April	90+*i*	15	105	9.41
May	120+*i*	15	135	18.79
June	151+*i*	11	162	23.09
July	181+*i*	17	198	21.18
August	212+*i*	16	228	13.45
September	243+*i*	15	258	2.22
October	273+*i*	15	288	-9.60
November	304+*i*	14	318	-18.91
December	334+*i*	10	344	-23.05

There are several angles of interest in describing the position of the sun at a particular time instant. The *hour angle,* ω is the azimuth angle of the sun's rays caused by the earth's rotation and is computed from. (Assumed solar time is 12.5).

$$\omega = (ST - 12) \times 15^0 \tag{3.2}$$

$$\omega = (12.33 - 12) \times 15^0 = 4.95^0$$

The *hour angle*, as defined here, is negative in the morning and positive in the afternoon ($\omega = 0^0$, at noon).

The solar *altitude angle* (α_s) is the apparent angular height of the sun in the sky. The *zenith angle* (θ_z) and its complement, the altitude angle (α_s), are given by:

$$\cos(\theta_z) = \sin(\phi)\sin(\delta) + \cos(\phi)\cos(\delta)\cos(\omega) \tag{3.3}$$

$$\cos(\theta_z) = \sin(5.58)\sin(17.96) + \cos(17.96)\cos(5.58)\cos(4.95) = 13.3^0$$

And,

$$\theta_z + \alpha_s = 90^0 \tag{3.4}$$

Thus, $\alpha_s = 90^0 - 13.3 = 76.70^0$

The *sunset hour angle* (ω_s) can be derived when $\theta_z = 90^0$

$$\cos(\omega_s) = -\tan(\phi)\tan(\delta) \tag{3.5}$$

$$= -\tan(5.58)\tan(17.96) = 91.81^0$$

The *sunset hour angle, (ω_s)* is negative for sunrise and positive for sunset. And the sun travels 15° per hour through the sky, the number of *daylight hours* (N_L) can be determined by solving the above equation for ω_s and converting the resultant degrees into hours:

$$N_L = \frac{2}{15}\cos^{-1}(-\tan(\phi)\tan(\delta)) \tag{3.6}$$

$$= \frac{2}{15}\cos^{-1}(-\tan(5.58)\tan(17.96)) = 12.24\text{hrs}$$

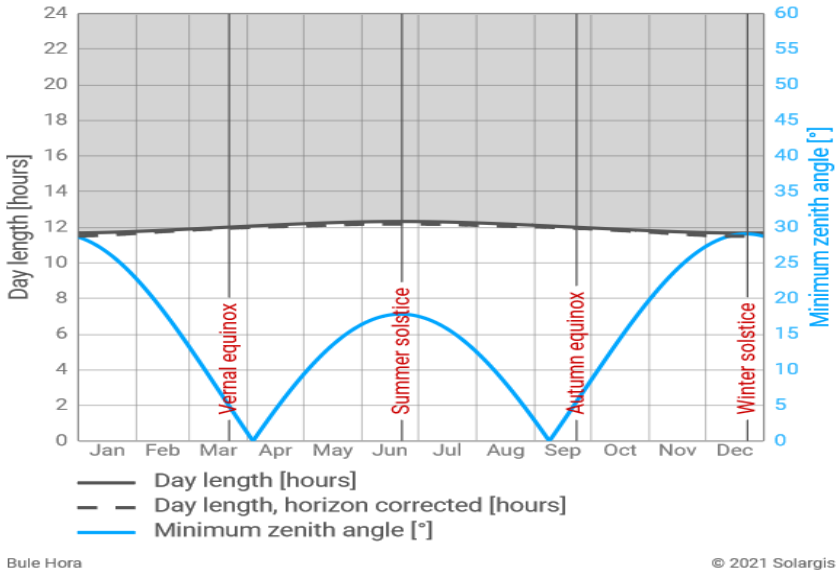

Figure 3.5: Estimates the mean value of day length and solar zenith angle throughout the year.

The *solar azimuth*, γ_s, is the angular displacement from the south of the projection of beam radiation on the horizontal plane.

$$\sin\gamma_s = \frac{\cos\delta\sin\omega}{\cos\alpha_s} \tag{3.7}$$

$$\gamma_s = \sin^{-1}\left(\frac{\cos(17.96)\sin(4.96)}{\cos(76.70)}\right) = 20.9^0$$

By using the above equations, the apparent route of the sun through the sky can be graphically represented by a sun path chart, as shown in Figure 3.6. The elevation (or altitude angle) of the sun is plotted against the azimuth at various times during the year.

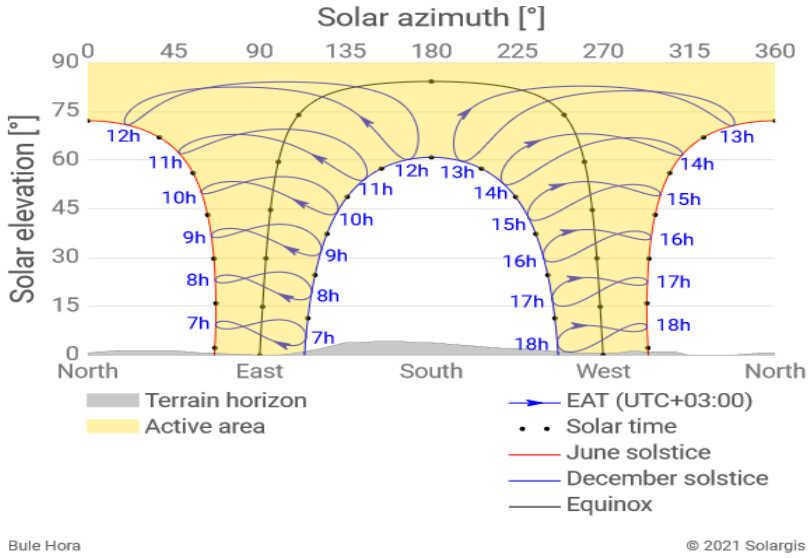

Figure 3.6: Elevation and azimuth angles of the sun at various dates and times during the year for 5.64^0 N latitude.

3.5. Extraterrestrial Solar Radiation

The amount of solar radiation per unit time, at the mean distance of the earth from the sun, received on a unit area of a surface normal to the sun (perpendicular to the direction of propagation of radiation) outside the atmosphere is called the *solar constant*, G_{sc}. When the sun is closest to the earth, on January 3, the solar heat on the outer edge of the earth's atmosphere is about 1400 W/m^2; when the sun is furthest away, on July 4, it is about 1330 W/m^2 [36],[37].

The extraterrestrial radiation (G_{on}) measured on the plane normal to the radiation on the N_{th} day of the year can be calculated by:

$$G_{on} = G_{sc}\left[1 + 0.033\cos\left(\frac{360N}{365}\right)\right](\text{W/m}^2) \qquad (3.8)$$

Where: G_{sc} = solar constant, and the latest value of G_{sc} is 1367 W/m^2.

3.5.1. *Extraterrestrial radiation on a horizontal surface*

A solar radiation incident on a horizontal plane outside of the atmosphere is a normal incident of solar radiation. And given by:

$$G_{oH} = G_{sc}\left[1 + 0.033\cos\left(\frac{360N}{365}\right)\right]\cos\theta_z \tag{3.9}$$

Combining Equation (3.9) $\cos\theta_z$ with Equation (3.3) gives G_{oH} for a horizontal surface at any time between sunrise and sunset:

$$G_{oH} = G_{sc}\left[1 + 0.033\cos\left(\frac{360N}{365}\right)\right](\cos\phi\cos\delta\cos\omega + \sin\phi\sin\delta) \tag{3.10}$$

It is often necessary for the calculation of daily solar radiation to have the integrated daily extraterrestrial radiation on a horizontal surface, H_o. This is obtained by integrating Equation 3.10 over the period from sunrise to sunset. If G_{sc} is in W/m^2, H_o in daily J/m^2 is:

$$H_o = \frac{24\times 3600 G_{SC}}{\pi}\left[1 + 0.033\cos\left(\frac{360N}{365}\right)\right](\cos\phi\cos\delta\sin\omega_s + \frac{\pi\omega_s}{180}\sin\phi\sin\delta) \tag{3.11}$$

Where: ω_s is the sunset hour angle in degrees.

To calculate the extraterrestrial solar radiation on a horizontal surface for an hour. Equation 3.11 is integrated between hour angles, ω_1 and ω_2 (ω_2 is larger). Therefore,

$$I_o = \frac{24\times 3600 G_{SC}}{\pi}\left[1 + 0.033\cos\left(\frac{360N}{365}\right)\right](\cos\phi\cos\delta[\sin\omega_2 - \sin\omega_1] + \frac{\pi(\omega_2 - \omega_1)}{180}\sin\phi\sin\delta) \tag{3.12}$$

It should be noted that limits ω_1 and ω_2 may define a time period other than an hour.

3.5.2. *Prediction of average solar radiation*

3.5.2.1. *Prediction of Monthly Average Daily Horizontal Global Radiation from Sunshine Duration*

Solar radiation estimate is an important factor for the analysis and assessment of the solar radiation potential of a given region. There is an equation called Angstrom- Prescott (1940). The monthly mean daily global radiation on a horizontal surface is estimated from sunshine records by the modified Angstrom correlation.

$$\frac{\overline{H}}{\overline{H_o}} = a + b\frac{\bar{n}}{\overline{N_L}} \tag{3.13}$$

Where:

$\overline{H}$ = monthly average daily radiation on the horizontal surface

$\overline{H}_o$ = monthly average radiation outside of the atmosphere for the same location,

a, b = empirical constants

$\bar{n}$ = monthly average daily hours of bright sunshine,

$\overline{N}_L$ = monthly average of maximum possible daily hours of bright sunshine

$\frac{\overline{H}}{\overline{H_o}}$ = monthly average clearness index (denoted by, $\overline{K}_T$)

The regression parameters *a* and *b* can be obtained from.

$$a = -0.110 + 0.235\cos\phi + 0.323\left(\frac{\bar{n}}{\overline{N_L}}\right) \tag{3.14}$$

$$b = 1.449 - 0.553\cos\phi - 0.694\left(\frac{\bar{n}}{\overline{N_L}}\right)$$

The monthly average clearness index $\overline{K}_T$ is the ratio of the monthly average daily radiation on a horizontal surface to the monthly average daily extraterrestrial radiation. In equation form,

$$\overline{K_T} = \frac{\overline{H}}{\overline{H_o}} \tag{3.15}$$

The daily clearness index, K_T can be defined as the ratio of the daily total to the extraterrestrial radiation for that day given by:

$$K_T = \frac{H}{H_o} \tag{3.16}$$

Similarly, an hourly clearness index, k_T can be defined by:

$$k_T = \frac{I}{I_o} \tag{3.17}$$

3.5.2.2. *Prediction of Beam and Diffused Components of Hourly Radiation*

The fraction of the hourly radiation on a horizontal plane that is diffused can be correlated to the hourly clearness index, k_T, and the ratio of the total radiation to the extraterrestrial radiation for the hour. The equation for the correlation is given by:

$$\frac{I_d}{I} = \begin{cases} 1.0 - 0.249k_T & for \quad k_T < 0.35 \\ 1.557 - 1.84k_T & for \quad 0.35 < k_T < 0.75 \\ 0.177 & for \quad k_T < 0.75 \end{cases} \tag{3.18}$$

3.5.2.3. *Prediction of Beam and Diffused Components of Daily Radiation*

$$\frac{H_d}{H} = \begin{cases} 0.99 & for \quad K_T \le 0.17 \\ 1.188 - 2.272K_T + 9.473K_T^2 - 21.865 + 14.648K_T^4 & for \quad 0.17 < K_T < 0.75 \\ -0.54K_T + 0.632 & for \quad 0.75 < K_T < 0.80 \\ 0.2 & for \quad K_T \ge 0.80 \end{cases} \tag{3.19}$$

Where: K_T = the daily clearness index

3.5.2.4. *Prediction of Monthly Average Daily Horizontal Global Radiation from Sunshine Duration*

The monthly average hourly global radiation on a horizontal surface can be calculated from the monthly average daily global radiation on a horizontal surface by using the expression proposed by Collaros-Pereira and Rabl, 1979.

$$\frac{\bar{I}}{\bar{H}} = \frac{\pi}{120}(a + b\cos\omega)\frac{\cos\omega - \cos\omega_s}{\sin\omega_s - \frac{\pi}{180}\omega_s\cos\omega_s} \tag{3.20}$$

Where: $a = 0.409 + 0.5016\sin(\omega_s - 60)$

$$b = 0.6609 + 0.4767\sin(\omega_s - 60)$$

3.5.2.5. *Prediction of Monthly Average Hourly Horizontal Diffused Radiation from Monthly Average Daily Horizontal Diffuse Radiation*

This is obtained by using the following expression of Lui and Jordan (1960).

$$\frac{\overline{I_d}}{\overline{H_d}} = \frac{\pi}{120}\frac{\cos\omega - \cos\omega_s}{\sin\omega_s - \frac{\pi}{180}\omega_s\cos\omega_s} \tag{3.21}$$

3.5.2.6. *Prediction of the monthly average of daily diffused radiation on a horizontal surface*

Two types of correlations have been developed for this purpose and they are:

$$\frac{\overline{H_d}}{\overline{H}} = 1.403 - 1.672\overline{K}_T \tag{3.22}$$

And

$$\frac{\overline{H_d}}{\overline{H}} = 0.931 - 0.814\left(\frac{n_s}{N_s}\right) \tag{3.23}$$

Generally, the clear sky beam radiation on a horizontal surface is:

$$I_b = I_n\tau_b\cos\theta_z \tag{3.24}$$

Where: $I_n = I_{SC}\left[1.0 + 0.033\cos\left(\frac{360N}{365}\right)\right]$ and $\tau_b = a_o + a_1\exp\left(\frac{-k}{\cos\theta_z}\right)$

Where: τ_b - beam radiation transmittance and the constants a_o, a_1 and k are found from a_o^*, a_1^* and k^* which are given as:

$$\begin{aligned} a_o^* &= 0.4237 - 0.00821(6-A)^2 \\ a_1^* &= 0.5055 + 0.00595(6.5-A)^2 \\ k^* &= 0.2711 + 0.01858(2.5-A)^2 \end{aligned} \tag{3.25}$$

Where: - $a_o = a_o^* r_o$; $a_1 = a_1^* r_1$ and $k = k^* r_k$.

r_o = 0.95; r_1 = 0.99 and r_k = 1.02. And *A* is the altitude of the observer in kilometers.

The transmittance of diffused radiation τ_d through clear skies can be estimated from the beam radiation transmittance based on the study of Liu and Jordan:

$$\tau_d = 0.271 - 0.2939\tau_b \tag{3.26}$$

The clear sky diffuse radiation is:

$$I_d = I_n\tau_d\cos\theta_z \tag{3.27}$$

Therefore, the totally clear sky radiation on a horizontal surface could then be estimated as follows:

$$I_T = I_b + I_d \tag{3.28}$$

Finally, the solar radiation during representative days of months is predicted by using the above correlations. Table (3.2) summarizes the predicted solar radiation in the Bule Hore region. The predicted average daily global solar radiation varies from around 4.67 kWh/m^2/day in the rainy month of July to just 6.56 kWh/m^2/day in the dry months.

Table 3.2: The predicted average daily global radiations on horizontal surfaces during representative days.

Months	Date	ω_s(°)	n [hrs.]	N_L [hrs.]	$\frac{n}{N_L}$	a	b	H_o [kwh/m^2]	H [kwh/m^2]	*Clearness index* (K_T)
January	17	87.86	8.50	11.72	0.72	0.35	0.40	10.02	6.39	0.638
February	16	88.71	8.01	11.83	0.68	0.34	0.43	10.37	6.56	0.633
March	16	89.76	7.37	11.97	0.62	0.32	0.47	10.49	6.41	0.611
April	15	90.93	7.45	12.12	0.61	0.32	0.47	10.18	6.18	0.607
May	15	91.90	6.42	12.25	0.52	0.29	0.54	9.62	5.49	0.571
June	11	92.39	6.82	12.32	0.55	0.30	0.52	9.26	5.43	0.586
July	17	92.17	4.95	12.29	0.40	0.25	0.62	9.38	4.67	0.464
August	16	91.34	4.90	12.18	0.40	0.25	0.62	9.32	4.92	0.498
September	15	9022	6.18	12.03	0.51	0.29	0.54	10.30	5.82	0.565
October	15	89.05	6.70	12.87	0.52	0.29	0.54	10.34	5.90	0.571
November	14	88.08	7.93	11.74	0.67	0.34	0.43	10.06	6.32	0.628
December	10	87.62	6.97	11.68	0.60	0.32	0.48	9.86	5.99	0.607

3.6. Sun Vector

The orientation of each heliostat is determined by the sun vector. This vector indicates the angle of the sun rays with wrt. a horizontal surface at the heliostat's location. It is expressed in terms of the zenith angle, θ_z, and the solar azimuth angle, γ_s. The Figure 3.7. Show three components of the sun vector and the important angles.

The sun vector is determined as follows:

$$\vec{S} = [s_e, s_n, s_z]^T \tag{3.29}$$

Where: the subscripts ***e, n,*** and ***z*** refer to directions east, north, and zenith, respectively.

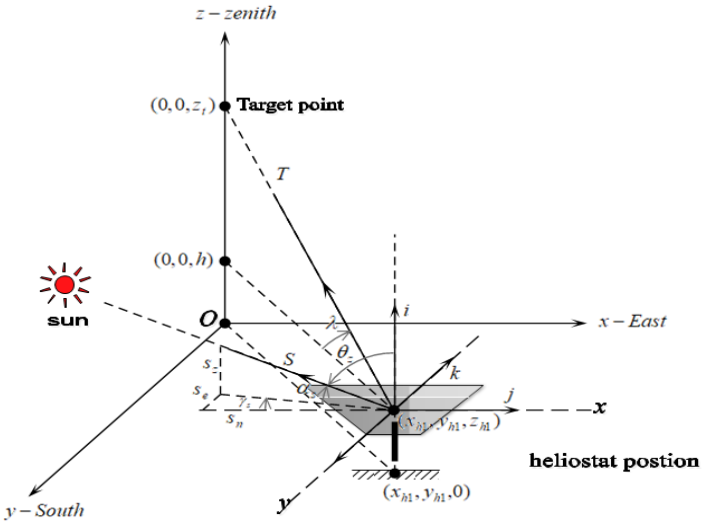

Figure 3.7: Sun vector and target with associated sun angles.

And,

$$\begin{aligned} \vec{s}_e &= \cos\alpha_s(-\sin\gamma_s) \\ \vec{s}_n &= \cos\alpha_s(-\cos\gamma_s) \\ \vec{s}_z &= \sin\alpha_s \end{aligned} \tag{3.30}$$

Where: s_e, s_n, and s_z are referred to east, north, and zenith sun vectors components, respectively

Therefore,

East component: $\vec{s}_e = \cos(76.7)(-\sin(20.9)) = -0.082$

North component: $\vec{s}_n = \cos(76.7)(-\cos(20.9)) = -0.215$

Zenith components: $\vec{s}_z = \sin(76.7) = 0.973$

3.6.1. *Target vector and heliostat normal*

The target vector is the vector pointing from the heliostat to the tower [38]. To calculate the target vector, one collector in the field must be selected as well and the location of the tower also needs

to be considered. Therefore, the coordinate of the particular collector under study and the tower of the field is given below. (See Table 3.3). Figure (3.8) shows the field layout of the proposed system.

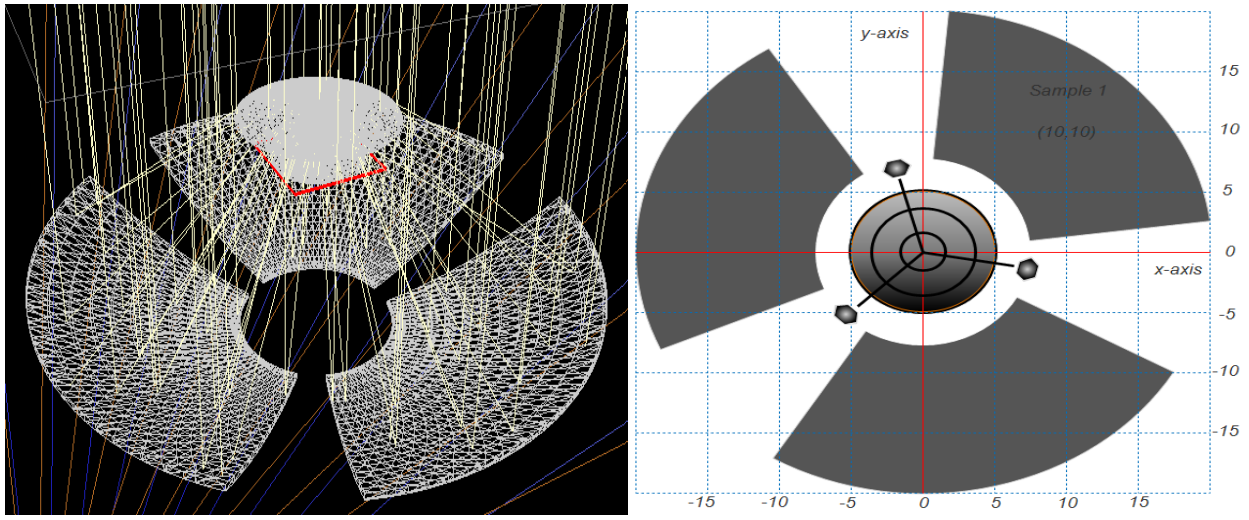

(a) (b)

Figure 3.8: (a) Beam-down wireframe, (b) Layout of the proposed solar power system.

Table 3.3: The coordinate of the collector under study.

Sample 1	**X**	**Y**	**Z**
Heliostat	10m	10m	2.5m
Tower	0	0	15m

Thus, the target vector can be calculated as equation (3.42):

$$\vec{T}_{hi} = \begin{bmatrix} x_T - x_{hi} \\ y_T - y_{hi} \\ z_T - z_{hi} \end{bmatrix} \tag{3.31}$$

Where: (x_T, y_T, z_T) - are the coordinates of the target, (x_{hi}, y_{hi}, z_{hi}) - are the coordinates of the collectors, *hi*. Then,

$$\vec{T}_1 = \begin{vmatrix} 0-10 \\ 0-10 \\ 15-2.5 \end{vmatrix} = \begin{vmatrix} -10 \\ -10 \\ 12.5 \end{vmatrix}$$

The magnitude is as follow:

$$T_1 = \sqrt{(-10)^2 + (-10)^2 + (12.5)^2} = 18.875$$

This vector is unitized by dividing each component of the vector by its magnitudes:

$$\hat{t}_i = \frac{\overrightarrow{T_{hi}}}{\left\|\vec{T}_{hi}\right\|} \tag{3.32}$$

Thus,

$$\vec{t}_1 = \begin{vmatrix} -10/18.875 \\ -10/18.875 \\ 12.5/18.875 \end{vmatrix} = \begin{vmatrix} -0.529 \\ -0.529 \\ 0.649 \end{vmatrix}$$

The vector normal to the surface is dependent on two unit vectors pointing from the reflector center—the first pointing towards the sun (*S*) and the second towards the receiver (*t*). The unit vector normal to the surface of the heliostat (*n*) is then defined as.

$$\overrightarrow{N} = \vec{S} + \vec{t}_1 \tag{3.33}$$

Therefore,

$$\overrightarrow{N} = \begin{vmatrix} -0.082 - 0.529 \\ -0.215 - 0.529 \\ 0.973 + 0.649 \end{vmatrix} = \begin{vmatrix} -0.611 \\ -0.744 \\ 1.622 \end{vmatrix}$$

The resultant vector is unitized by dividing each component of the vector by the magnitude of the vector:

$$\vec{n} = \frac{\vec{S} + \hat{t}_1}{\left\|\vec{S} + \hat{t}_1\right\|} \tag{3.34}$$

Where: $\left\|\vec{S} + \hat{t}_1\right\| = \sqrt{(-0.611)^2 + (-0.744)^2 + (1.622)^2} = 1.886$

$$\vec{n} = \begin{vmatrix} -0.611/1.886 \\ -0.744/1.886 \\ 1.622/1.886 \end{vmatrix} = \begin{vmatrix} -0.324 \\ -0.395 \\ 0.860 \end{vmatrix}$$

Finally, Tonatiuh V 2.2.4 software, on the base of the Monte Carlo ray tracing (MCRT) method, was adopted for ray tracing and the prediction of heat flux distribution at the focus point.

CHAPTER FOUR

4. DESIGN AND ANALYSIS

The Beam-Down Solar Thermal Concentrator is a point-focus concentrator. The primary collector system comprises three 2-axis independently sun-tracking heliostat collectors. The primary heliostat collectors focus sunlight on one imaginary upper focal point. The radiation gets intercepted by a secondary Central Reflector (SCR) on top of the tower and is then redirected to a lower focal point close to ground level. The Beam-Down system is a central-tower-like system, but instead of collecting solar energy in the heat transfer fluid on top of the tower as is done in conventional tower plants, the receiver is located at the lower focal point close to the ground. This is accomplished by a set of secondary optics of a secondary central reflector [39][40].

4.1. Design Considerations

The determination of the concentration field area serves as the key to CSP plant design and is normally calculated by applying the design point method. The design point is a very important concept for CSP generation design and can be used to determine the parameters of various segments of the solar concentration field, the receiver, thermal storage, and power generation. Factors of a design point include time, solar DNI, ambient air temperature, wind speed, etc. The time selection is normally midday during the spring or autumn equinox; the annual mean temperature can be used as the ambient air temperature, and the annual mean wind speed can be used as the respective wind speed [41].

4.2. Energy Demand Assessment

Ethiopia is a country in which 80% of the population lives in rural areas. Furthermore, the settlement of the population in the rural pastoral areas is in a scattered manner. It is remote from the national grid, and the major energy sources for those areas are 85% firewood, 1% electricity, and 14% gas for lighting and cocking [42]. In order to improve the life of those communities. This condition must be changed, and they must get electricity access with available resources. This study aims to get electricity access for one rural village in the Oromia region, West Guji zone, Bule hora woreda (particular place name: Goroba). In this village, 100 households were assumed to assess the total energy demand of the community in the village for design purposes. Table (4.1)

illustrates the frequently used appliances in this village and the energy needed to run the appliances:

Table 4.1: Household appliance. [*https://generatorist.com*]

Household appliance	Running watts	Quantity	Hours	Total energy (Wh)
Home internet router	5	10	5:00	250
Cocking stove	2100	3	2:00	12600
Laptop	300	20	4:00	24000
TV (LED)	17(22''), 85(49'')	40, 20	6:00	10880
Cell phone charger	25	200	1:00	5000
Clock radio	50-200	25	5:00	12500
Electric shaver	15	50	5:30	4125
Outdoor light	250	75	10:00	187500
Light bulb	9	300	3:00	8100
	Total wattage = 45680W			**Total energy = 264955Wh**

4.3. Site Selection

The location is situated near Bule hora City in the Oromia region, Ethiopia, geographically located at latitude 5.63 N and longitude 38.24 E. The total energy demand identified for this study was 45.68 kW, equal to a scaled yearly average of 265 kWh/day. (See Table 4.1). The layout of the site is shown in Figure 4.1; it is roughly equal to 0.62 acres and is approximately (50 x 50) m^2 rectangular field.

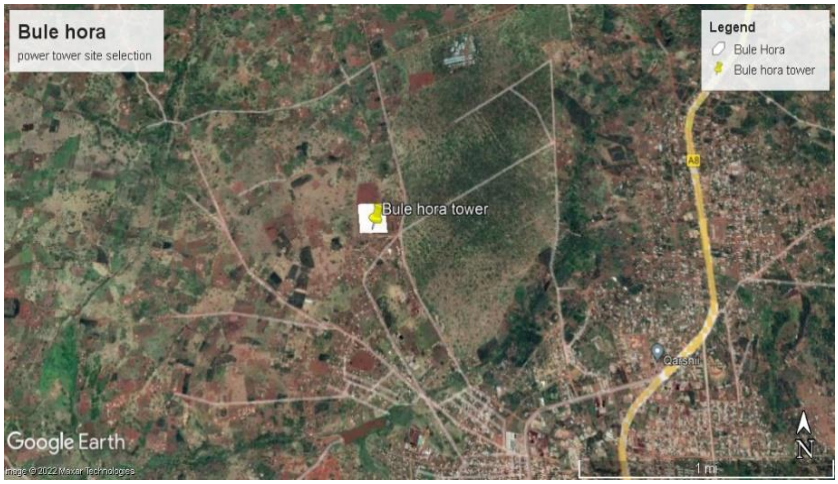

Figure 4.1: Site of the project. Source: *Google Earth*

4.4. Beam-down System Component Design

4.4.1. *Design of parabolic concentrators*

Primarily, it is essential to consider the location of a point that is at an equal distance from a line (directrix) and a focal point; when designing the parabolic concentrator. The mathematical representation of the parabolic concentrator is a paraboloid, which can be described as a surface formed by rotating a parabola around an axis, as shown in Figure 4.2.

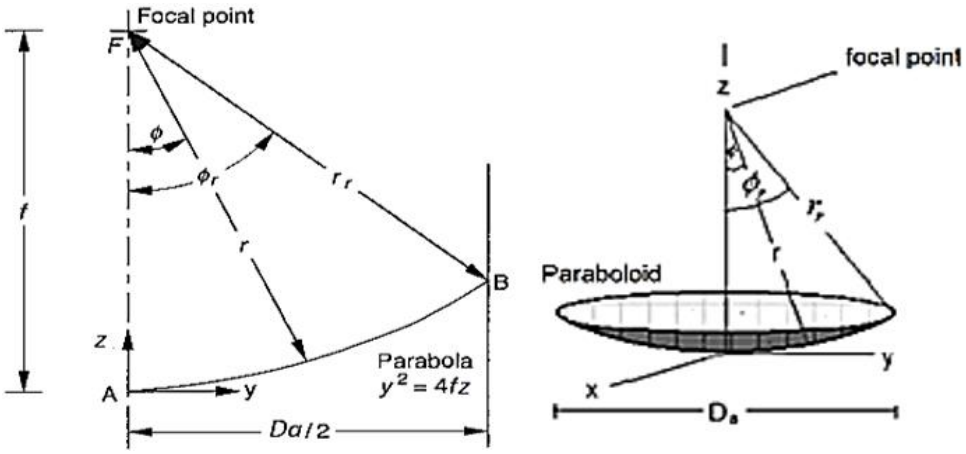

Figure 4.2: Section of a parabolic concentrator and the x, y, and z coordinates [43].

The equation of the parabola, in terms of the coordinate system shown, is:

$$y^2 = 4fz \tag{4.1}$$

Where: x and y are coordinates in the aperture plane, and z is the distance from the vertex measured along the line parallel with the paraboloid axis of symmetry; f is the distance from the vertex to the focus along the paraboloid axis of symmetry or focal length.

For the calculation of necessary points that define parabola public domain software Parabola Calculator 2.0 [http://mscir.tripod.com/parabola/] is used. The calculated coordinates (x and y) for the designed paraboloid shapes are also shown in Table 4.2:

Table 4.2: x-y coordinate of the parabolic shape segments by using the Parabola Calculator.

Segments No.	Primary collector	Secondary dish reflector	Tertiary reflector Or CPC
	(x, y) mm	(x, y) mm	(x, y) mm
1	-7746.00, 1000.00	-1250.00, 60.00	-500.00, 2000.00
2	-6777.75, 765.63	-1093.75, 45.94	-437.50, 1531.25
3	-5809.50, 562.50	-937.50, 33.75	-375.00, 1125.00
4	-4841.25, 390.63	-781.25, 23.44	-312.50, 781.25
5	-3873.00, 250.00	-625.00, 15.00	-250.00, 500.00
6	-2904.75, 140.63	-468.75, 8.44	-187.50, 281.25
7	-1936.50, 62.50	-312.50, 3.75	-125.00, 125.00
8	-968.25, 15.63	-156.25, 0.94	-62.50, 31.25
9	0.00, 0.00	0.00, 0.00	0.00, 0.00
10	968.25, 15.63	156.25, 0.94	62.50,31.25
11	1936.50, 62.50	312.50, 3.75	125.00, 125.00
12	2904.75, 140.63	468.75, 8.44	187.50, 281.25
13	3873.00, 250.00	625.00, 15.00	250.00, 500.00
14	4841.25, 390.63	781.25, 23.44	312.50, 781.25
15	5809.50, 562.50	937.50, 33.75	375.00, 1125.00
16	6777.75, 765.63	1093.75, 45.94	437.50, 1531.25
17	7746.00, 1000.00	1250.00, 60.00	500.00, 2000.00

The parabolic concentrator reflects solar radiation from the reflector mirror into the focal point or aperture of the receiver, where it is concentrated on the absorber. The focal length (f) is the distance from the vertex to the focus along the paraboloid axis of symmetry. It can be obtained by using the equation (4.2).

$$f = \frac{D_a^2}{16h} \tag{4.2}$$

Where: h is the depth and D_a aperture diameter of a parabolic dish. See Figure 4.3.

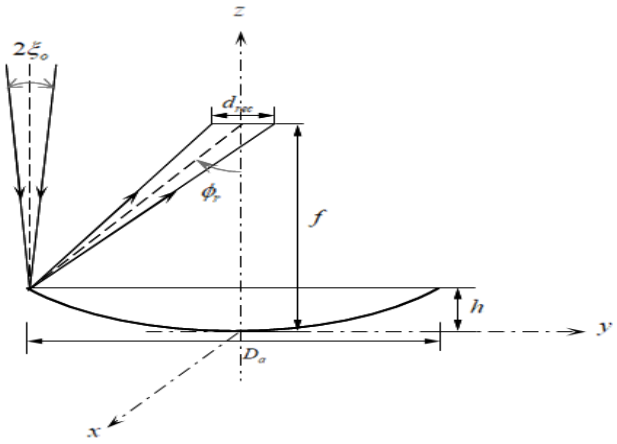

Figure 4.3: The dimension and geometry of the parabolic solar collector.

In this thesis paper, the parabolic dish concentrator is considered to be faced upside down so that the focal point is found at the bottom.

The *relative aperture* is defined as the relationship between the focal length and the diameter of the parabolic dish. It describes the shape of the paraboloid as well as the location of a focus point. The rim angle(ϕ_r) also defines the geometry of the paraboloid. The paraboloids used in solar collectors usually have rim angles ranging from 10º to 90º. As well as the paraboloid with small rim angles has a focal point and receiver at a large distance from the surface of the concentrator [44]. The relationship between the *relative aperture* and the *rim angle* is given by:

$$\frac{f}{D_a} = \frac{1}{4\tan\left(\frac{\phi_r}{2}\right)} \tag{4.3}$$

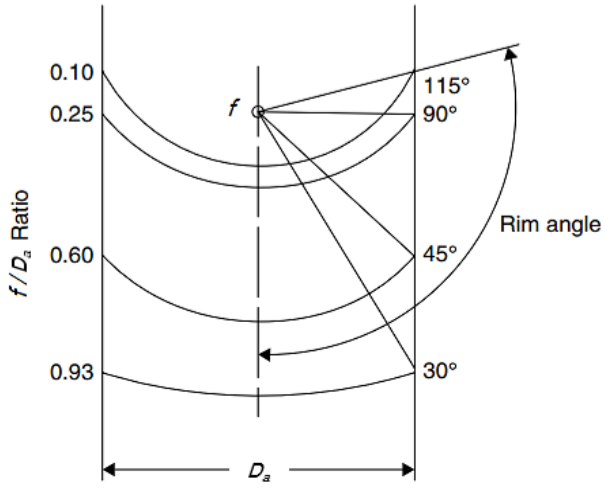

Figure 4.4: Relative aperture of a parabolic dish [45].

Another important parameter to define the geometry of the parabolic dish solar collector is *the rim radius* (r_r). It is the maximum distance between the focal point and the paraboloid extreme point.

$$r_r = \frac{2f}{1+\cos(\phi_r)} \tag{4.4}$$

Geometrical concentration ratio: It is defined as the ratio of the area aperture (A_{ap}) of the collector system to the receiver area (A_{rec}). The aperture of the system is the projected area of the collector facing or normal to the sun. In the case of this paper, the aperture area of the system is considered to be the total sum of the reflecting mirror area or heliostats. The temperature that can be achieved with a solar concentrator system increases with higher concentration ratios. The geometric concentration ratio (CR) is:

$$CR = \frac{A_{ap}}{A_{rec}} \text{ and } CR_{\max} = \frac{1}{\sin^2(\xi_{\max})} \tag{4.5}$$

Where: $\xi_{\max}$ is acceptance angle.

The aperture area of the parabolic dish can be calculated through the following ratio:

$$A_a = \frac{\pi D_a^2}{4} \tag{4.6}$$

The focal point diameter can be calculated by using Equation 4.7 [23]. Also, this factor will affect the size of the receiver. Figure (4.4) shows the effect of the acceptance angle on the parabolic dish, which is the angle of the worst condition that collects all reflected solar radiation from the concentrator in a short time for tracking.

$$d_{rec} = \frac{D_a \times \sin\xi_o}{\sin\phi_r} \tag{4.7}$$

The receiver is the interface between the concentrator and the engine. It absorbs concentrated solar flux and converts it to thermal energy that heats the working gas of the Stirling engine. The receiver area is represented as:

$$A_{rec} = \frac{\pi d_{rec}^2}{4} \tag{4.8}$$

The design parameter of the parabolic dish concentrator is summarized in the following table:

4.4.2. *Primary heliostat collector design*

The three specially designed heliostat collectors are arranged at an angle of 120^0 around the center of the system. (Figure 4.5). Then, the total area of the primary collectors can be calculated as follows.

$$\text{Area of collector\_1} = \frac{\alpha}{360} \times \pi r_2^{\,2} - \frac{\alpha}{360} \times \pi r_1^{\,2} \; or \; \frac{b_2 r_2 - b_1 r_1}{2} \tag{4.9}$$

$$\text{Where: } b = \frac{\alpha}{360} \times 2\pi r$$

$$\text{So, } b_1 = \frac{100}{360} \times 2\pi(2.5m) = 4.36m, \quad b_2 = \frac{100}{360} \times 2\pi(9.5m) = 16.6m, \text{ and}$$

$$\text{Area of collector\_1} = \frac{16.6m(9.5m) - 4.36m(2.5m)}{2} = 73.4m^2$$

Since we have three equal-sized collectors, the total collector's area will be equal to $220m^2$.

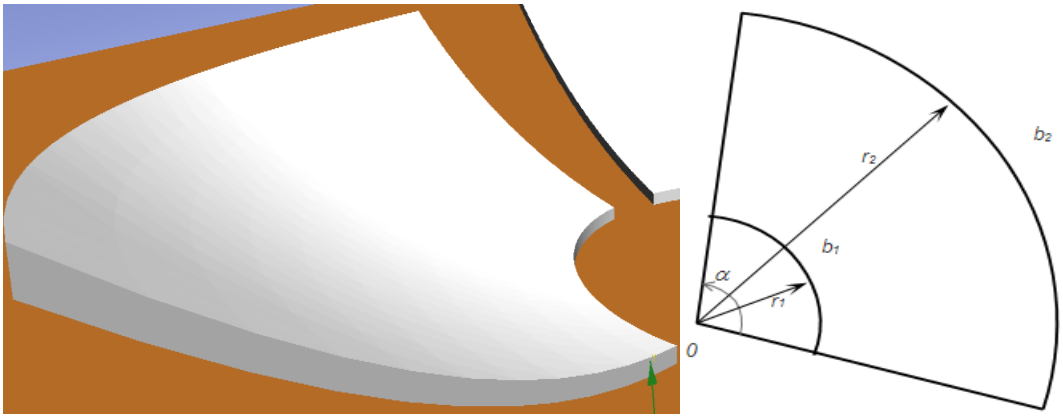

Figure 4.5: A primary collector mirror.

Table 4.3: Design parameters of the paraboloid shapes

Design parameters primary collectors	**Value**	**Unit**
Collector inner radius (r_1)	2.5	m
Collector outer radius (r_2)	9.5	m
Inner arc length (b_1)	16.58	m
Outer arc length (b_2)	4.36	m
sector angle (α)	100	(^{0})
Total collector area (A_t)	73.31x3 =220	m^2
Focal length	15	m

Rim angle	23.54	(^{0})
Depth	0.65	m
Concentration ratio	1100	-
Rim radius	15.65	m
Design parameter of a secondary dish reflector		
Dish aperture area	10	m^2
Focal length	6	m
Rim angle	17	(^{0})
Depth	0.13	m
Rim radius	6.13	m
Facet		
Facet design	Aluminum reflector	-
Reflectance	0.89	(%)

4.4.3. *Design of compound parabolic concentrator*

The receiver aperture must be wider to collect more energy. Nevertheless, at that aperture, a significant amount of energy will be lost due to reradiation. A solar concentrator customized at the receiver aperture is a good solution in most circumstances. A solar concentrator has a large entry area that can gather the necessary power from the collectors and a small exit area connected with the receiver aperture to reduce the loss by reradiation. Therefore, the CPC concentrator is the best choice [46]. All rays going inside at the maximum acceptance angle (θ_{max}) will pass through point F of the exit aperture (Fig 4.6). The acceptance angle (θ_{max}) and the entrance (d_1) or exit (d_2) apertures determine the 3D-CPC.

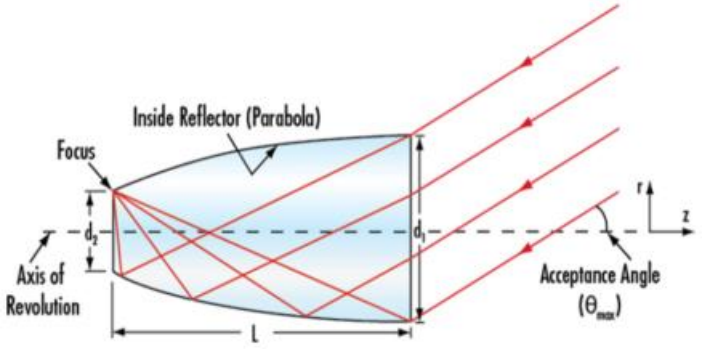

Figure 4.6: 3D - CPC scheme [46].

The acceptance angle (θ_{max}) and the dimensions of CPC (d_1 or d_2) are determined by a complex relationship between the CPC entry area, the collector field power (at least, at the design point), and the layout of a field. It is known, that the maximum concentration is given by:

$$C_{max} = 1/\sin^2\theta_{\max}; \quad (4.10)$$

And the length of CPC is:

$$l = (d_1 + d_2)/ (2\tan\theta_{max}) \quad (4.11)$$

Table 4.4: Design parameters of the tertiary reflector

Parameters	Value	Unit
Top opening diameter (d_1)	1	m
Bottom opening diameter (d_2)	0.25	m
Length (l)	1.5	m
Acceptance angle	22.62	degree

4.4.4. *Tower Design*

During a tower design for supporting a beam-down system, it is essential to have high optical access from the field collectors to the beam-down reflector. For a field of south-facing heliostats, the tower's north side must be highly visible. So that, the tower does not obstruct the rays that reflected from the heliostat field to the beam-down reflector. Again, for rays incoming from the east or west side of the tower, the visibility of the beam-down reflector is not obstructed when viewing the tower from the side. Another design consideration for the tower's construction is to use three steel-beam columns. A three steel-beam column tower interferes less with rays traveling from the heliostat field to the beam-down reflector.

Table 4.5: Design parameter of the supporting tower.

Parameters	Value	Unit
Steel-beam columns	3	Quantity
Length	14.5	m
Upper-end diameter	0.2	m
Lower-end diameter	0.3	m

4.4.5. *Metal support structure design*

The heliostat's ability to move and operate against design and operational wind loads is considered to be a significant component in heliostat strength. The tubular steel pedestal and the reflector support structure make up the metal support structure for glass-metal heliostats. The pedestal is hollow and made of galvanized steel. A torque tube assembly or a truss structure may be used to support the reflector. Large and medium-sized heliostats necessitate the use of hollow sections such as purlins and girders, whereas smaller heliostats can be created using stamped profiles mass-produced on a production line. [47] [48].

Table 4.6: Design parameter of heliostat collectors' support.

Pedestal	**Value**	**Unit**
galvanized steel (hollow)	3	Quantity
Inner diameter	0.3	m
Outer diameter	0.35	m
Length	2.5	m
Collector supporting structures		
Truss structure (rectangular hollow cross-section)	50 *50	mm^2

4.5. Stirling Engine

Stirling engine, named after its inventor Robert Stirling (1816), operates on a "*closed regenerative thermodynamic cycle with cyclic compression and expansion of a working gas at different temperature levels"*[49]. In comparison to an internal combustion engine, the Stirling engine has a high level of efficiency and produces significantly less exhaust. Since the Stirling engine can be powered by a variety of heat sources, including biomass, methane, and solar energy, it is also referred to as an external combustion engine.

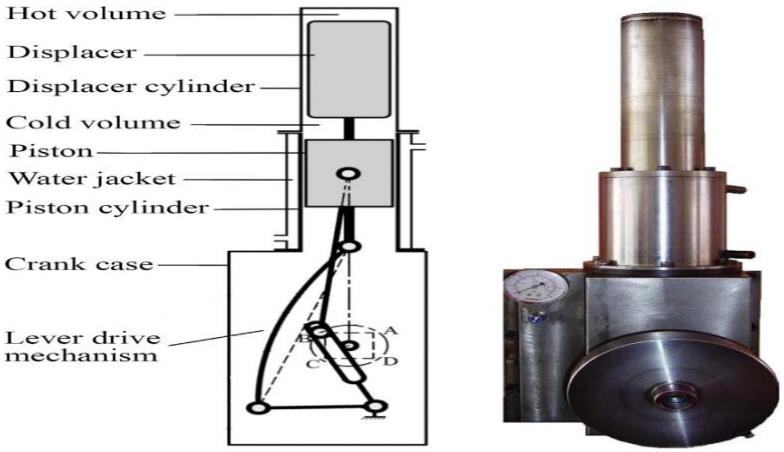

Figure 4.7: Lever-drive low and moderate temperature Stirling engine [50][51].

Stirling engines are made up of the following components:

1. *Heat source:* Since fuel does not directly contact the working fluid, Stirling engines can operate on fluids that otherwise damage some components of a conventional engine.
2. *Regenerator:* prevents waste heat from escaping into the atmosphere by temporarily storing it. This helps to attain high efficiencies that are similar to an ideal Carnot cycle. A straightforward design makes use of a tiny mesh of metallic wires. In an ideal Stirling cycle, the space that connects the hot and cold ends functions as a regenerator.
3. *Heat sink:* In most cases, the ambient environment serves as the appropriate heat sink. If not, frozen water or other icy substances, such as liquid nitrogen, can be used to maintain the cold side.
4. *Displacer piston:* It moves working gas between hot and cold zones, causing expansion and contraction to occur simultaneously during engine operation.
5. *Power piston:* transfers pressure to the crankshaft.

Stirling engines come in three mechanical configurations: alpha, beta, and gamma. Each arrangement has the same thermodynamic cycle but distinct mechanical design characteristics. [52][53].

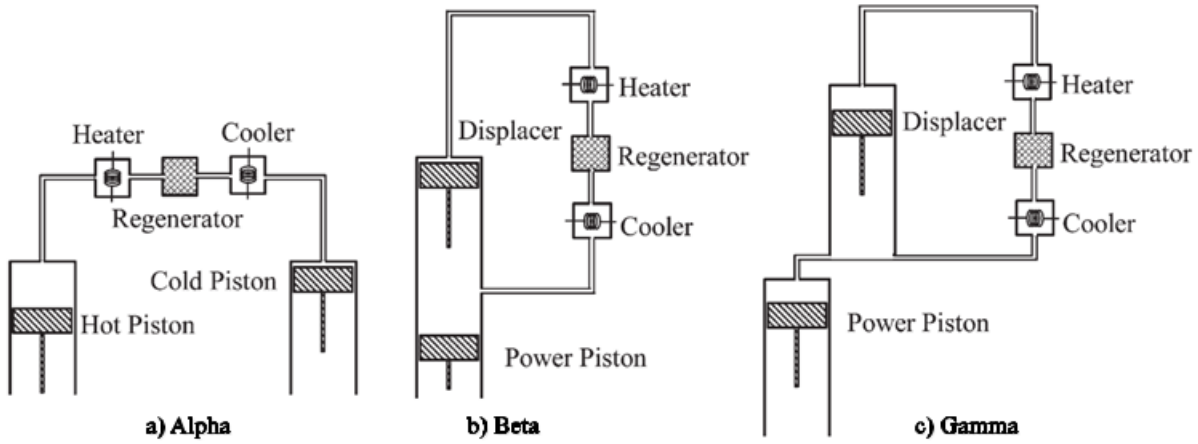

Figure 4.8: Three basic mechanical configurations for the Stirling engine [52].

A brief overview of various cylinder-coupling types is provided below:

- *Alpha*: It contains two pistons in separate cylinders that are linked in series to the heater, regenerator, and cooler. The adjacent pistons have a 90° phase difference.
- *Beta*: It houses both the displacer and the piston in the same cylinder. Separate linkages connect the displacer and piston to the crankshaft to maintain the proper phase angle.
- *Gamma*: The displacer and piston are arranged in the same way as in beta coupling, but in distinct cylinders. The cooler, heater, and generator are all linked in series between the two cylinders.

4.5.1. *Selection Engines working fluid*

For the Stirling engine's better performance, choosing the right working fluid is critical. A working fluid with high specific heat, high thermal conductivity, low density, and low viscosity is highly preferable [49].

Furthermore, availability, pricing, safety, and storage requirements are all critical considerations. The capability of a working fluid in terms of thermal conductivity, specific heat capacity, and density is defined as [54][55], which is helpful to preliminary working fluid selection.

$$\text{Capacity factory} = \frac{\text{thermal conductivity}}{\text{specific heat capacity} \times \text{density}} \tag{4.12}$$

According to the literature, thermal diffusivity is also a key property of the working fluid—the higher the value of thermal diffusivity, the greater the working fluid's performance. A few examples of working fluids are mentioned in Table 4.7.

Table 4.7: Thermal characteristics for various working fluids [49].

Working fluids	Thermal conductivity (W/m-K)	Density (kg/m^3)	Specific Heat (J/kg-K)	Thermal Diffusivity (m^2/s)
Helium	0.138	0.164	5188	$1.62* 10^{-4}$
Hydrogen	0.1805	0.0899	14310	$1.40*10^{-4}$
Air	0.024	1.225	1010	$1.94*10^{-5}$
Carbon dioxide	0.0146	1.98	844	$8.74*10^{-6}$

High-temperature and high-pressure Stirling engines run on hydrogen or helium. They are high-performance and typically operate at working fluid temperatures of over 973 K and pressures of up to 200 bar. The best Stirling engines have a heat conversion efficiency of approximately 40% [56]. At this time, kinematic Stirling engines such as the Kockums (United Stirling) 4-95 25-kWe, Stirling Thermal Motors STM 4-120 25-kWe, and the SOLO 161 11-kWe are examples of engines utilized in solar power systems [52].

In this thesis, the *"(United Stirling) 4-95 MKII Stirling engine*," which uses Hydrogen as a working fluid, was selected by considering their operating temperature and pressure, as well as the parameters mentioned in Table (4.7). The detailed information on the engine selected for this model is shown in Table (4.8). For more information [Table A1].

Table 4.8: Data on the United Stirling 4-95 MKII Stirling engine system [44].

Engine	
Manufacture	USAB
Model	4-95 MK II
Type	Kinematic
Power (elec.)	25-kW
Working fluid	Hydrogen
Pressure (max.)	20 MP

Gas temp. (high)	720 ^{0}C
Peak efficiency	41%
Receiver	
Type	Direct tube irradiation
Aperture diameter	20 cm
Peak flux	75 W/cm^2
Tube temp. (Max.)	810 ^{0}C
Efficiency	90%

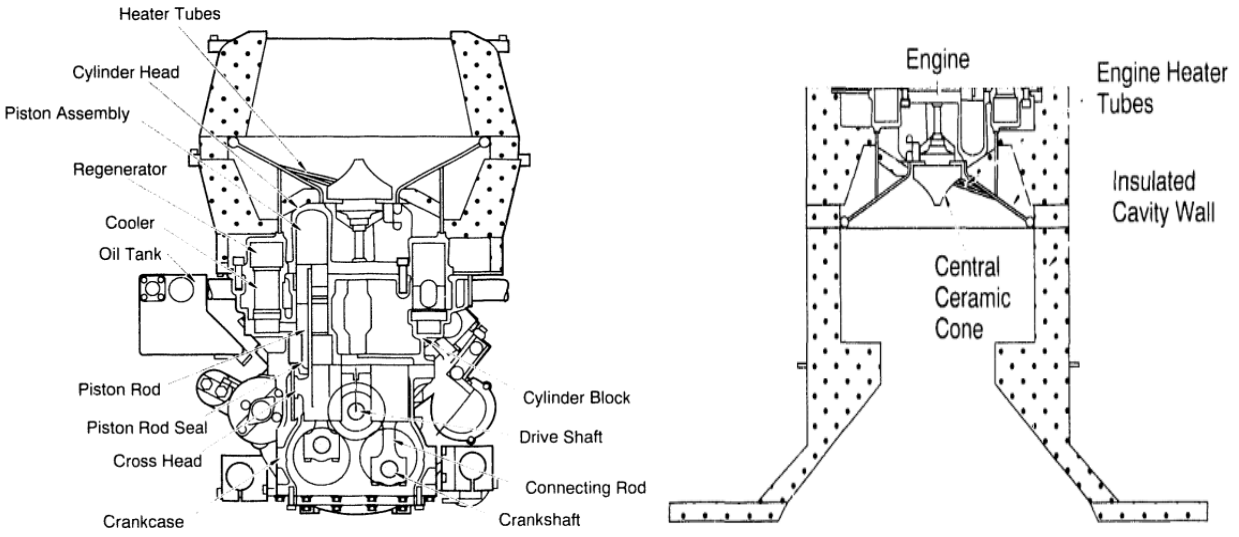

(a) (b)

Figure 4.9: (a). "(United Stirling) 4-95 MKII" Stirling engine. (b) Receiver [44].

4.5.2. *Stirling Cycle*

Stirling engine working can be described with the help of the Stirling cycle, which is a thermodynamic cycle consisting of two isothermal and two isochoric processes. Heat rejection and heat addition take place at a constant temperature. This can be illustrated with the help of an idealized Stirling cycle. (See Figure. 4.10).

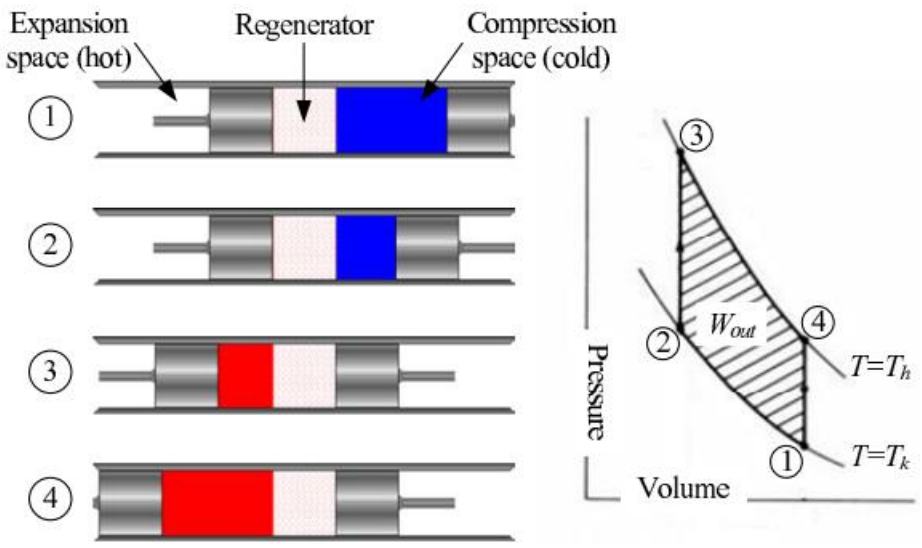

Figure 4.10: Pressure-volume diagram for the Stirling cycle [50].

Process Description of the given cycle:

- 1-2 *Isothermal compression:* The volume of the gas decreases, and the pressure increases as it gives up heat to the sink.
- 2-3 *Constant volume heating*: The volume of the gas remains constant as it passes back through the regenerator and regains some of its previous heat.
- 3-4 *Isothermal expansion*: The gas absorbs energy from the source, its volume increases, and its pressure decreases while the temperature remains constant.
- 4-1 *Constant volume cooling*: The volume of the gas remains constant as it transfers through the regenerator and cools.

4.5.3. *Stirling Cycle Efficiency*

Hot air expands when heated and contracts when cooled in a Stirling engine. Robert Boyle, an Irish scientist, has the best understanding of this operating principle. According to Boyle, the gas temperature (T) is inversely proportional to its volume. The product of pressure (P) and volume (V) occupied is a constant depending on the temperature of the gas [57].

Hence,

$$PV = nRT \tag{4.13}$$

Taking this into account, for an air-standard Stirling cycle, the amounts of heat added and rejected per unit mass of working fluid are as follows. (See Figure. 4.10)

$$Q_{added} = RT \ln v_1 / v_2 = \int pdv = nRT_h \ln v_1 / v_2 \tag{4.14}$$

$$Q_{rejected} = RT \ln v_2 / v_1 = \int pdv = nRT_c \ln v_2 / v_1 \tag{4.15}$$

where n is the number of a mole of gas, R is the universal gas constant = 8.321 J/ (mol. K), T_H is the source temperature in the Stirling cycle in K, T_C is the sink temperature in K, v_1, and v_2 are specific volumes of the constant-volume regeneration processes of the cycle in m^3/kg, and v_2/v_1 is the volume compression ratio. $v_1 = v_4$ and $v_2 = v_3$.

The net work done in the PV cycle is as follows:

$$W_{net} = Q_{added} - Q_{rejected} = nR[T_h - T_c]\ln\left(\frac{v_{\max}}{v_{\min}}\right) \tag{4.16}$$

However, W_{net} may not be obtained due to loss in friction, misalignment, improper temperature difference, and improper selection of material. So, we have to consider the Schmidt factor (which is equal to 0.559) to obtain actual work as follows:

$$W_{actual} = W_{net} * 0.559 \tag{4.17}$$

The Stirling engine's thermal efficiency can be expressed as:

$$\eta_{ths} = \frac{W_{net}}{Q_{added}} = \frac{nRT(T_h - T_c)\ln\left(\frac{v_{\max}}{v_{\min}}\right)}{nRT_h \ln\left(\frac{v_{\max}}{v_{\min}}\right)} = \frac{T_h - T_c}{T_h} \tag{4.18}$$

The Power and Torque can be obtained by:

$$P_{net} = W_{net} * f \tag{4.19}$$

Where: f is the frequency (Hz) and $1rpm = \frac{1}{60} Hz$

$$P_{Actual} = P_{net} * 0.559 \tag{4.20}$$

Now for the torque, we have [55].

$$P = \frac{2\pi N\tau}{60} \text{ Or, } \tau = \frac{P_{Actual} * 60}{2\pi N} \tag{4.21}$$

Where; N is flywheel revolution in rpm.

4.6. Optical Performance of the System

Decisions on the ideal position for locating collectors relative to the ray destination and how high to place the secondary reflector above the field represent a multifaceted problem with variables such as collectors' loss mechanisms (Figure 4.11). We will first go over some of these losses and then look at how they interact to create the best collectors field.

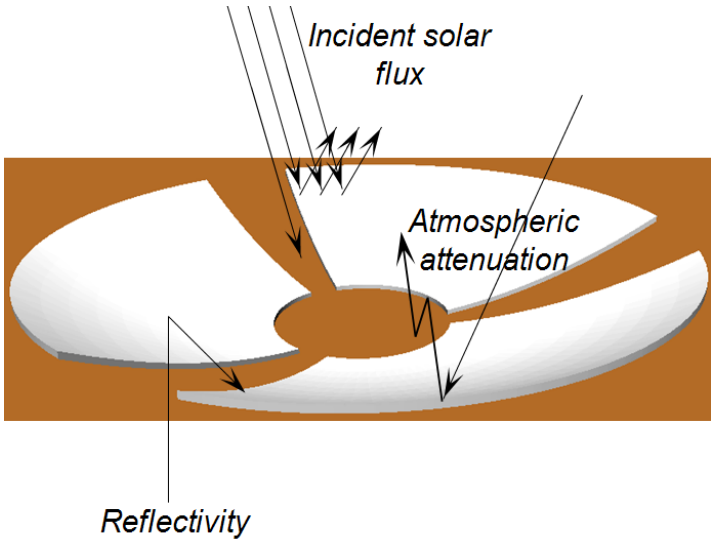

Figure 4.11: Collector's losses.

4.6.1. *Mirror reflectivity*

The collector's surface reflectivity is calculated as the product of the cleanliness of the mirror and the surface reflectivity. It is kept constant with a normal heliostat reflectivity and cleanliness value [58]. The factor, however, will vary depending on heliostat maintenance and manufacturer specifications. Thus the typical overall collector reflectivity can be taken as follows:

$$\eta_{ref} = 0.935 \times 0.95 = 0.89 \tag{4.22}$$

4.6.2. *Cosine efficiency*

The cosine efficiency has the greatest impact on the optical efficiency of the collector field because it accounts for the effective reduction in reflector surface area (as illustrated in Figure 4.12). The cosine effect is defined as the angle formed between an incident solar beam and a vector normal to the surface of a certain heliostat. It is thus affected by the position of the sun as well as the location of the collector under consideration [59].

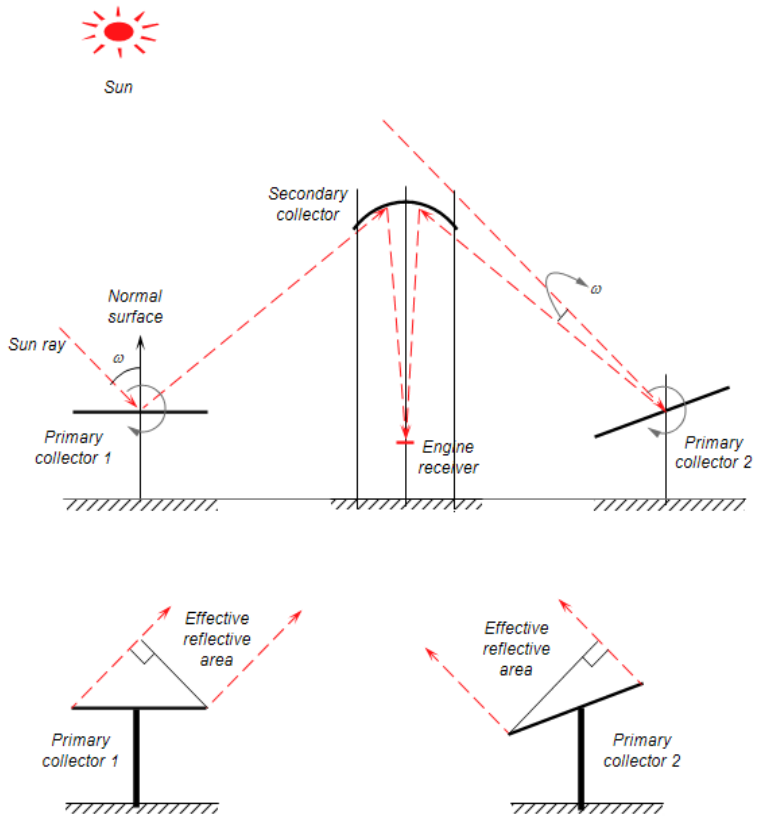

Figure 4.12: Cosine effect of beam-down collectors.

By using the Law of Reflection, the cosine efficiency and angle of incidence angle are determined as follows:

$$\eta_{\cos} = n \cdot S \tag{4.23}$$

$$\omega = \frac{\cos^{-1}(S \cdot t)}{2}$$

Where: n - is the normal vector to surface. S - is the sun vector, ω - the angle of incidence, and t - is the target vector (see section 3.6). Thus,

$$\eta_{\cos} = S \cdot n, \Rightarrow -0.08(-0.324) + (-0.21(-0.395) + 0.97(0.860)) = 0.943 \approx \underline{\underline{94.3\%}}$$

4.6.3. *Atmospheric attenuation factor*

A portion of the light reflected by a mirror surface is absorbed or scattered by the air, resulting in an atmospheric attenuation loss. In the case of particular weather conditions, the attenuation of

solar radiation is defined as a function of the distance between each collectors and the target *d*, and the greater the distance, the smaller the value of $\eta_{At:M}$ is [58].

$$\eta_{At.M} = \begin{cases} 0.99321 - 0.0001176\ d + 1.97\times10^{-8} d^2 & for,\ d \le 1000\ m \\ e^{-0.0001106\ \times d} & for,\ d > 1000\ m \end{cases} \quad (4.24)$$

Where: *d* is the distance between the center of the collector and the target, also known as the slant distance.

The distance of the collector under study from the target, *d*

$$\begin{aligned} d &= \|(x_h, y_h, z_h) - (x_T, y_T, z_T)\| \Rightarrow \|(10,10,2.5) - (0,0,15)\| \\ &= \underline{\underline{18.875}} m \end{aligned}$$

Then, the attenuation efficiency is:

$$\begin{aligned} \eta_{At.M} &= 0.99321 - 0.0001176 d\ + 1.95 * 10^{-8} d^2 \\ &= 0.99321 - 0.0001176\ (18.875) + 1.97 * 10^{-8} * (18.875)^2 \\ &= 0.9909 \approx \underline{\underline{99.1\%}} \end{aligned}$$

4.6.4. *Spillage efficiency*

It is the fraction of radiation arriving outside the entrance aperture of the secondary parabolic reflector. Its value ranges from 97 to 99% [58]. For this particular study, the spillage efficiency is assumed to be 98%.

4.6.5. *The optical efficiency of heliostat collectors*

The energy loss of a collector's field is measured by its optical efficiency. In general, the field's optical efficiency can be determined by:

$$\eta(x, y, t, n) = \eta_{ref}(x, y) \times \eta_{Cos}(x, y, t) \times \eta_{\text{int}}(x, y, t) \times \eta_{At.M}(x, y) \quad (4.25)$$

Finally, by using equation (4.25), the total optical efficiency of the collector ($\eta_{opt.\ collect}$) is estimated as 0.81.

Note: In this work, blocking and shadowing efficiency are not considered.

4.6.6. *The optical efficiency of the secondary parabolic reflector*

The optical efficiency η_{opt} depends on the optical properties of the materials involved (e.g., the reflectance of the dish and the optical properties of the receiver glazing, etc.), the geometry of the collector, and the various imperfections arising from the construction of the collector. It can be analyzed by identification of the different loss mechanisms and given as:

$$\eta_{\text{optSR}} = \lambda \rho \tau \alpha \gamma \tag{4.26}$$

Where:

- λ – is a shading factor; that is affected by the concentration ratio. It should be decreased as the concentration ratio increases and generally less than 1% [59].
- ρ – is a dish material reflectivity (0.92 for an aluminum reflector) [60].
- $\tau\alpha$ – the product of transmissivity and absorptivity. It is a loss caused by the air gap between the concentrator and the receiver. Its value ranges from 2 to 4% [59][61].
- γ – is an intercept factor, which is defined as the ratio of energy intercepted by a receiver to the energy received from the parabolic dish reflection. It could range between 97 and 99%.

The optical efficiency value estimated for this study should be 0.84, which is in the range of 0.83 to 0.85 [58].

Generally, the overall optical efficiency of the system ($\eta_{overall\ opt.}$) is the optical efficiency of the primary collector plus the optical efficiency of the secondary reflector, which is 0.682 or 68.2%.

4.7. Thermal performance of the system

A large amount of energy is released by the sun. However, only a small portion of this energy is absorbed by the earth. Due to the rotation of the Earth, any collector device located on Earth can only collect energy from the sun during certain hours of the day. Additionally, factors like the atmosphere and the efficiency of solar energy collectors can influence the amount of available solar energy.

- The available solar energy collected by an ideal collector can be expressed as:

$$Q_{sun} = DNI \times A_C \times \eta_{opt.collect} \tag{4.27}$$

Where: *DNI* – direct normal irradiance,

A_C – represents the collector area, and

$\eta_{opt.collect}$ – represents the collector's optical efficiency.

Then,

$$= 4.99kwh/day \times 220m^2 \times 0.81 = \underline{\underline{889.22kwh/day}}$$

- The total amount of thermal energy collected by the collector, regardless of losses due to convection and radiation, is:

$$\dot{Q} = DNI \times A_C \times \eta_{overall\ opt.} \tag{4.28}$$

$$= 4.99kWh/day \times 220m^2 \times 0.68 = \underline{\underline{746.95kwh/day}}$$

- The energy is converted to useful energy by an energy conversion system:

$$\dot{Q}_u = \dot{Q} \times \eta_{th,str.} \tag{4.29}$$

$$= 746.95kwh/day \times 0.41 = \underline{\underline{306.25kwh/day}}$$

- The overall efficiency of the system will be:

$$\eta_{over\ all} = \frac{\dot{Q}_u}{Q_{Sun}} \tag{4.30}$$

$$= \frac{306.25}{889.22} = \underline{\underline{0.3444}} \approx 34.44\%$$

4.7.1. Receiver Thermal Losses

The receiver of a concentrated solar plant is associated with three basic loss mechanisms; heat losses due to radiation, convection, and conduction. They are discussed as follows:

4.7.1.1. *Heat loss due to radiation*

Heat transfer due to radiation will only consider the absorbed power of the particles, their emission, and reflection. It can then be evaluated by equation (4.31):

$$\dot{Q}_{rad} = \varepsilon \sigma A_{rec} \left(T_{rec}^4 - T_{sky}^4 \right) \tag{4.31}$$

$$= 0.1 \times 5.67 \times 10^{-8} \times 0.0314(1083.15^4 - 298.15^4) = \underline{\underline{243.65\text{W}}}$$

Where: σ – is the Stefan-Boltzmann constant, A_{rec} – is the receiver area, T_{sky} – is the sky temperature which is assumed to be equal to the ambient, and ε – the emissivity of the absorber material.

4.7.1.2. *Heat loss due to Convection*

Heat loss due to a convention is estimated by using Nusselt number correlations, which depend on the magnitude of Reynolds number, Re_L, and Prandtl number, *Pr*. *Pr* for air = 0.69 and $Re_L = uL/v$, where: *u* is the wind speed in m/s, *L* is the characteristic length of the exposed hot surface (receiver diameter) in m, and *v* is the kinematic viscosity of air = 16.1 x 10^{-6} m^2/s. and all fluid properties were calculated at the temperature of 720 ^{0}C. Thus, the Reynolds number is:

$$\text{Re}_L = \frac{uL}{v} \Rightarrow \frac{2.8m/s \times 0.2m}{16.1 \times 10^{-6} m^2/s} = 34782.6 \tag{4.32}$$

For $10^3 < \text{Re} \leq 5 \times 10^5$, and $\text{Pr} > 0.5$.

The average forced convection Nusselt number on the receiver surface $\overline{Nu}_{Forced}$ can be found as follows:

$$\overline{Nu}_{Forced} = 0.664(\text{Re}_L^{1/2} \times \text{Pr}^{1/3}) \tag{4.33}$$

$$= 0.664(34782.6)^{\frac{1}{2}} \times (0.69)^{\frac{1}{3}} = 19.15$$

The average Nusselt number for Natural Convection $\overline{Nu}_{Natural}$ is also given as:

$$\overline{Nu}_{Natural} = 0.54\,(G_{rL}\ \text{Pr})^{1/4} \tag{4.34}$$

Valid for $10^5 < (G_{rL}\ \text{Pr}) < 2 \times 10^7$, and the flow is laminar.

$$\overline{Nu}_{Natural} = 0.14\,(G_{rL}\ \text{Pr})^{1/3} \tag{4.35}$$

Valid for $2 \times 10^7 < (G_{rL}\ \text{Pr}) < 3 \times 10^{10}$, and the flow is Turbulent.

Where: G_{rL} – Grashof number and it is given as:

$$G_{rL} = \frac{\beta \Delta T g L^3}{v^2} \tag{4.36}$$

$$= \frac{9.81 \times 0.00335(1083.15 - 298.15)(0.2)^3}{(16.1 \times 10^{-6})^2} = 8.43 \times 10^8$$

Where:

- ΔT – is the temperature difference between the working fluid in the receiver and the ambient fluid (ambient air) in K,
- g – is the gravitational acceleration in m/s^2,
- β – is the volumetric coefficient of expansion (for an ideal gas, $\beta = 1/T$) [1/K], and
- v – is the kinematic viscosity of the fluid in m^2/s.

$$G_{rL} \Pr = 8.43 \times 10^8 \times 0.69 = \underline{\underline{5.82 \times 10^8}}$$

For $2 \times 10^7 < (G_{rL} \Pr) < 3 \times 10^{10}$, the flow is Turbulent. And, by using equation (4.35), the of $\overline{Nu}_{Natural}$ is equal to 116.86

For mixed convection, natural, and forced convection, Nusselt numbers are combined.

$$\overline{Nu}^{3.5} = \overline{Nu}^{3.5}_{Natural} + \overline{Nu}^{3.5}_{Forced} \tag{4.37}$$

$$= (19.15^{3.5} + 116.86^{3.5})^{\frac{1}{3.5}} = 116.92$$

The convection heat transfer coefficient (in W/m^{2}K) is given by:

$$h = \frac{\overline{Nu} \cdot k}{L} \tag{4.38}$$

$$= \frac{116.86 \times 0.02705 W/m.K}{0.2m} = \underline{\underline{14.65 \text{W/m}^2\text{K}}}$$

Where k – is the conductivity of air = 0.02705 W/m K.

Hence, the convective heat loss is evaluated as follows:

$$\dot{Q}_{Conv} = hA_{rec}(T_{rec} - T_{amb}) \tag{4.39}$$

$$= 14.65 \text{W/m}^2\text{K} \times 0.0314 \text{m}^2 (1083.15 - 298.15)\text{K} = \underline{\underline{361.12 \text{W}}}$$

Where: h is the coefficient of heat transfer.

The total heat loss Q_{loss} will be:

$$\dot{Q}_{loss} = \dot{Q}_{rad} + \dot{Q}_{conv} \tag{4.40}$$

$$= (0.244 + 0.361)\text{KW} = \underline{\underline{0.605\text{KW}}}$$

The useful thermal energy ($\dot{Q}_{net}$) is an absorbed net flux at the receiver aperture. We have a total thermal energy ($\dot{Q}$) collected of 746.95kWh/day. Therefore it could be:

$$\dot{Q}_{net} = \dot{Q} - \dot{Q}_{loss} \tag{4.41}$$

$$= \left(\frac{746.95kWh}{day} \times \frac{1day}{12h} \right) - 0.60kW = \underline{\underline{61.65\text{KW}}}$$

The thermal efficiency of the receiver is performed as follows:

$$\eta_{th,rec} = 1 - \left(\frac{\dot{Q}_{loss}}{\dot{Q}} \right) \tag{4.42}$$

$$= 1 - \frac{0.60}{62.25} = 0.99 \approx 99\%$$

- Net electrical energy generation could be:

$$\dot{Q}_u = \dot{Q}_{net} \times \eta_{th,str.} \Rightarrow (61.65 \times 12)kWh \times 0.41 = \underline{\underline{303.32kWh/day}} \tag{4.43}$$

- The annual electrical energy generated by the system will be:

$$\dot{Q}_{ann.} = Q_u \times 360days \tag{4.44}$$

$$= 303.32kwh/day * 365days/yr = \underline{\underline{109.2MWh/yr}}$$

By considering three rainy sessions, the annual electrical energy generated could be 82.2MWhe. Finally, the total energy flow through the system can be summarized in the following block diagram. (See Figure 4.13).

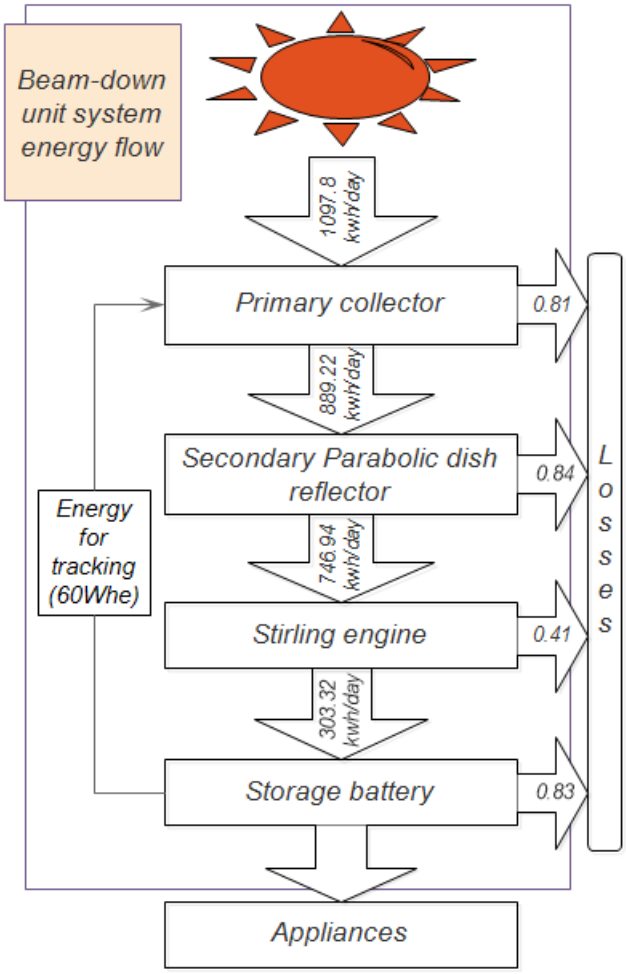

Figure 4.13: Schematic diagram of energy flow.

Therefore, the rate of heat supplied to the receiver is calculated as follows:

$$\dot{Q}_{net} = \dot{m} C_p \Delta T \tag{4.45}$$

Where: $\dot{m}$ – mass flow rate of the working fluid, C_p – is the specific heat capacity of the working fluid, and ΔT – is the change of temperature between receiver and ambient.

$$\dot{m} = \rho_{H_2} \times V_c \times \eta_v \times \frac{N}{60} (kg/\sec) \tag{4.46}$$

The density of hydrogen gas (ρ_{H2})

$$\rho_{H_2} = \frac{M_n P}{RT} \tag{4.47}$$

$$= \frac{2.016kg/mol \times 20 \times 10^6 \text{Pa}}{8.3145J/mol.k \times 993.15k} = 4.883kg/m^3$$

The volumetric efficiency of the engine is:

$$\eta_v = \frac{\text{volume of gas taken into cylinder}}{\text{max. possible volume in the cylinder (swept volume)}} \quad (4.48)$$

The engine with normal aspiration has a volumetric efficiency of 80% to 90% [62]. Therefore, the volumetric efficiency assumed for this engine is approximately 85%. Thus, the mass flow rate of hydrogen gas is calculated as follows:

$$\dot{m} = 4.88kg/m^3 \times 0.000095m^3 \times 4 \times 0.85 \times \frac{1800}{60 \times 2} = 0.024kg/\text{sec} \quad (4.49)$$

The change of temperature on the receiver was calculated by using equation (4.45):

$$\Delta T = \frac{\dot{Q}_{net}}{\dot{m} C_p} \Rightarrow \left(\frac{61.65kw}{0.024 \frac{kg}{Sec} \times 14.310 \frac{kJ}{kg.K}} \right) = \underline{\underline{180K}}$$

4.8. The energy required for tracking

The weight of the system and Aerodynamic forces affect the amount of energy that the servomotor uses during tracking. The system's weight involves the mass of the collector mirror, supports, and control system. (See Figure 4.14). By assuming the total mass of the system as 1000 kg, the weight of the system could be 9.81 KN. The direction of the wind flowing over the concentrator determines the aerodynamic force acting on the concentrator and is given by equation (4.50).

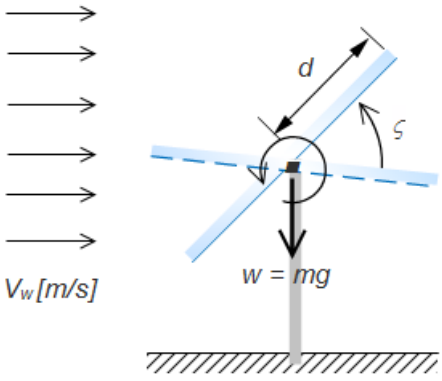

Figure 4.14: Collectors' energy balance.

$$F_a = \frac{1}{2}\rho A_c C_D V_w^2 \tag{4.50}$$

Where: ρ – represents the density of air,

A_c – concentrator area,

C_D – the aerodynamic coefficient of the heliostat collector, and

V_w – wind velocity.

Accordingly, the air density is 1.293kg/m^3, the area of the concentrator is 73.5 m^2, the aerodynamic coefficient for the heliostat collector is 1.32 [63], and the average wind velocity of the Bule Hora region is 2.8m/s, then the aerodynamic force could be 0.492KN. So, the energy required for the tracking system is estimated as follows:

$$P_{Tr} = \frac{F_t * d\left(\varsigma^0 \times \frac{\pi}{180^0}\right)}{t} \tag{4.51}$$

Where: F_t – total force (summation of weight and aerodynamic force),

t – Tracking time, and

ς – Tracking angle.

Assuming the tracking angle (ς) as 75^o, d = 5 m, and total tracking time 12hrs. The total power required for the motor to track the sun could be about 1.56W x 3 = 4.68W. The total electrical energy required could be approximately 60Whe.

4.9. Energy Storage

Solar power plant output, like that of any other power plant, must meet the needs of the utility market. Kilowatt-hour costs are high during peak demand periods, and financial incentives for guaranteed supply are strong—changes in diurnal, seasonal, and weather-related insolation limit solar plant input. To deal with these variations, the solar plant input must be backed up, or the solar changes can be regulated using a storage system. The decision is influenced by the demands, systems, and site conditions [64]. In the case of this study, the Stirling engine is the energy conversion unit, and it should cover the daily energy demand, both during daytime and nighttime. But it can only produce electricity during the daytime. Therefore batteries are implemented to supply the demand even during nighttime. It stores electrical energy as chemical energy.

The batteries are constructed from a combination of different chemicals. Their chemical composition also affects the cost and storage capacity. They are categorized as primary and secondary batteries. Only secondary batteries may be recharged, making them ideal for energy storage applications. Lead-acid and nickel-cadmium are the most regularly used rechargeable batteries. Lead-acid batteries have been used for over a century and remain the most popular batteries [65]. It provides the optimum balance of capacity per dollar and is the most frequent type of battery used in standalone power systems. More than 97% of batteries can be recycled. Batteries, as an electrochemical device, are sensitive to climate, charge or discharge history, temperature, and age. The three types of lead acid batteries that can be utilized in solar power systems are the flooded lead acid battery, the absorbed glass-sealed lead acid battery (AGM), and the gelled electrolyte-sealed lead acid battery [66],[67].

Table 4.9: Properties of some rechargeable batteries [65].

System	Electrolyte	Temp.[^{o}C]	Open cell voltage	Achievable energy density [Wh/kg]	Efficiency [%]
Lead-acid	H_2SO_4	20-30	2.05	50	75
Nickel-iron	KOH	20-30	1.35	60	55
Zinc-iron	KOH	50-60	1.65	90	45
Sodium-sulfur	β-Al_2O_3	300-375	1.76-2.08	120	75
Lithium-iron sulfide	LiCl-KCl	400-450	1.6	150	75

4.9.1. *Battery system sizing*

The capacity of a battery is defined as the quantity of energy that can be taken from a fully charged condition. The capacity of a battery is typically stated in ampere-hours (Ah) or watt-hours (Wh). To calculate how much battery capacity is necessary to run a specific appliance at a particular time, multiply the wattage of the appliance by the duration the battery is meant to be used, as shown in Table (4.1), and divide the result by the voltage of the battery.

Assumptions: Load sub-system efficiency or load factor is 0.83, and 48*v* Batteries are used.

$$\text{Required capacity per day } (Ah) = \frac{264955 wh/day}{48 volt \times 0.83} = \underline{\underline{6650.5 Ah/day}} \qquad (4.52)$$

Hence, we don't have another backup system; the days of autonomy are assumed to be 3 days, and the depth of discharge is 0.9. Then, the battery system size could be:

$$\frac{26601.71Ah/day \times 3day}{0.9} = \underline{\underline{22168.25Ah}},$$

$$21168.25\text{Ah} \times 48v = 1064076\text{W}h \approx 1\text{MWh}$$

The Lead acid battery; (model: SD-48V3000Ah/2V-L1-G) with 48*v*, 3000*Ah* is selected for this application, and the Number of batteries required is calculated as follows:

$$\frac{221668.25Ah}{3000Ah} = \underline{\underline{7.4}}$$

Approximately 8 batteries are required to run the appliance or to meet the energy demand market of the village.

4.9.2. *Battery connections*

Higher voltage with series connection: We may require a higher voltage than that provided by a single battery. It is thus possible to link batteries in series. This means that the negative terminal of one battery is connected to the positive terminal of another. For example, if we connect three 12V batteries in series, there will be 36V between the positive and negative terminals of the first and last battery, respectively.

Higher capacity with parallel connection: When more battery capacity or the ability to connect heavier loads is required, the batteries must be connected in parallel. This means that the positive terminal of one battery is connected to the positive terminal of another battery. The voltage of this connection will remain that of a single battery, but the capacity and ability to withstand larger loads will be increased. Figure 4.15 illustrates the battery connections more schematically.

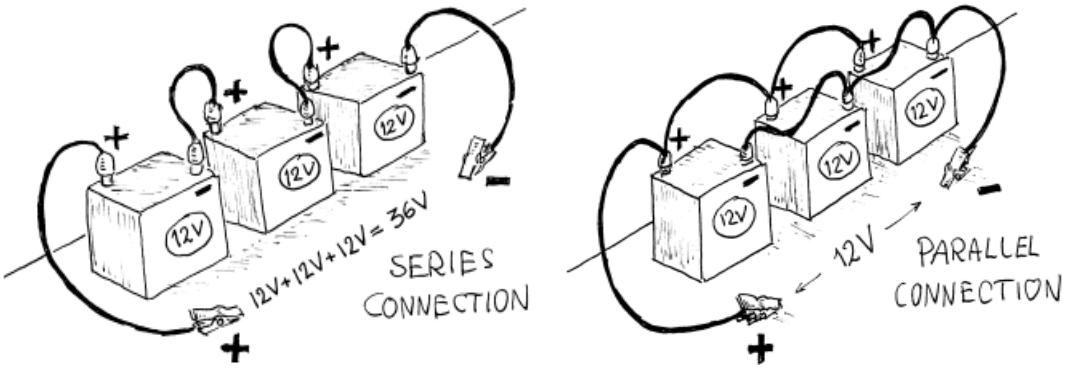

Figure 4.15: Battery connection types [68].

Note: In the case of non-professional batteries and installations, it is not suggested to run more than 3-4 batteries in parallel. Otherwise, a single faulty cell may destroy the entire battery bank. To provide the best total lifetime, all batteries should be the same age and size. Finally, Table 4.11: Summarizes the specification of the storage battery decided to be used for the designed system.

Table 4.10: Information about the battery used in the model. [*https://itprice.com/sheet*]

Battery specification	
Battery type	Lead acid **(**SD-48V3000Ah/2V-L1-G)
Battery Voltage	48*v*
Battery size	3000*Ah*
Numbers of batteries	8
Connection	Series

4.9.3. *Inverters (converters)*

An inverter is a device that converts direct current (DC) to alternating current (AC) [69]. DC to AC converters are classified into three types. There are three types of sine waves: square waves, modified sin waves, and pure sin waves. The square wave type is the simplest and least expensive of these three inverters, however, it has low quality. The modified sine wave inverter is suited for a wide range of load types and has a low cost. Pure sin wave inverters generate high-quality signals and are mostly employed in sensitive devices such as medical equipment [70]. An inverter's average efficiency is 95.5% [71].

We have the total required power per day = 45680 watts (see table 4.1). And according to NEC, inverters should be 25% to 30% high. (Therefore, the assumed safety factor = 1.25). The required inverter power is calculated as follows:

$$\text{Required inverter power} = \frac{total\,power\,required \times\ factor\,of\ safety}{Invertor\,efficiency} \tag{4.53}$$

$$= \frac{45680watt \times 1.25}{0.95} = \underline{\underline{60105.26watt}}$$

Then, the power required from the inverter is approximately 60kW. And pure sin wave inverter was selected for this work.

4.9.4. *Charge controller*

The charge controller is a key component of solar home systems that controls the energy flow into and out of the battery bank. It avoids overcharging and deep draining, extending the battery's life. For a solar home system, a typical charge controller has an efficiency of 85% [72].

The charge controller current is normally calculated from the battery bank voltage (v) and total solar power system output (W).

$$\text{Charge controller current} = \frac{total\ solar\ power\ output\ (w)}{Battery\ bank\ voltage\ (v)} \tag{4.54}$$

$$= \frac{(303.32 \times 1000)Wh \div 12h}{48v} = \underline{\underline{526.60\,Amp}}$$

4.9.5. *Charging lead-acid batteries: Float charging*

Lead-acid batteries are continually charged at a constant voltage in float charging. In order to account for self-discharge, only the current required to keep the voltage constant is supplied. This approach has the benefit of giving the proper charge current regardless of the size of the battery, decreasing the probability that the battery would be overcharged.

Since the battery is parallelly connected to a rectifier and inverter, electricity can be delivered during a power failure without being interrupted. These systems also have the benefit of being able to deliver a steady supply of power despite voltage fluctuations in the main power supply or unexpected surges in the load's power requirements since the battery acts as a buffer [73].

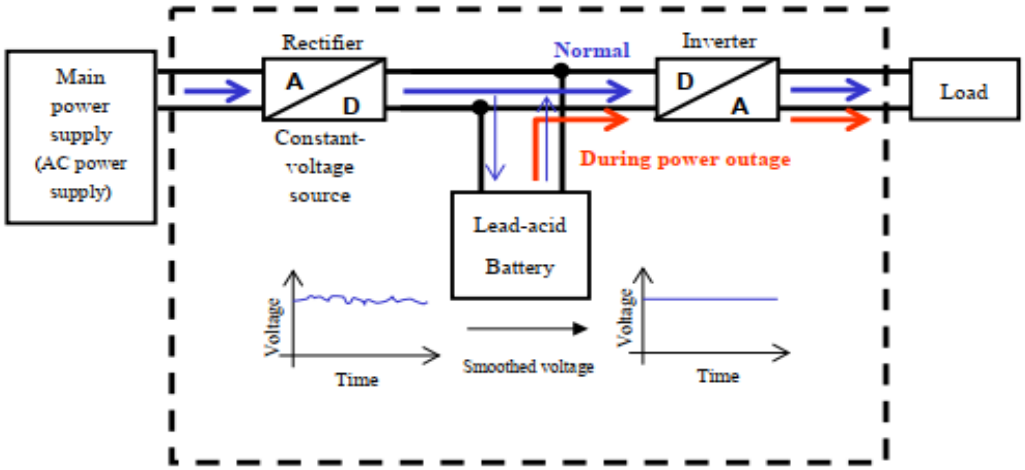

Figure 4.16: Continuous inverter power supply type UPS [73]**.**

4.10. Tonatiuh (Version 2.2.4)

Tonatiuh v 2.2.4 is used to model the power system module optically. It was created by the National Renewable Energy Centre of Spain (CENER) in partnership with the University of Texas at Brownsville (UTB), with assistance from the National Renewable Energy Laboratory (NREL) [74]. Tonatiuh uses the MCRT method to perform simulations, and it can model all the systems that use the sun as the source.

At first, TracePro was planned to be used for optical modeling. But Tonatiuh v 2.2.4 is chosen due to its ease of use and user-friendly interface. (See Figure 4.17)

Note that one can enter the parameters (reflectivity, diameter, aperture width, absorptivity, azimuth, etc.) of the components (primary collector, secondary dish reflector, sun, etc.) and also see the 3D model of the object at the same time. However, this is not as easy as Tonatiuh with Tracepro. Moreover, Tonatiuh uses a tree structure similar to CAD programs, making the model very organized and easy to work with. Figure (4.18) shows a flow chart of ray tracing and flux analysis during software operation.

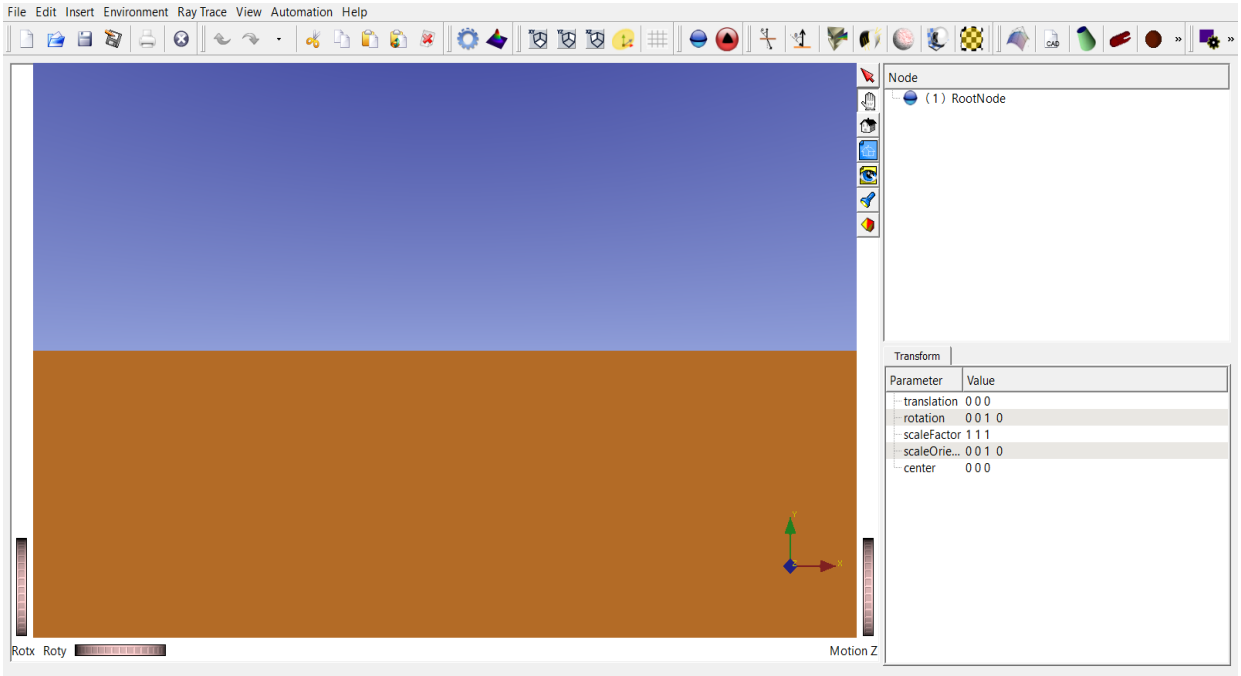

Figure 4.17: The user interface of Tonatiuh_V 2.2.4.

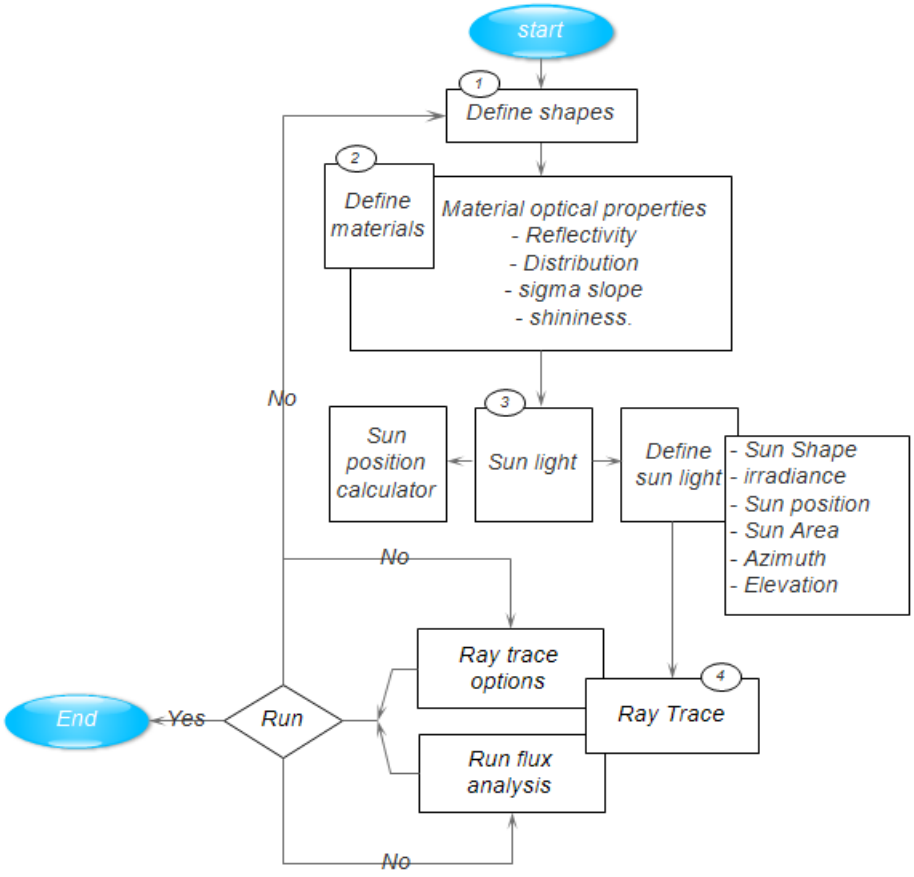

Figure 4.18: Flow chart of ray tracing and flux analysis simulation using Tunatiuh.

Table 4.11: Input parameters for Tonatiuh ray tracing software.

Parameters	**Value**
Model components	Primary collector, secondary reflector (dish), tertiary reflector (CPC), and receiver (flat plate).
Materials optical properties	Specular standard materials
Sun shape	Pillbox
Irradiance	1000 W/m^2
Azimuth	0^0
Elevation	90^0
Number of rays	10^3 to 10^8

4.11. Economic feasibility study of the system

The feasibility study is one of the research tools to answer the research questions. This section answers most of the questions asked by decision-makers about the feasibility of the projects. The levelized cost of energy (LCOE) is the most commonly used parameter for the feasibility study of solar thermal power plants. Equation (4.55) is used to estimate the LCOE of the CSP technologies. The formula considers the initial cost of the generation facilities, annual maintenance and operating (M&O) costs, and the facility's estimated life. The LCOE formula, for ($t = 1, 2, 3... n$) in dollars per kWh is given by;[75].

$$LCOE = \frac{\sum_{t=1}^{n} \frac{C_t + A_t}{(1+d)^t}}{\sum_{t=1}^{n} \frac{E_t}{(1+d)^t}} \tag{4.55}$$

Where: C_t – capital investments made in year t

A_t – annual maintenance and operating costs for year t

E_t – the amount of electricity generated in year t

n – Expected life of the facility

d – Discount rate (cost of capital)

In this study, the LCOE (in US$/kWh) was illustrated as a main economic indicator. To investigate the LCOE of renewable energy systems, the inflation rate, discount rate, and other factors are taken into consideration. According to the National Bank of Ethiopia, currently, the inflation rate is 33.5%. Finally, it was found that the facility would be the short-term best CSP technology with the lowest LCOE of 0.11 US$/kWh. According to Zhang H.L. et al.[76] The levelized electricity cost (in US$/kWh) of 50MW PTC with oil and SPT with steam, both without thermal storage and backup, were (0.17 – 0.21) US$/kWh and (0.19 – 0.25) US$/kWh, respectively. Therefore, comparatively, the facility is economically feasible. Table (4.12) summarizes the economic input parameter of the newly proposed system.

Table 4.12: The financial parameters of the beam-down system [77] [78] [79].

Factors	
Inflation rate	0.34
Capacity factor	0.25
Annual energy [MWh]	110
The expected life of facility [yrs.]	30

Total investment cost	**Specific Cost [$]**	**Plant parameters**	**Total cost [$]**
Direct cost			
Site improvement	0.65 USD/m^2	2,500 m^2	1,625
Primary collector (heliostat facets Mirror's Module)	23.6 USD/m^2	220 m^2	5,192
Cost of secondary reflectors	322.79 USD/m^2	9.62 m^2	3,105.24
Tertiary reflector (CPC)	100 USD/m^2	2 m^2	200
Steel supporting structure	6.75 USD/m^2	275 m^2	1,856.25
Pedestal	16.96 USD/m^2	3(quantity)	127.2
Derive and controls	3.38 USD/m^2	3(quantity)	10.14
Engine cost	300 USD/kW	25.5 Kw	7,650
Storage battery	1,900 USD	8(quantity)	15,200
Invertor (converter)	493.86 USD	1(quantity)	493.86
Total direct cost			**35,458.83**
Indirect cost			
Engineer, procure, and construct	11%(direct cost)		3,900.47
Other miscellaneous costs	2%(direct cost)		709.18
Total indirect cost			**4,609.65**
Total (indirect +direct) cost			**40,068.5**
Operation and maintenance cost			
Total (M&O) cost	1% (investment cost)		**400.68**

Another important factor in the economic analysis of the system is the payback period (PBP), which is defined as the number of years required to recover the whole cost of the project. This study refers to the critical period for receiving a monetary return on beam-down solar system investment. It can then be calculated as follows [80]:

$$PBP = -IC + \sum_{t=1}^{\rightarrow n} \frac{CF}{(1+i)^t} \tag{4.56}$$

Where: *CF* is cash flow for year *t*, *i* is the yearly interest rate (According to NBE, *i* = 7%), and *IC* is the initial cost.

The system has been predicted to produce 82.2MWh of electricity annually and sold for 0.11US$/kWh. Which is an input to the economic model that implies the electricity generated in the first year (Year 1) of the project's cash flow. The total annual generated electricity for year 2 and above is calculated as follow:

Electricity yield in year $n_{n>1}$ = [Electricity yield in Year (n –1)] × (1– degradation rate) (4.57)

The *degradation rate* is the annual percentage decrease in system output from the system's total annual output. For instance, degradation rate = 0.5% means, the system's output decreases by 0.5% each year from the previous year's generation [81]. By using equation (4.57) electricity yield from year-1 to 7 is calculated as in the table below:

Table 4.13: The economic model of the system designed.

Years	1	2	3	4	5	6	7	…*n*
Annual electricity yield [kWh]	82200	81789	81380	80973	80568	80165	79764.5	…
Cash flow[US$]	9042.00	8996.80	8951.80	8907.04	8862.50	8818.12	8774.10	…

Again, by using equation (4.56) the following cash flow diagram was built, and the payback period (PBP) is found to be 5 years and 8 months.

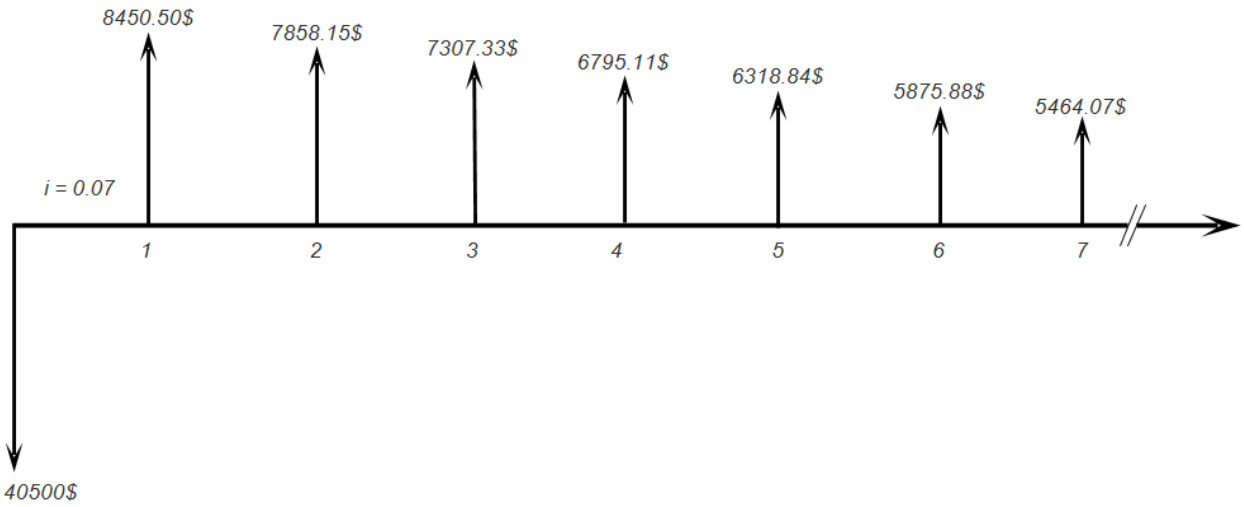

Figure. 4.19: Cash flow diagram of the investment.

CHAPTER FIVE

5. RESULT AND DISCUSSION

5.1. Solar radiation resource

5.1.1. *Area solar radiation*

The area solar radiation tool; is a tool for spatial analysis that extracts sun radiation from a raster surface. This is a tool in ArcGIS. For this study, ArcMap 10.3 is used to run the area solar radiation tool on a DEM layer in Bule Hora. The result is shown in Figure (5.1) that the output raster "BH_Area Solar radiation" has units of watt hours per square meter [Wh/m^2] and represents the global radiation calculated for all surfaces. According to this classification, three places have been distinguished with very good potential (i.e., which is depicted with a deep brown color) to test the proposed system.

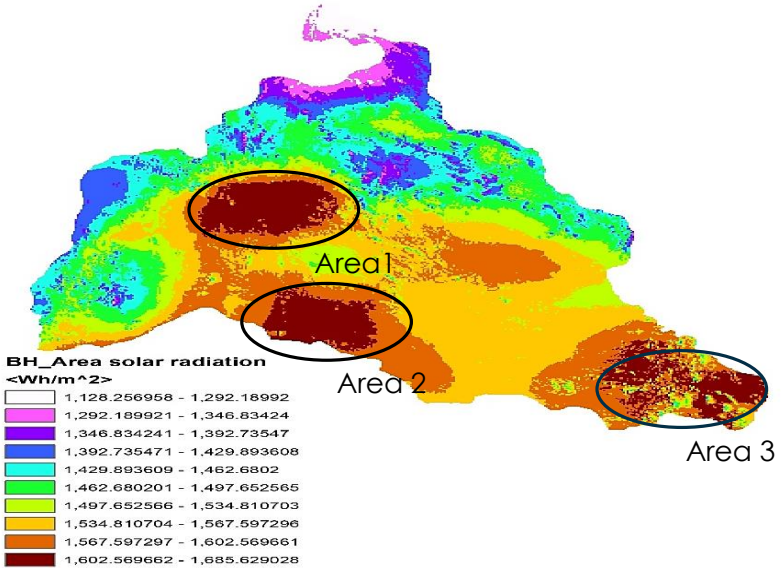

Figure 5.1: Areal solar radiation.

5.1.2. *Sunshine duration*

The sunshine duration is a very important variable parameter for estimating the radiation of a particular area. Sources like *Newloc_clim* and *Meteonorm* provide the sunshine duration on the base of the coordinate of the given location. The sunshine duration of the area selected for study is high during the three successive months of the winter session. As shown in Figure (5.2); the maximum and the minimum sunshine duration are recorded in January and July, respectively.

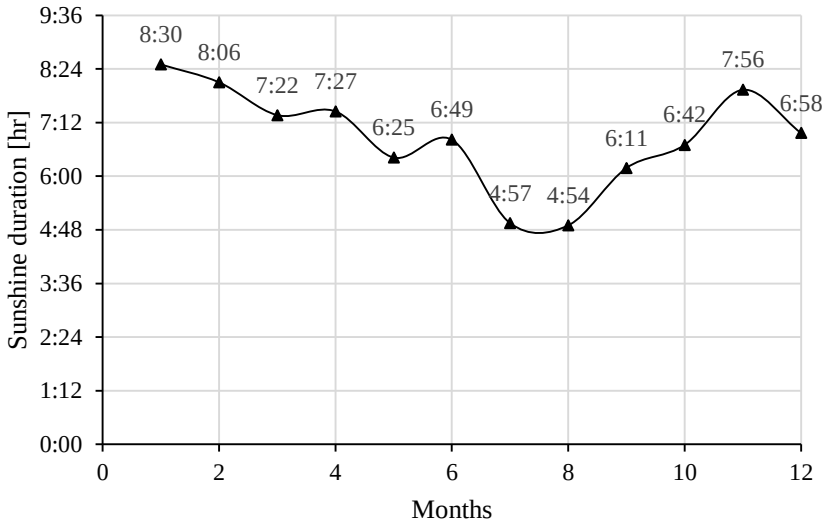

Figure 5.2: Sunshine duration variation throughout the year.

5.1.3. *Available solar radiation*

As depicted in Figure 5.3, the graph of beam radiation or DNI lies above 5 kWh/m^2/day for at least five months. Also, the value of global radiation is greater than 5 kWh/m^2/day other than for two months, from June to August, which is greater than 4.5 kWh/m^2/day. So, the estimated result indicates that a site has significant beam solar irradiance potential for small-scale power generation.

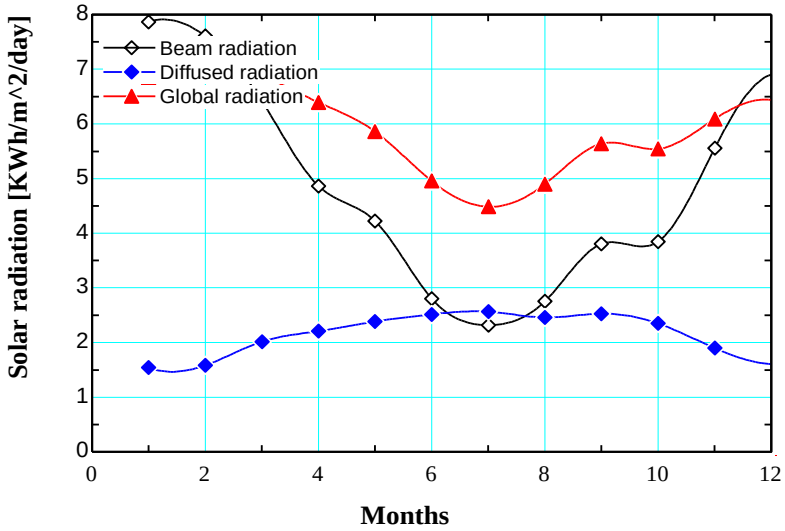

Figure 5.3: Monthly average daily global, beam, and diffuse radiation.

Figures (5.4 & 5.5) present the total global irradiance and the clearness index obtained by the Angstrom-Prescott (1940) correlation from sun-shine duration. The validation for this was carried

out by using data generated from Retscreen, Meteonorm, and Solargis. The graph depicted in black is; the predicted average solar radiation of the Bule Hora region, which is a good agreement with the data generated from different databases. From these graphs, it is visible that the radiation gets lower during the three rainy months.

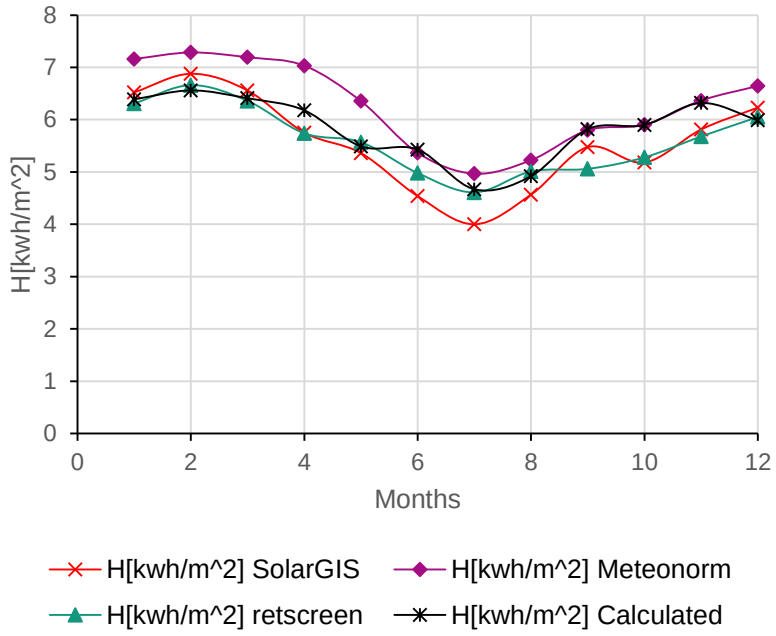

Figure 5.4: Solar radiation of the study area.

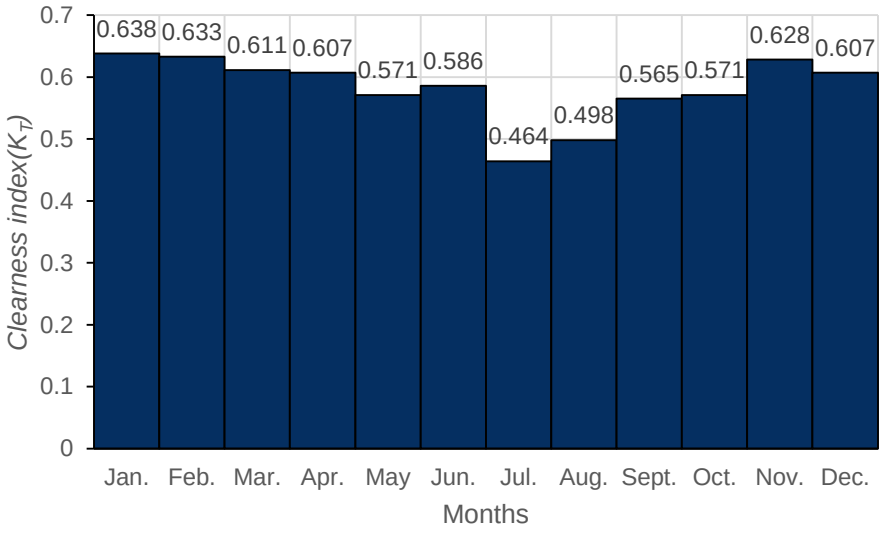

Figure 5.5: Clearness index.

While Figure (5.6) presents the comparison of monthly average daily beam radiation data provided by different databases and the direct normal irradiance (DNI) data generated from PVGIS©EU,

NSRDB, Solargis, and Meteonorm, the estimated monthly mean daily direct normal radiation (DNI) by using PVGIS is found to be 4.75 kWh/m^2/day. The average minimum and maximum monthly mean daily DNI is 3.96 kWh/m^2/day and 6.37 kWh/m^2/day for NSRDB and Meteonorm, respectively. In the case of Solargis, it is also found to be 4.57 kWh/m^2/day. These results are almost close to each other. Generally, the yearly average daily DNI resource for the study area is estimated to be 4.99 KWh/m^2/day.

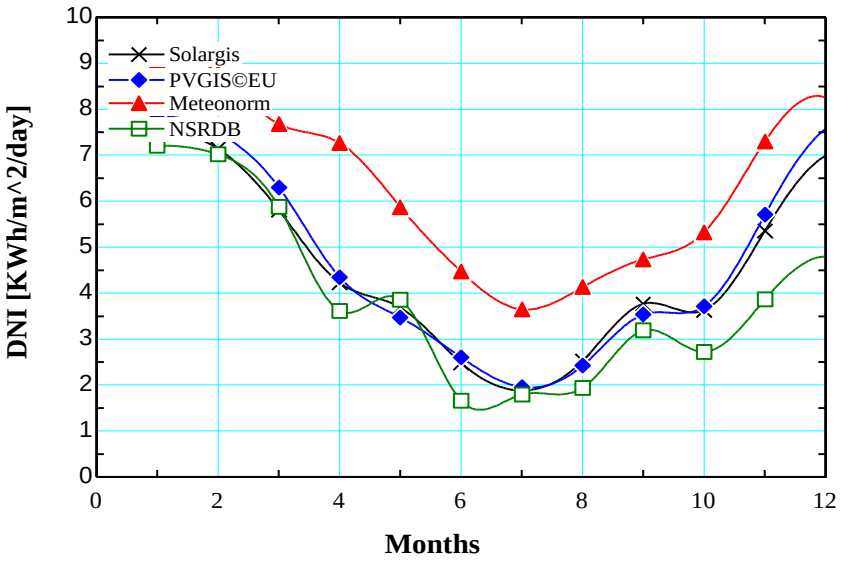

Figure 5.6: Monthly average daily beam radiation from different sources.

A view of the resource data for the selected site is generated in PVGIS 2022. Figure (5.7) shows the average daily irradiance at (TUC+3). It appears that the irradiances are depicted by colors that are labeled on the legend. The maximum value for all average daily solar irradiance is high at noon time.

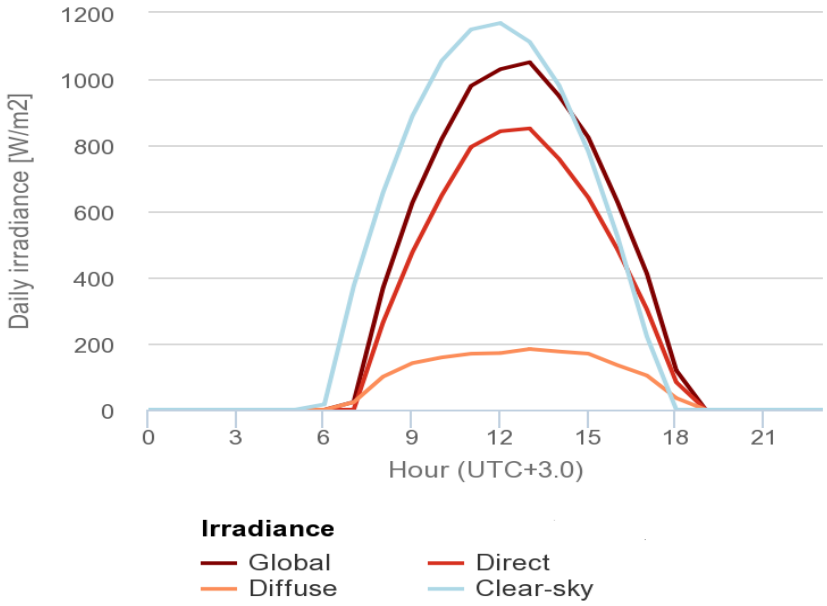

Figure 5.7: Daily irradiance profile.

As stated in section (4.1); the time selection was midday during the spring or autumn equinox for design purposes. Figure (5.8) presents the variation in daily beam irradiance (DNI) during four representative days. According to this graph, the peak DNI value is registered at noon time for the spring equinox and winter solstice, while for the fall equinox and winter solstice before and after noon respectively. The spring equinox, which is depicted in black, best fits the design point day relatively.

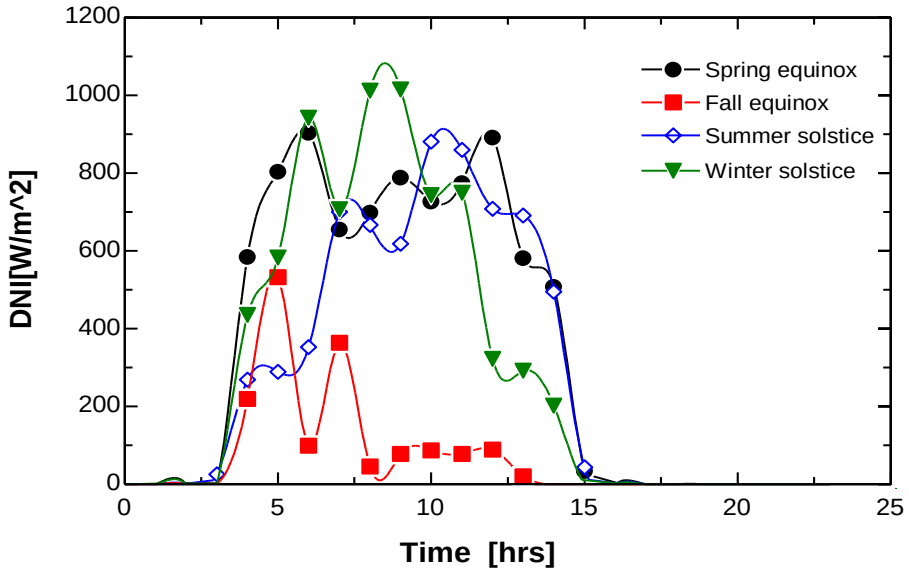

Figure 5.8: Clear sky DNI values at location 5°35′N, 38°15′E.

5.2. Climate data

Other environmental conditions, such as ambient air temperature and wind speed change, are known to have an impact on the effectiveness of solar concentrators. The change in monthly ambient air temperature for the study area is depicted in Figure (5.9).

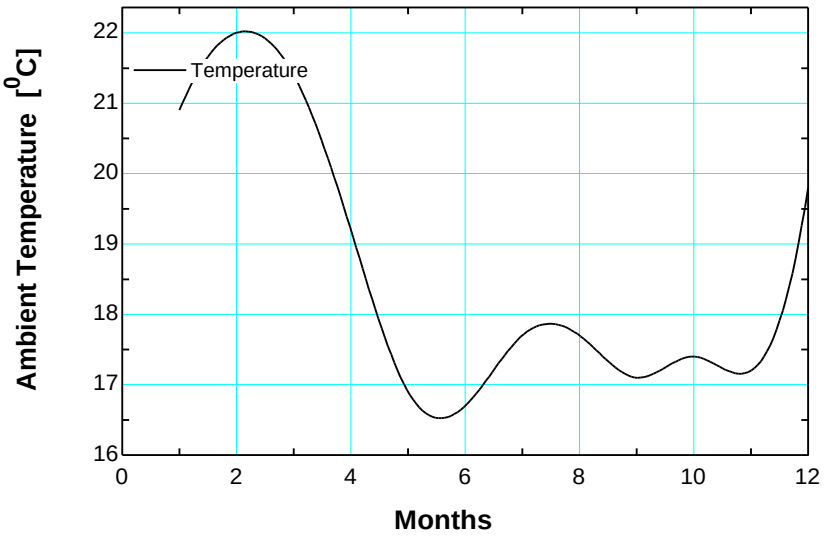

Figure 5.9: Monthly temperature vibration of the study area.

The average monthly wind speed in the Bule Hora region varies dramatically throughout the year. Figure (5.10) shows that the average yearly wind speed varies between 2.2 (m/s) and 3.8 (m/s), with the winter season being the windiest in this location.

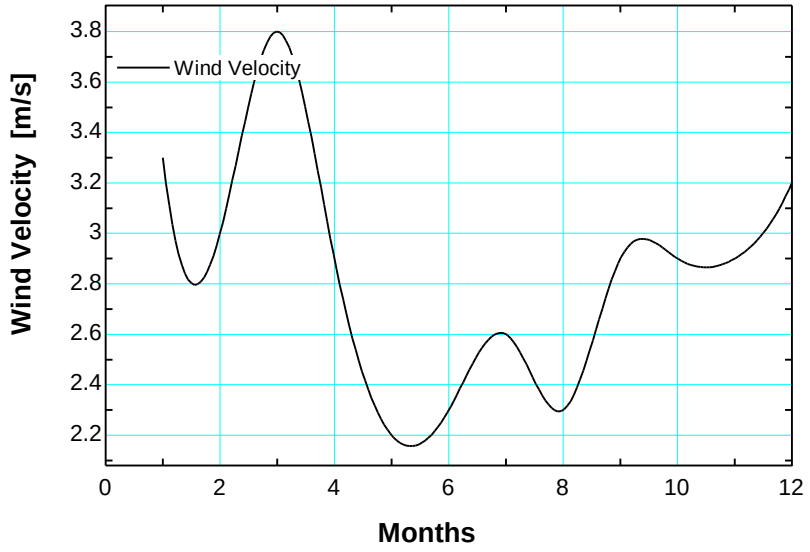

Figure 5.10: Monthly wind speed vibration of the study area.

It is worth noting that each of the curves depicted in Figures (5.9 & 5.10) indicate the average monthly changes, with the meteorological data depicted in those figures having a direct impact on numerical simulation outcomes.

5.3. The output of the System

Figure (5.11) illustrates the temperature change on the receiver during design point day (March 21) from morning to afternoon. In the meantime, the change of receiver temperature goes beyond 350K, which can best fit the engine operating temperature for generating power, and it has a good agreement with the calculated mean temperature of the receiver. The status of power generation during this day is also depicted in Figure (5.12). The graph shows that the power that can be generated by this system on this day at a mean productive time ranges from 30kW to 50kW. Therefore, the system can meet the energy demand of the selected area.

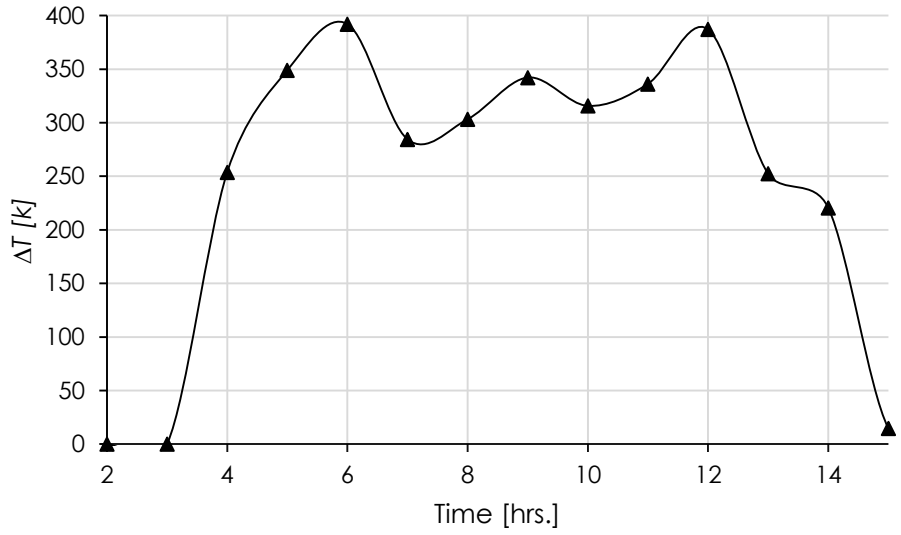

Figure 5.11: Daily receiver temperature

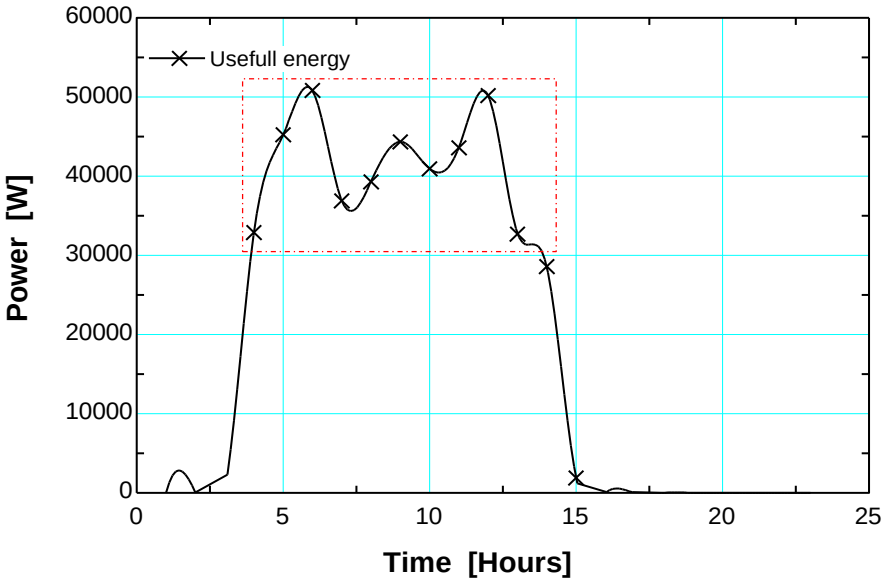

Figure 5.12: Daily energy output profile of design point day.

To be more reliable, the output energy during representative days is estimated. Figure (5.13) shows the energy that can be generated from the system during representative days. According to this graph the amount of energy generated is too high on 17 – January when compared to other representative days, and it goes more than 60 kWh. The lowest energy generated is recorded during 17 – July and 16 – August, and occasionally it drops below 10kWh.

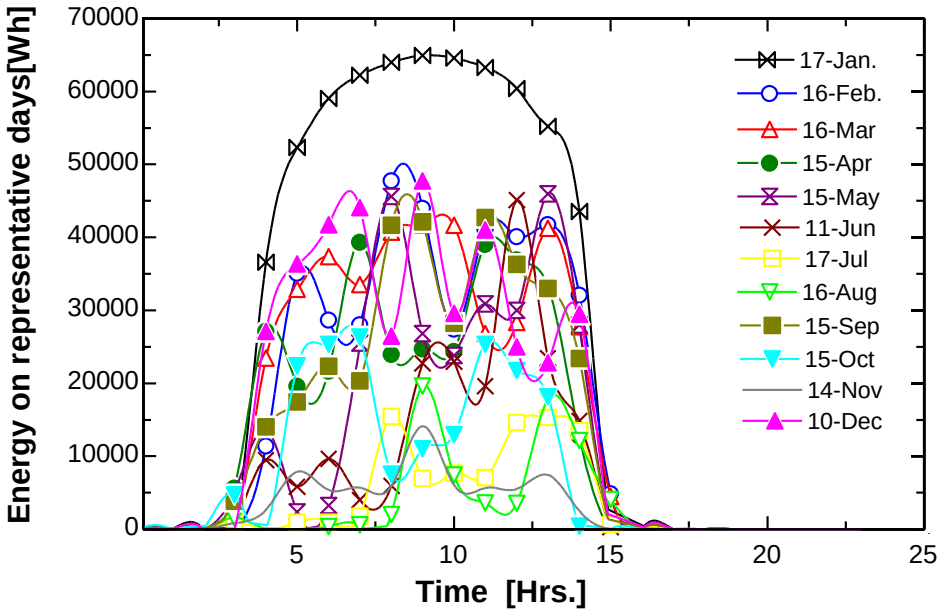

Figure 5.13: Energy during representative days

Figure (5.14) presents the average monthly solar energy variation. According to this graph, the monthly average energy; that can be generated varies from around 4.75 MWh/m^2/day in the rainy month of July to just 15.4 MWh/m^2/day in the dry months. During the rainy season (June, July, and August), it gets lowered; that is due to climate change.

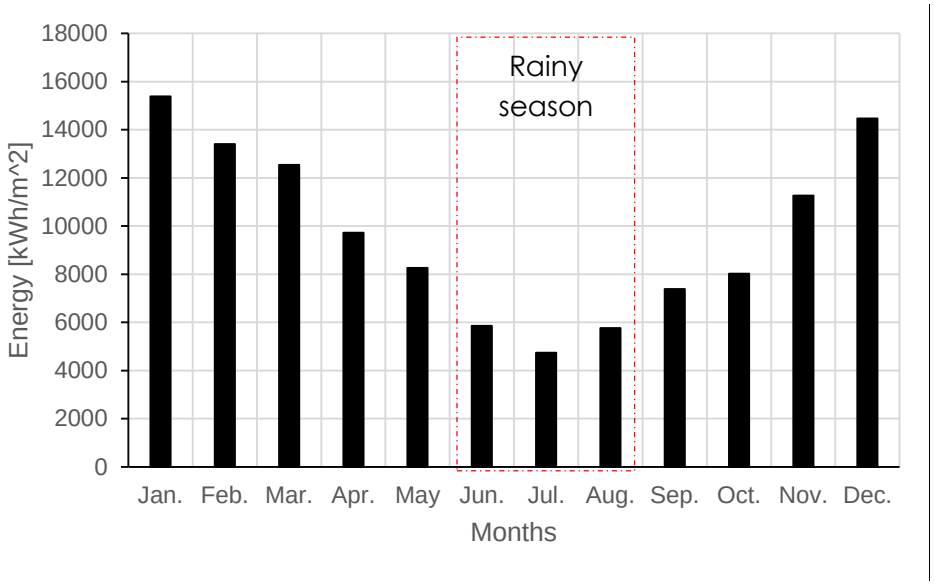

Figure 5.14: Monthly average yearly energy estimation.

5.4. Simulation results

5.4.1. *Tonatuih simulation result*

The simulation result gives the flux distribution on the virtual point that has been added to the model at the end of CPC (on the receiver). The time used for this simulation or design point is the 21st of March 2022 at noon, UTC+3. Figure (5.15) shows the distribution of the ray intercepted at the focal point of the beam-down system. At the same time, Figure (5.16) illustrates the distribution of heat flux at the focal point of the system. The heat flux is apparent to be high near the absorber center and somewhat decreasing towards the edge. For 1000 W/m^2 of beam solar radiation and 10^8 numbers of rays, the heat flux reaches 180 kW/m^2 at the center of the receiver and 30 kW/m^2 at the absorber edge.

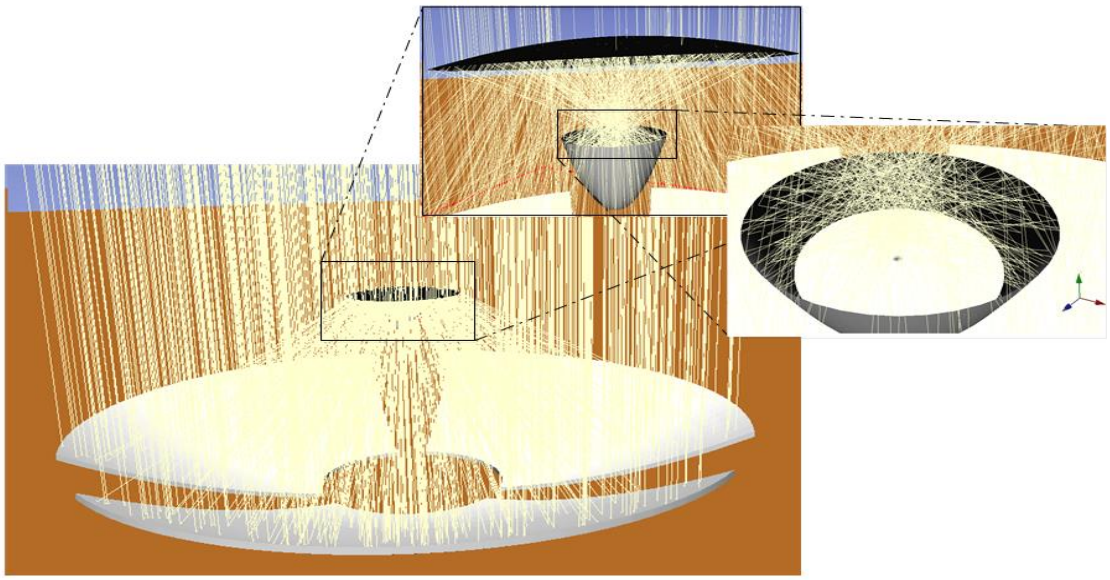

Figure 5.15: Ray intercepted at the focal point.

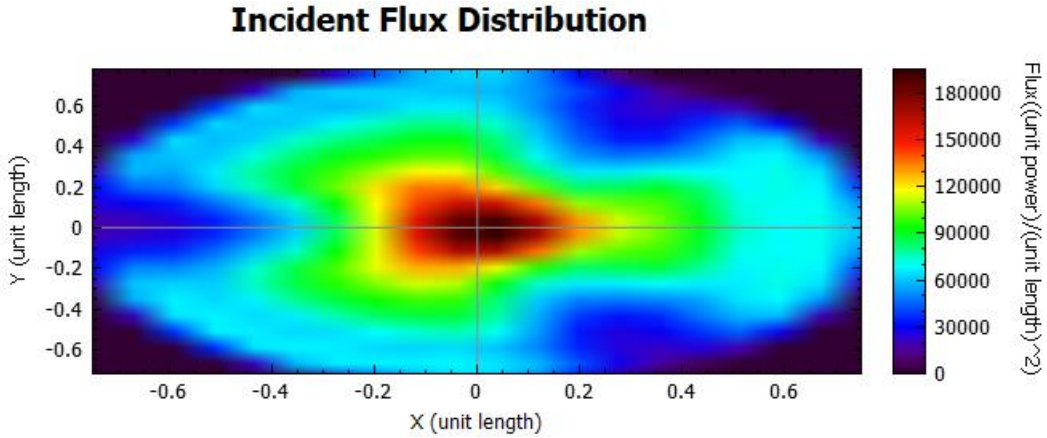

Figure 5.16: Heat flux distribution on the focal point.

The simulation was run on a model by considering the number of rays as a variable function. So, it varied from 10^3 to 10^8. During those simulations, it was shown that the total power output increased with the number of rays. See Figure (5.17). At the same time, the error decreases when the number of rays increases; at the maximum iteration, it was about 0.00755. See Figure (5.18).

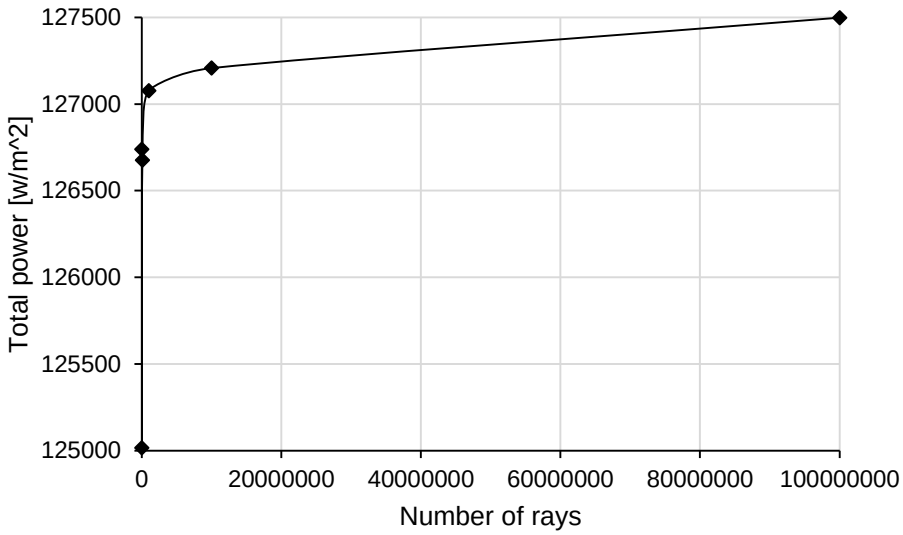

Figure 5.17: Total power variation with the number of rays

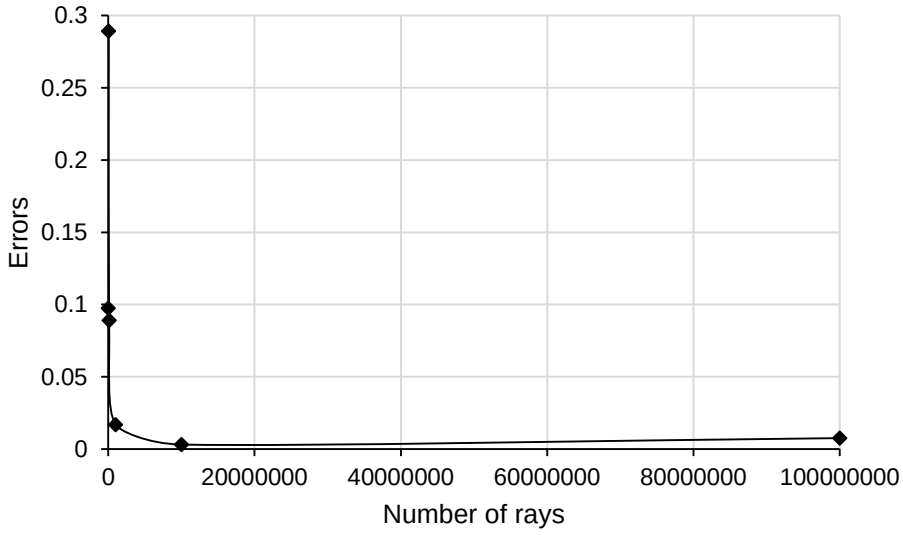

Figure 5.18: Error of rays during simulation

Finally, as shown in Figure (5.18), the total power and average heat flux have a linear relationship.

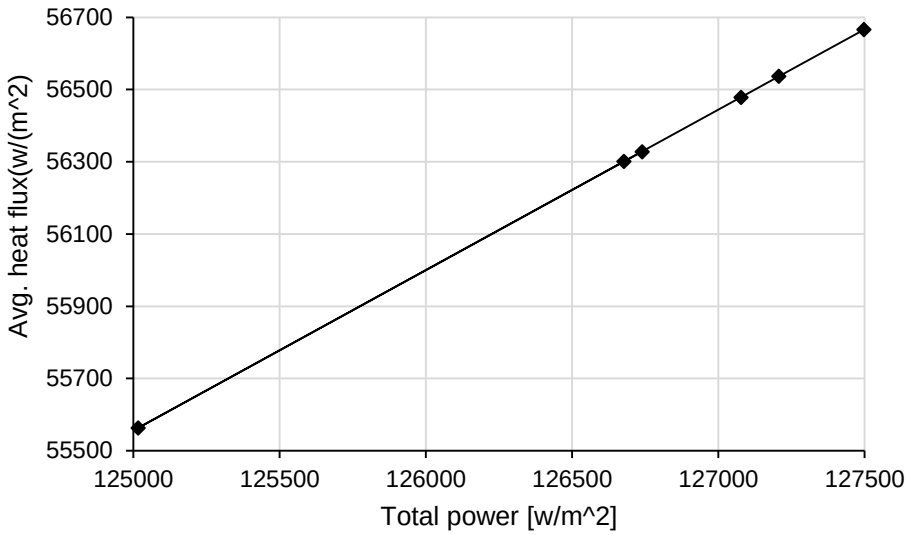

Figure 5.19: Relationship between Average heat flux and total power.

5.4.2. *Mathlab simulation result*

As mentioned in section (4.9), the battery bank consists of seriously connected eight lead acid batteries with 48V and 3000Ah capacity. As a result of solar irradiance fluctuation the main power supply from the Stirling engine will be not constant and this condition can impact the state of battery charging. By taking this into account the charging conditions must be evaluated. Figure (5.20) represents the battery bank equivalent circuit Math lab Simulink. The model was built by Matlab R2022b, and it is aimed to evaluate the state of charge (SOC) at constant current and voltage during the charging. Figure (5.21). The simulation result shows that the state of charge is high at the beginning and slightly decreases as time goes longer. From this, we can conclude that there is a healthy charging condition.

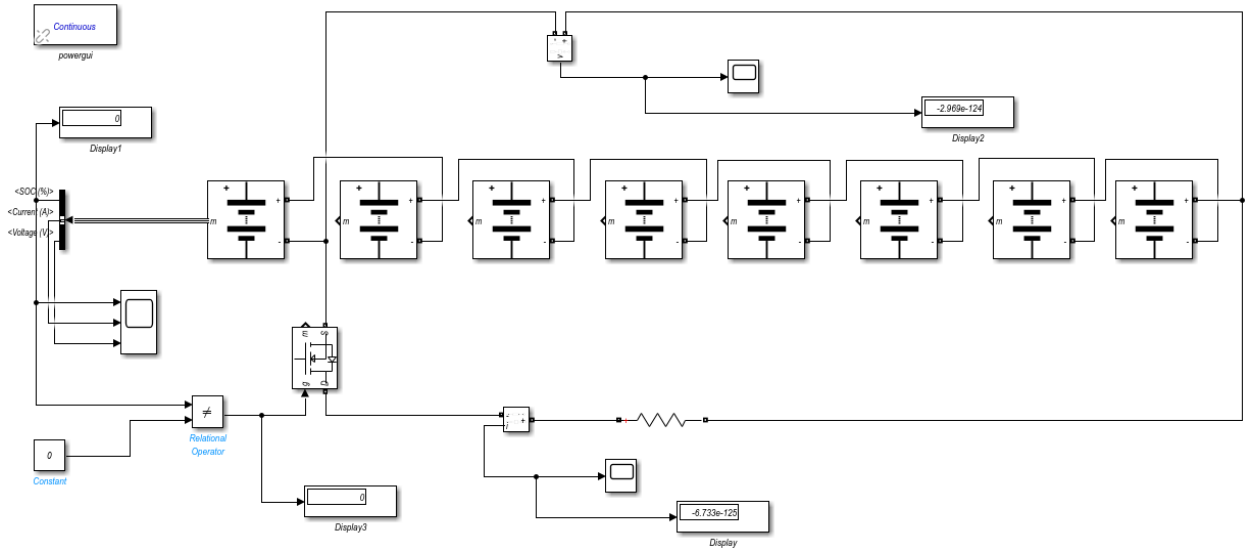

Figure 5.20: Battery package design.

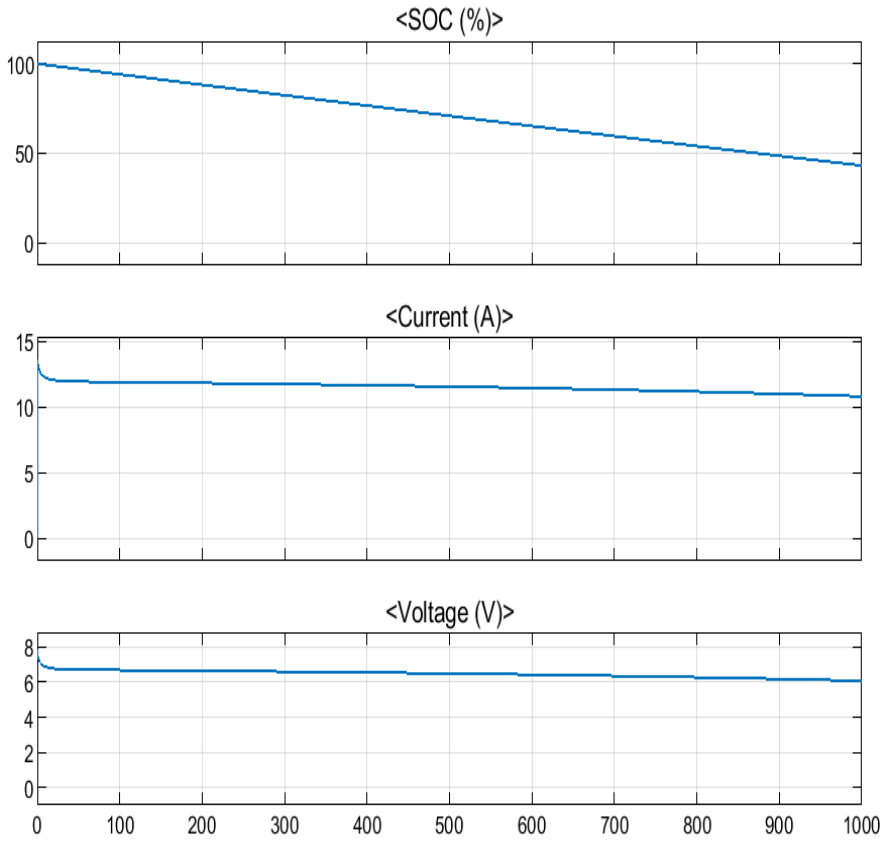

Figure 5.21: State of charge, current, and voltage variation.

CHAPTER SIX

6. CONCLUSION AND RECOMMENDATION

6.1. Conclusion

This paper presents the design of a small-scale solar-stirling power system with a beam-down focus for rural electrification. The work includes weather data estimation in the study area, design, and analysis of point focus beam-down system performance at different operating conditions, area solar radiation (Arc Map 10.3), tonatiuh v2.2.4 simulation of the system designed, and the selection of optimum Stirling engine, size of the battery, and economic feasibility of the system.

The following conclusions were drawn from this work.

- The area has good solar radiation potential for rural electrification, and the estimated solar data exhibits consistency when compared to various software.
- The energy demand assessment for households of specified rural villages was estimated at 265 kWh/day.
- The total amount of electrical energy that can be generated by the newly designed system was estimated as 303.32 kWh/m^2/day. That can meet the needs of a village.
- A unique geometrical optical model was developed to investigate the causes of optical errors, and sun shapes on concentration quality.
- Heat flux at the focal point of the concentrator increases with increasing beam solar radiation. For 1000w/m^2 of DNI and 10^8 rays, The average flux intensity distribution at the concentrator receiver reaches 56.65 kW/m^2
- The Levelized cost of energy (LCOE), which is one of the economic indicators of energy investment, is about 0.11US$/kWh.

6.2. Recommendation

This work has shown that the newly designed (Beam-Down) system can be a viable option to power rural areas from different perspectives. Furthermore, the following recommendations can be addressed for future research work in this field.

- The collector design requires more investigation. The wind pressure affects the concentration quality of the collectors as a result of the collector's wider area. Hence, different designs, as well as other mechanisms to minimize wind effects, have to be considered.
- During the rainy season (June, July, and August), the output power gets lowered due to climate change. Therefore, another backup source of power was recommended for this season.
- Finally, the system was recommended to be tested by installing it in distinguished places to achieve the final goal of powering rural areas.

REFERENCES

[1] S. Yunn, Y. Asako, T. Suwa, L. Ken, N. Bazila, and J. Oktavia, "Performance of a small-scale solar cogeneration system in the equatorial zone of Malaysia," *Energy Convers. Manag.*, vol. 184, no. October 2018, pp. 127–138, 2019, doi: 10.1016/j.enconman.2019.01.059.

[2] WORLD ENERGY COUNCIL, "World Energy Resources | 2016," 2016.

[3] A. A. Adenle, "Assessment of solar energy technologies in Africa-opportunities and challenges in meeting the 2030 agenda and sustainable development goals," *Energy Policy*, vol. 137, no. October 2018, p. 111180, 2020, doi: 10.1016/j.enpol.2019.111180.

[4] RES4Africa, "INTEGRATION OF VARIABLE RENEWABLE ENERGY IN THE NATIONAL ELECTRIC SYSTEM OF ETHIOPIA," 2019.

[5] M. H. Ahmadi *et al.*, "Solar power technology for electricity generation: A critical review," *Energy Sci. Eng.*, vol. 6, no. 5, pp. 340–361, 2018, doi: 10.1002/ese3.239.

[6] K. Lovegrove and W. Stein, "Introduction to concentrating solar power (CSP) technology," 2012.

[7] R. Meligy, M. Rady, A. El Samahy, W. Mohamed, F. Paredes, and F. Montagnino, "Simulation and control of linear Fresnel reflector solar plant," *Int. J. Renew. Energy Res.*, vol. 9, no. 2, pp. 804–818, 2019.

[8] D. Mills, "Advances in solar thermal electricity technology," *Sol. Energy*, vol. 76, no. 1–3, pp. 19–31, 2004, doi: 10.1016/S0038-092X(03)00102-6.

[9] A. A. Admasu, "SOLAR PV BASED RURAL ELECTRIFICATION IN REMA RURAL VILLAGE," KTH industrial engineering and Management, 2010.

[10] M. Dorothal, "Solar Report," 2019.

[11] G. T. Tucho and S. Nonhebel, "Alternative energy supply system to a rural village in Ethiopia," *Energy. Sustain. Soc.*, vol. 7, no. 1, 2017, doi: 10.1186/s13705-017-0136-x.

[12] D. Hipoldina, B. C. Cuamba, and A. J. Leão, "A Review on Renewable Energy Systems for Irrigation in Arid and Semi-Arid Regions," *J. Power Energy Eng.*, pp. 21–58, 2019, doi: 10.4236/jpee.2019.710002.

[13] E. W. Ramde, E. T. Tchao, Y. Atsu, K. Fiagbe, J. J. Kponyo, and A. S. Atuah, "Pilot Low-Cost Concentrating Solar Power Systems Deployment in Sub-Saharan Africa : A Case Study of Implementation Challenges," *sustainability*, 2020.

[14] R. Islam, A. B. M. N. Bhuiyan, and M. W. Ullah, "An Overview of Concentrated Solar Power (CSP)Technologies and its Opportunities in Bangladesh," *ECCE 2017 - Int. Conf. Electr. Comput. Commun. Eng.*, no. January 2019, pp. 844–849, 2017, doi: 10.1109/ECACE.2017.7913020.

[15] Y. M. Seshie, K. E. N'Tsoukpoe, P. Neveu, Y. Coulibaly, and Y. K. Azoumah, "Small scale concentrating solar plants for rural electrification," *Renew. Sustain. Energy Rev.*, vol. 90, no. February, pp. 195–209, 2018, doi: 10.1016/j.rser.2018.03.036.

[16] P. D. Sonawane and V. K. B. Raja, "An overview of concentrated solar energy and its applications," *Int. J. Ambient Energy*, vol. 0, no. 0, pp. 1–6, 2017, doi: 10.1080/01430750.2017.1345009.

[17] A. Luzzi and K. Lovegrove, "Solar Thermal Power Generation," *Encycl. energy*, vol. 5, pp. 669–683, 2004.

[18] S. A. Kalogirou, *Solar Energy Engineering Processes and Systems Second Edition*, Second. 2014.

[19] O. Scheffler, "Optimization of an Optical Field for a Central Receiver Solar Thermal Power Plant," 2015.

[20] A. Technology, "The Knowledge Mapping of Concentrating Solar Power Development Based on Literature Analysis Technology," 2020.

[21] M. S. Răboacă *et al.*, "Concentrating Solar Power Technologies," pp. 1–17, 2019, doi: 10.3390/en12061048.

[22] M. Epstein, I. Vishnevetsky, A. Segal, and R. Rubin, "Research and Development in the Solar Research Facilities Unit of the Weizmann Institute of Science : Past , Present , and Future," no. December, 2014, doi: 10.18848/2325-1077/CGP/v09i04/55113.

[23] A. Segal, "Solar energy at high temperatures; researches at the Weizmann Institute of Science, Israel; 25 years of success," vol. 1, 2016, doi: 10.1051/rees/2016001.

[24] X. Wei, Z. Lu, W. Yu, and W. Xu, "Ray tracing and simulation for the beam-down solar concentrator," *Renew. Energy*, vol. 50, pp. 161–167, 2013, doi: 10.1016/j.renene.2012.06.029.

[25] A. Segal and M. Epstein, "The optics of the solar tower reflector," vol. 69, pp. 229–241, 2001.

[26] N. Calvet *et al.*, "The Masdar Institute solar platform : A new research facility in the UAE for development of CSP components and thermal energy storage systems.," vol. 100003, no. 2016, 2018, doi: 10.1063/1.4949191.

[27] D. Fontani, P. Sansoni, F. Francini, and D. Jafrancesco, "Optical approach to design a beam-down heliostats plant," vol. 160009, no. June 2017, 2018, doi: 10.1063/1.4984543.

[28] M. Diago *et al.*, "Where should beam down heliostat central rays intersect the final optical element axis ?," vol. 040012, no. November, 2018.

[29] S. Taramona, P. G.-G. Angel, J. V. Briongos, and J. Gomez-Hernandez, "Designing a flat beam-down linear Fresnel reflector," vol. 187, 2022, doi: 10.1016/j.renene.2022.01.104.

[30] D. Canavarro, G. Delgado, V. Patil, and M. Blanco, "Etendue-matched solar tower beam-down system for high-temperature industrial processes.," vol. 120005, no. May, 2022.

[31] M. Diago, N. Calvet, and P. R. Armstrong, "Net power maximization from a faceted beam-down solar concentrator," *Sol. Energy*, vol. 204, no. May, pp. 476–488, 2020, doi: 10.1016/j.solener.2020.04.061.

[32] M. Mokhtar, S. A. Meyers, P. R. Armstrong, and M. Chiesa, "Performance of a 100 kW th Concentrated Solar Beam-Down Optical Experiment," vol. 136, no. November 2014, pp. 1–8, 2016, doi: 10.1115/1.4027576.

[33] J. Gómez-Hernández, P. Á. González-Gómez, T. Ni-Song, J. V. Briongos, and D. Santana, "Design of a solar linear particle receiver placed at the ground level," vol. 170005, no. November 2018, 2019.

[34] S. Ihtsham, U. Haq, A. K. Khlief, H. H. Al-kayiem, and B. Ali, "OPTICAL ANALYSIS OF VARIOUS REFLECTORS APPLIED IN SOLAR BEAM DOWN TOWER," no. January, 2016.

[35] F. Z. Ahmed and R. C. Bansal, *HANDBOOK OF RENEWABLE ENERGY TECHNOLOGY*. World Scientific Publishing Co. Pte. Ltd., 2011.

[36] S. Kalogirou, *Solar_Energy_Engineering-Processes_and_Systems*, First edi. Elsevier, 2009.

[37] J. A. Duffie and W. A. Beckman, *Solar Engineering of Thermal Processes*, Fourth Edi. John Wiley & Sons, Inc., Hoboken, New Jersey.

[38] S. L. Lutchman, "Heliostat Field Layout Optimization for a Central Receiver," 2014.

[39] A. Yogev, A. Kribus, and M. Epstein, "SOLAR ' TOWER REFLECTOR ' SYSTEMS : A NEW APPROACH SOLAR PLANTS," vol. 23, no. 4, pp. 239–245, 1998.

[40] A. R. I. Rabl, "Tower reflector for solar power plant," vol. 18, no. 4, pp. 269–271, 1976.

[41] -, "Design of Solar Thermal Power Plants," Elsevier, Inc. under an exclusive license with Chemical Industry Press., 2019, pp. 1–46.

[42] E. M. Getie, "Poverty of Energy and Its Impact on Living Standards in Ethiopia," vol. 2020, 2020.

[43] V. V. Mukkoti, "DESIGN OF CONCENTRATED PARABOLIC DISH COLLECTOR FOR VAPOUR ABSORPTION REFRIGERATION," no. February, 2018.

[44] W. B. Stine and D. Ph, "A Compendium of Solar Dish / Stirling Technology," 1994.

[45] A. Z. Hafez, A. Soliman, K. A. El-metwally, and I. M. Ismail, "Solar parabolic dish Stirling engine system design, simulation, and thermal analysis.," no. August, 2016, doi: 10.1016/j.enconman.2016.07.067.

[46] J. J. O'Gallagher, *Nonimaging Optics in Solar Energy*, ISSN 1942-. Morgan & Claypool Publishers series, 2008.

[47] T. Keck, G. Weinrebe, and M. Balz, "Key aspects of cost-effective collector and solar field design," no. May, 2016, doi: 10.1063/1.4949051.

[48] W. P. Limited, *Concentrating solar power technology Related titles :* 2012.

[49] D. G. Thombare and S. K. Verma, "Technological development in the Stirling cycle engines," vol. 12, pp. 1–38, 2008, doi: 10.1016/j.rser.2006.07.001.

[50] A. Der Minassians, “Stirling Engines for Low-Temperature Solar-Thermal- Electric Power Generation,” 2007.

[51] H. Karabulut, E. C.Çınar, O. Rk, and H. S. Yucesu, “Torque and power characteristics of a helium charged Stirling engine with a lever controlled displacer driving mechanism,” vol. l, pp. 138–143, 2010, doi: 10.1016/j.renene.2009.04.023.

[52] U. of E. & T. L. Design Engineering Technical Section, ASME UET Lahore, “A review of operation and calculations for a Solar-Powered beta-type stirling engine,” ASME UET Lahore.

[53] K. Wang, S. R. Sanders, S. Dubey, F. Hoong, and F. Duan, “Stirling cycle engines for recovering low and moderate temperature heat : A review,” *Renew. Sustain. Energy Rev.*, vol. 62, pp. 89–108, 2016, doi: 10.1016/j.rser.2016.04.031.

[54] D. Thombare, “Stirling Engine Micro-CHP System,” no. January 2008, 2014.

[55] S. Edition, “Stirling Engine Design Manual Conservation and Renewable Energy.”

[56] M. H. Ahmadi, M. A. Ahmadi, M. Mehrpooya, and R. Energies, “Investigation of the effect of design parameters on power output and thermal efficiency of a Stirling engine by thermodynamic analysis,” pp. 1–16, 2014, doi: 10.1093/ijlct/ctu030.

[57] S. Narayan and V. Gupta, “OVERVIEW OF WORKING OF STIRLING ENGINES,” vol. 21, no. 4, pp. 45–53, 2015.

[58] V. Thakkar, A. Doshi, and A. Rana, “Performance Analysis Methodology for Parabolic Dish Solar Concentrators for Process Heating Using Thermic Fluid,” no. October, 2019, doi: 10.9790/1684-1212101114.

[59] A. Kribus, D. Kaftori, G. Mittelman, A. Hirshfeld, Y. Flitsanov, and A. Dayan, “A miniature concentrating photovoltaic and thermal system,” vol. 47, pp. 3582–3590, 2006, doi: 10.1016/j.enconman.2006.01.013.

[60] S. Yang, J. Wang, P. D. Lund, C. Jiang, and D. Liu, “Assessing the impact of optical errors in a novel 2-stage dish concentrator using Monte-Carlo ray-tracing simulation,” *Renew. Energy*, 2018, doi: 10.1016/j.renene.2018.02.034.

[61] S. Wu, L. Xiao, Y. Cao, and Y. Li, “A parabolic dish / AMTEC solar thermal power system

and its performance evaluation," *Appl. Energy*, vol. 87, no. 2, pp. 452–462, 2010, doi: 10.1016/j.apenergy.2009.08.041.

[62] J. C. Livengood, A. R. Rogowski, and C. F. Taylor, "THE VOLUMETRIC EFFICIENCY OF FOUR-STROKE ENGINES," vol. 6, no. 4, pp. 617–636, 2018.

[63] H. Merarda, M. Aksas, and T. Andrianne, "Shape effects on aerodynamic loading of heliostats," vol. 614, pp. 1–16, 2020.

[64] W. B. Stine and M. Geyer, "PowerFromTheSun.net," 2001. https://www.powerfromthesun.net/book.html (accessed Nov. 08, 2022).

[65] D. Y. . et. al. Goswami, *"Energy Conversion" Mechanical Engineering Handbook*. CRC Press LLC, 1999.

[66] T. M. P. Nguyen, "Lead acid batteries in extreme conditions: accelerated charge, maintaining the charge with imposed low current, polarity inversions. Introducing non-conventional charge.," 2009.

[67] Victron Energy B.V. | De Paal 35 | 1351 JG Almere | The Netherlands, "Gel and AGM Batteries." [Online]. Available: www.victronenergy.com.

[68] I. E. A. Task and I. I. I. Report, "Lead-Acid Battery Guide for Stand-Alone Photovoltaic Systems," vol. 1, no. December, pp. 1–33, 1999.

[69] A. Al-karaghouli and L. L. Kazmerski, "Optimization and life-cycle cost of health clinic PV system for a rural area in southern Iraq using HOMER software," *Sol. Energy*, vol. 84, no. 4, pp. 710–714, 2010, doi: 10.1016/j.solener.2010.01.024.

[70] G. Bekele and B. Palm, "Feasibility study for a standalone solar – wind-based hybrid energy system for application in Ethiopia," *Appl. Energy*, vol. 87, no. 2, pp. 487–495, 2010, doi: 10.1016/j.apenergy.2009.06.006.

[71] "2010 Solar Technologies Market Report," no. November, 2011.

[72] A. Chaurey and T. C. Kandpal, "A techno-economic comparison of rural electrification based on solar home systems and PV microgrids," *Energy Policy*, vol. 38, no. 6, pp. 3118–3129, 2010, doi: 10.1016/j.enpol.2010.01.052.

[73] H. E. E. CORPORATION, "Lead-acid Battery Handbook," pp. 1–23.

[74] M. J. Blanco, P. Garcia, and R. Gastesi, “Preliminary validation of Tonatiuh,” 2009, no. June 2021.

[75] L. Blank and A. Tarquin, *Engineering economy*, Seventh. .

[76] G. Cac, “Concentrated solar power plants : Review and design methodology,” vol. 22, pp. 466–481, 2013, doi: 10.1016/j.rser.2013.01.032.

[77] M. Abbas, B. Boumeddane, N. Said, and A. Chikouche, “Dish Stirling technology : A 100 MW solar power plant using hydrogen for Algeria,” *Int. J. Hydrogen Energy*, vol. 36, no. 7, pp. 4305–4314, 2011, doi: 10.1016/j.ijhydene.2010.12.114.

[78] P. Daniel and T. Arriola, “Technical , Economic , and Environmental Feasibility Analysis of a Small Scale CSP Desalination Plant in Sonora , Mexico by,” no. April, 2017.

[79] J. Coventry, J. Campbell, Y. Xue, and C. J. Hall, “Heliostat Cost Down Scoping Study Final Report,” no. December, 2016.

[80] T. Mekonnen, R. Bhandari, and V. Ramayya, “Islanded Solar PV Systems for the Ethiopian Residential Sector : Considering an Emerging Utility Tariff Plan for 2021,” 2021.

[81] A. Aly, A. Bernardos, C. M. Fernandez-peruchena, S. Solvang, and A. B. Pedersen, “Is Concentrated Solar Power (CSP) a feasible option for Sub-Saharan Africa?: Investigating the techno-economic feasibility of CSP in Tanzania,” *Renew. Energy*, 2018, doi: 10.1016/j.renene.2018.09.065.

APPENDIX

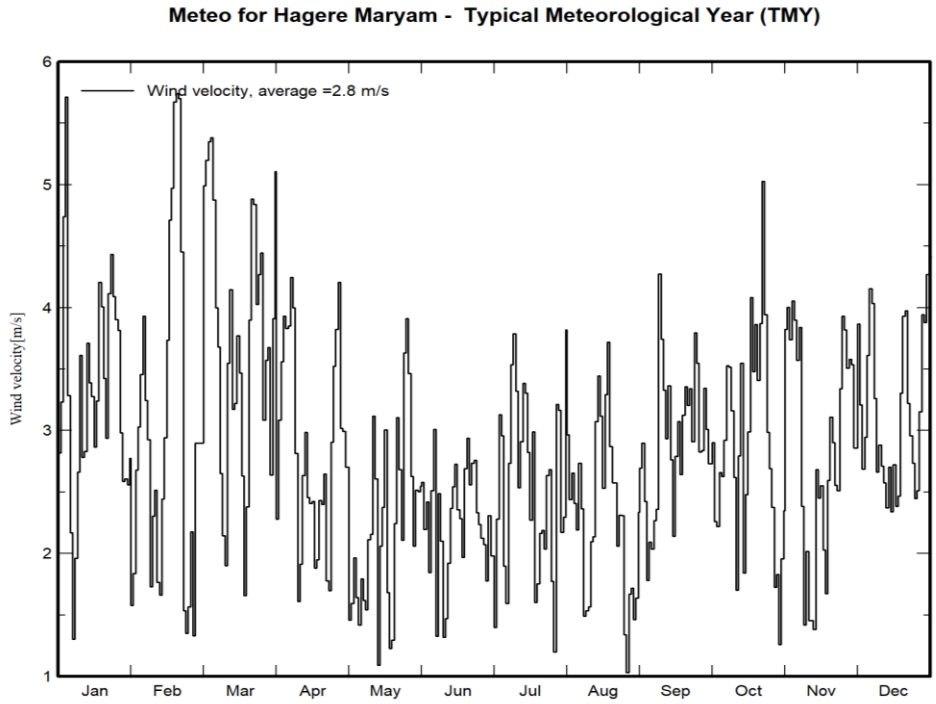

Figure A1: Daily wind speed.

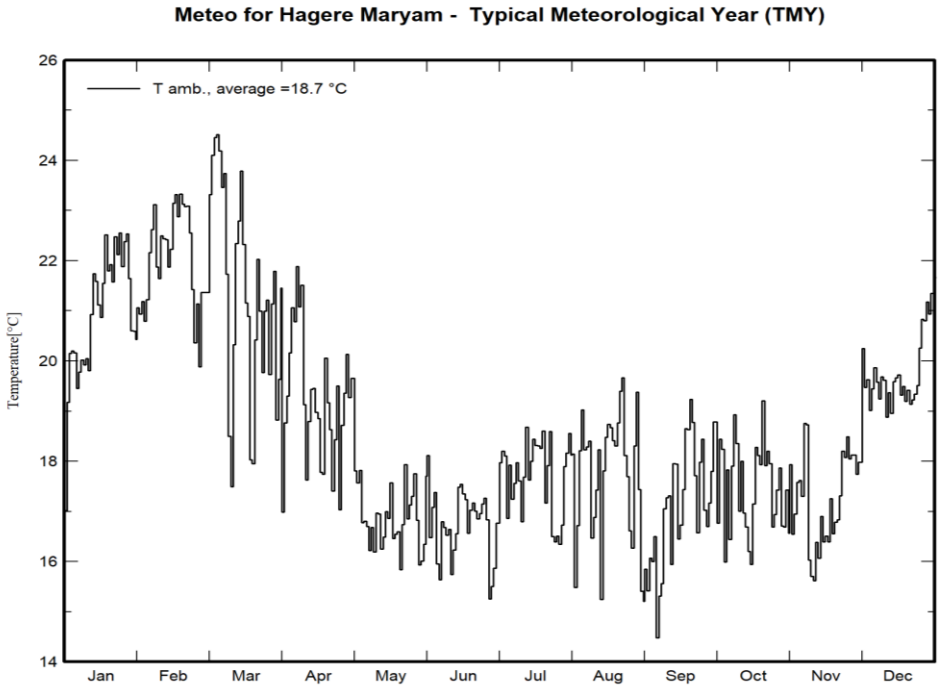

Figure A2: Daily temperature.

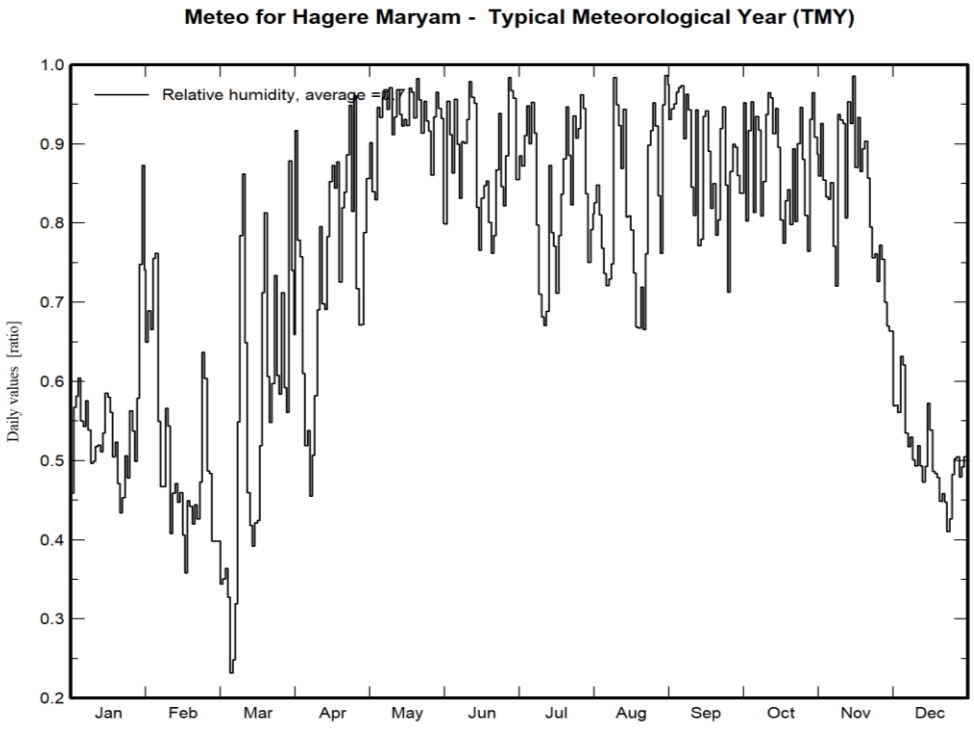

Figure A3: Relative humidity

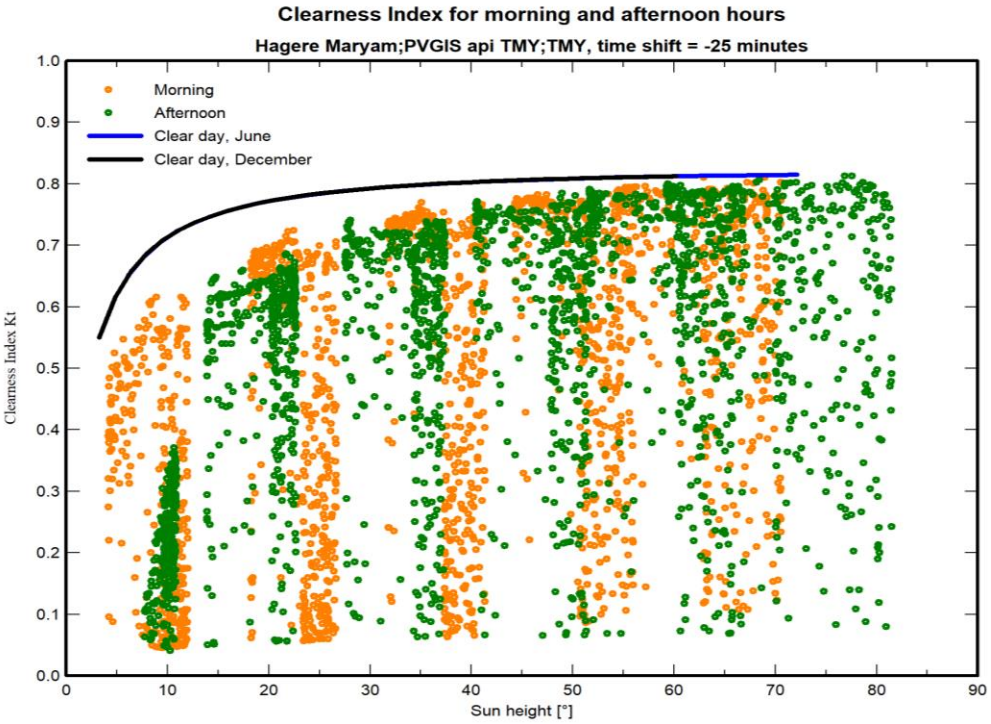

Figure A4: Clearness for morning and afternoon.

Table A1: The summary of "***United Stirling 4-95 MKII Stirling engine***" data.

DESIGN		
	Power (rated)	25 kW @ 1800 rpm (52 kW @ 4,000 rpm)
	Number of Cylinders	4, parallel in square configuration
	Stirling Configuration	Four-piston, double-acting
	Displaced Volume*	4 x 95 cm^3
	Swept Volume*	540 cm^3
	Bore	55 mm
	Stroke	40 mm
	Heater	4 x 18 tubes @ 260 mm long, 3 mm diameter
	Regenerators	4 x 2 @ 44 mm long, 57 mm diameter, holding 200 mesh stainless steel wire screens.
	Cooler	4 x 2 x 200 tubes, 90 mm long
	Cooling System	Glycol-water / forced-air radiator
	Drive Mechanism	Dual crankshafts with crossheads driving single contra-rotating output shaft.
	Working Gas	Hydrogen (helium optional)
	Mean Gas Pressure (max.)	20 MPa
	Gas Containment	Leningrader piston rod seal (preloaded trapezoidal Rulon™ ring)
	Gas Temperature (high)	720°C
	Coolant Temperature (max.)	50°C
	Power Control	Variable working gas pressure
	Envelope (including receiver)	Length - 550 mm
		Width - 450 mm
		Height - 400 mm
		Weight - 330 kg
ALTERNATOR/GENERATOR		
	Type	Induction Motor/Generator
	Manufacturer	Reliance Electric
	Rating	22.5 kW @ 1800 rpm, 480 Vac, 60 Hz, 0.90 pf
PERFORMANCE		
	Output (electrical)	27.1 kW_e @ 1800 rpm / 1000 W/m^2
	Efficiency	41% @ 1800 rpm (engine/alternator)
	Year	1984
	Number Built	Numerous, approx. 15 for solar applications
	Manufacturer	United Stirling of Sweden AB, Malmö, Sweden

The general outlook of tonatiuh

The interface of Tonatiuh is similar to CAD programs. In Figure (A.6), the general outlook of Tonatiuh with a beam-down model is shown.

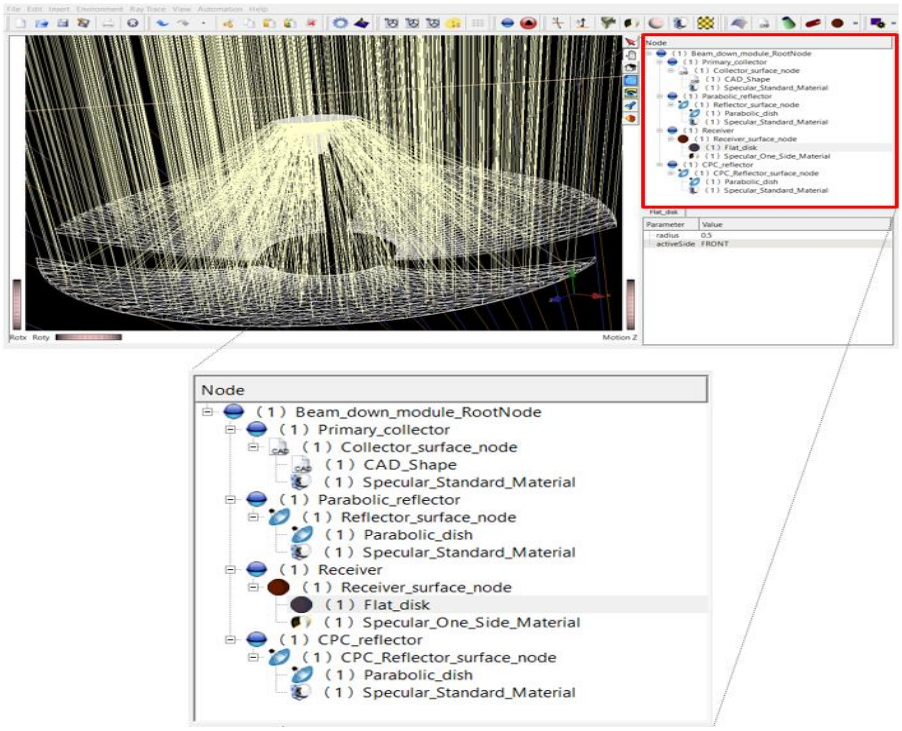

Figure A.6: The general outlook of tonatiuh, and zoom out tree structure, to create a power module.

Defining shapes

First, a group node, called the “Primary collector,” is created for the collector mirror. The primary collector is created by solid work_2014, and transported to tonatiuh. Then, a surface node, called the “Collector Surface node” is defined under the group node. Finally, the shape and the material for the surface node are implemented. Again, to create the secondary parabolic reflector, compound parabolic collector (CPC), and receiver plane the same procedure is followed.

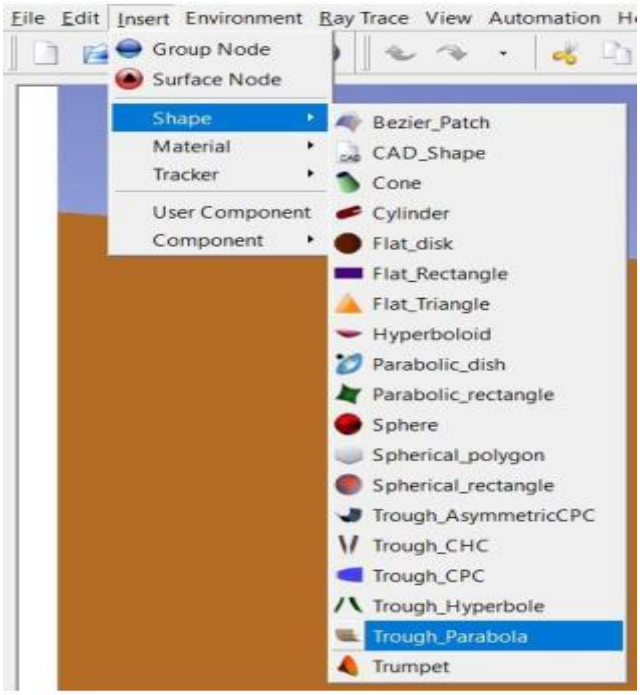

(a)

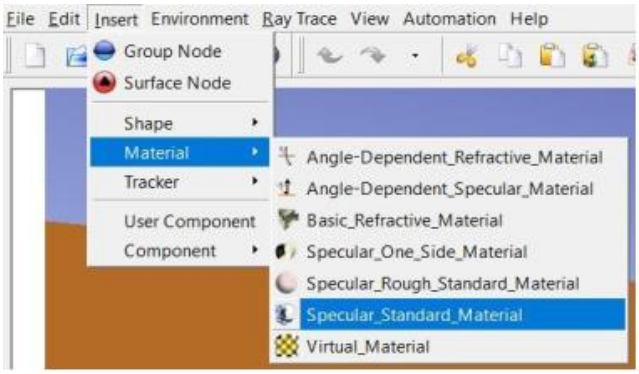

(b)

Figure A.7: (a). Shapes node, and (b). Material node; insertion windows.

Environment definition

After defining the geometry, and the materials for each component of the model. Under this section, the Sunlight must be introduced. (See Figure A.8).

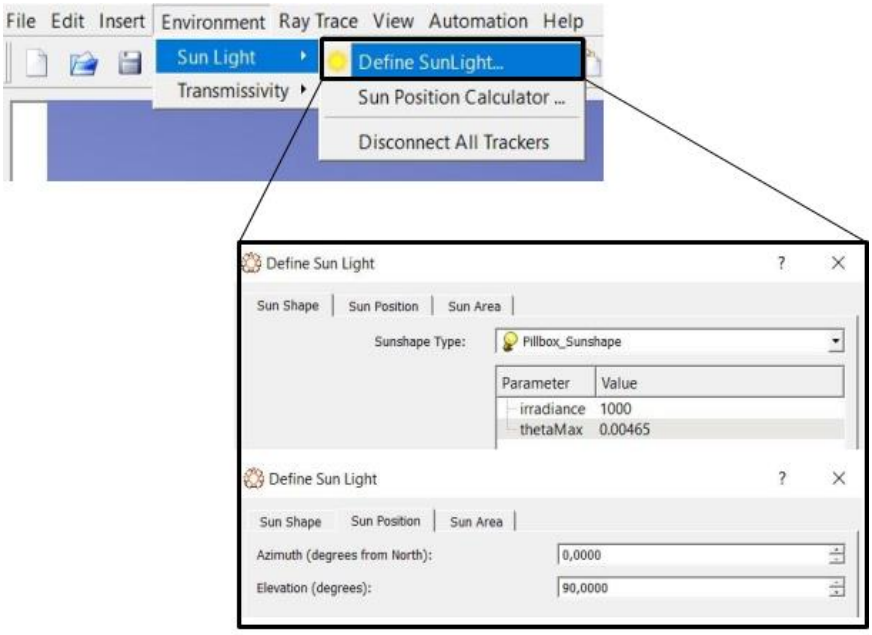

Figure A.8: Define SunLight window.

As shown in Figure under environment, the "Define SunLight" option allows users to manually enter the parameters (Sun shape, DNI, azimuth angle, angle of incidence, etc.). Therefore, it is used for the Sun definition. Note that, the "Sun Position Calculator" in Figure (A.8) is also quite useful since it allows users to select the location and time on Earth directly.

Number of Rays

After all the above has been done, the number of rays must be determined to start the ray-tracing simulation. Tonatiuh uses the MCRT method, which is a stochastic approach. Therefore, one has to make sure that the number of rays used is good enough so that the total solar irradiation on the absorber surface can be accurately calculated.

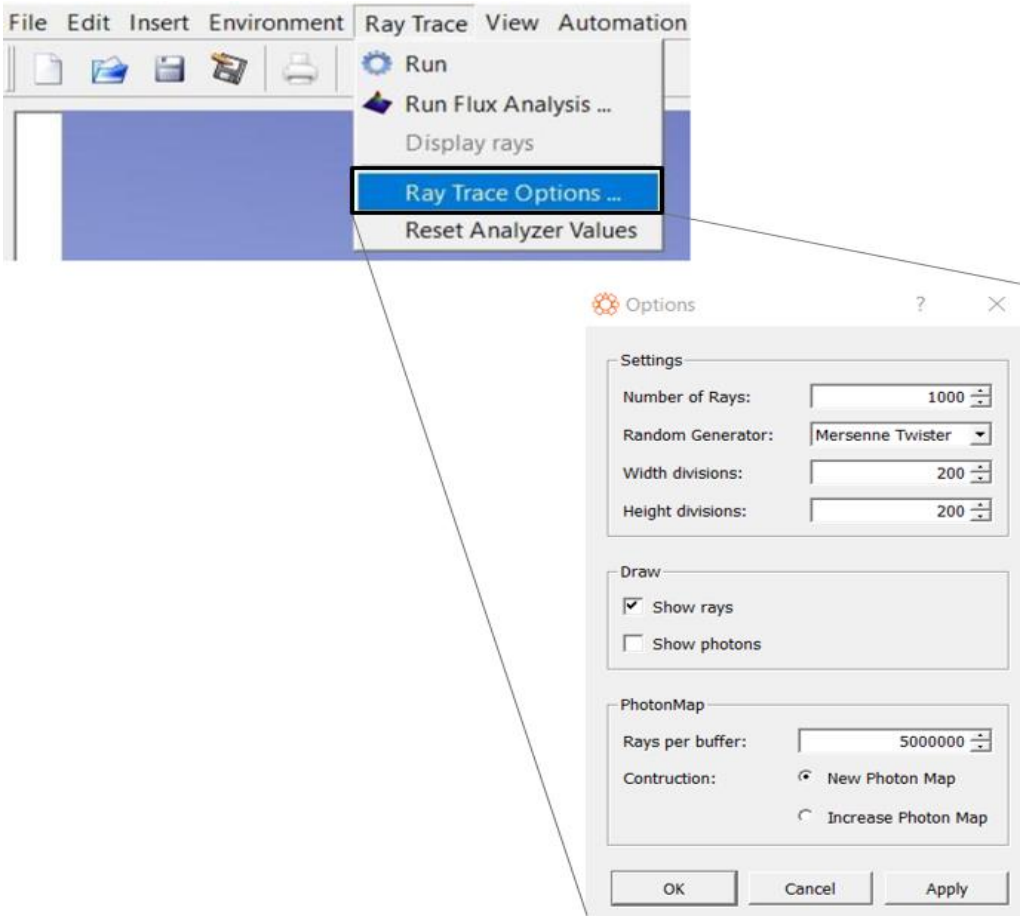

Figure A.9: The ray-trace options.

In Figure A.9, Mersenne Twister is chosen as a “Random Generator”. Hundreds million, which can be changed by the user, is entered for “Number of Rays”.

Finally, the ray tracing simulation is run to collect the tracing result. (See Figure A.10, A.11 & A.12).

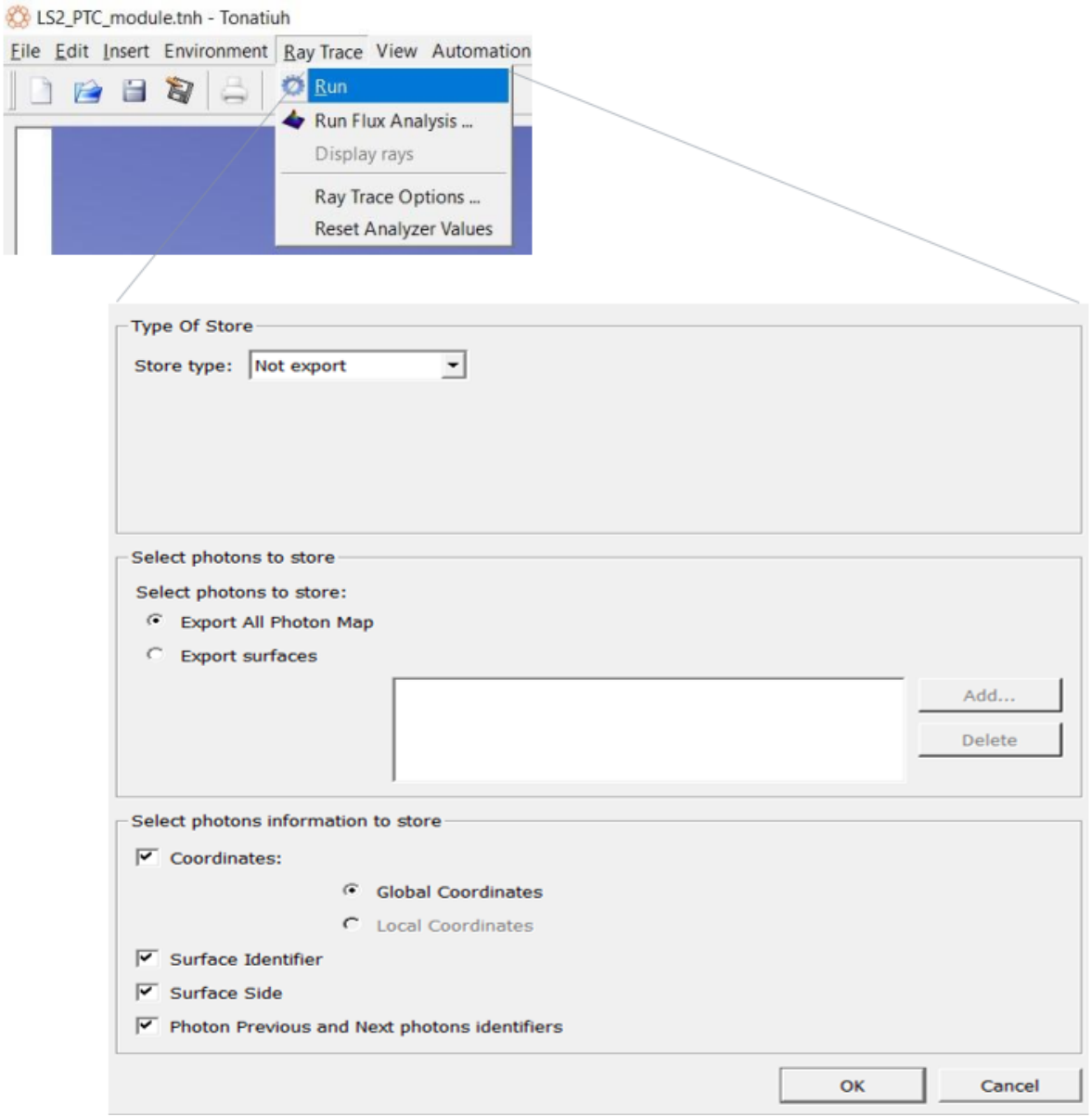

Figure A.10: Final simulator button.

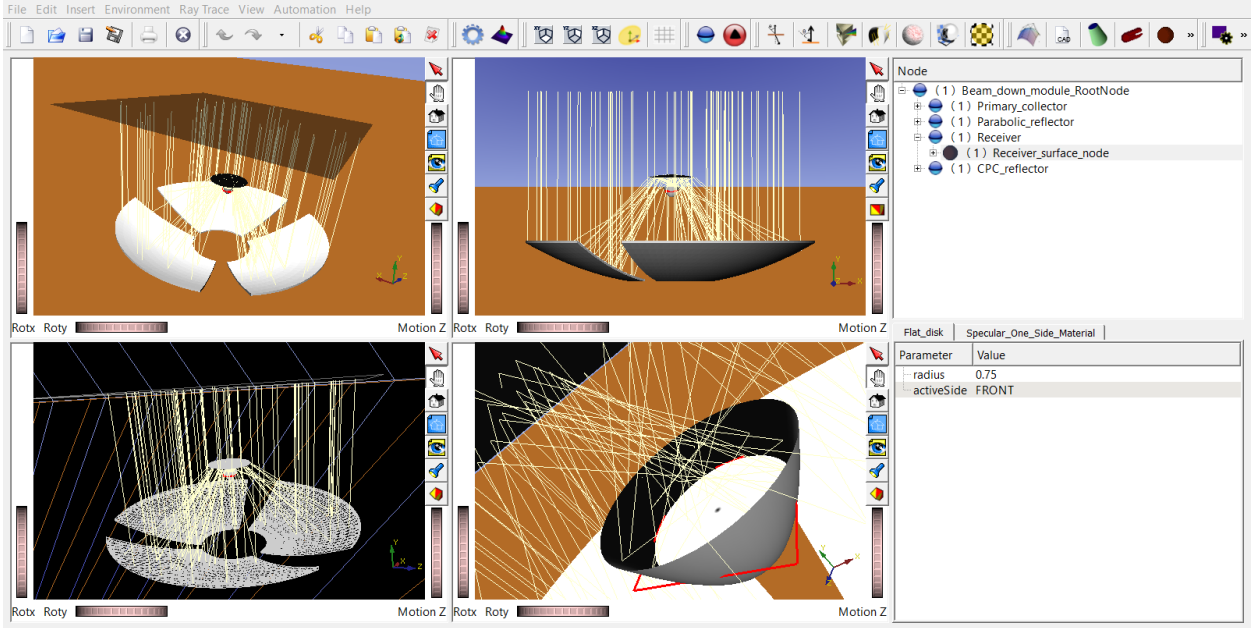

Figure A.11. Multi-view.

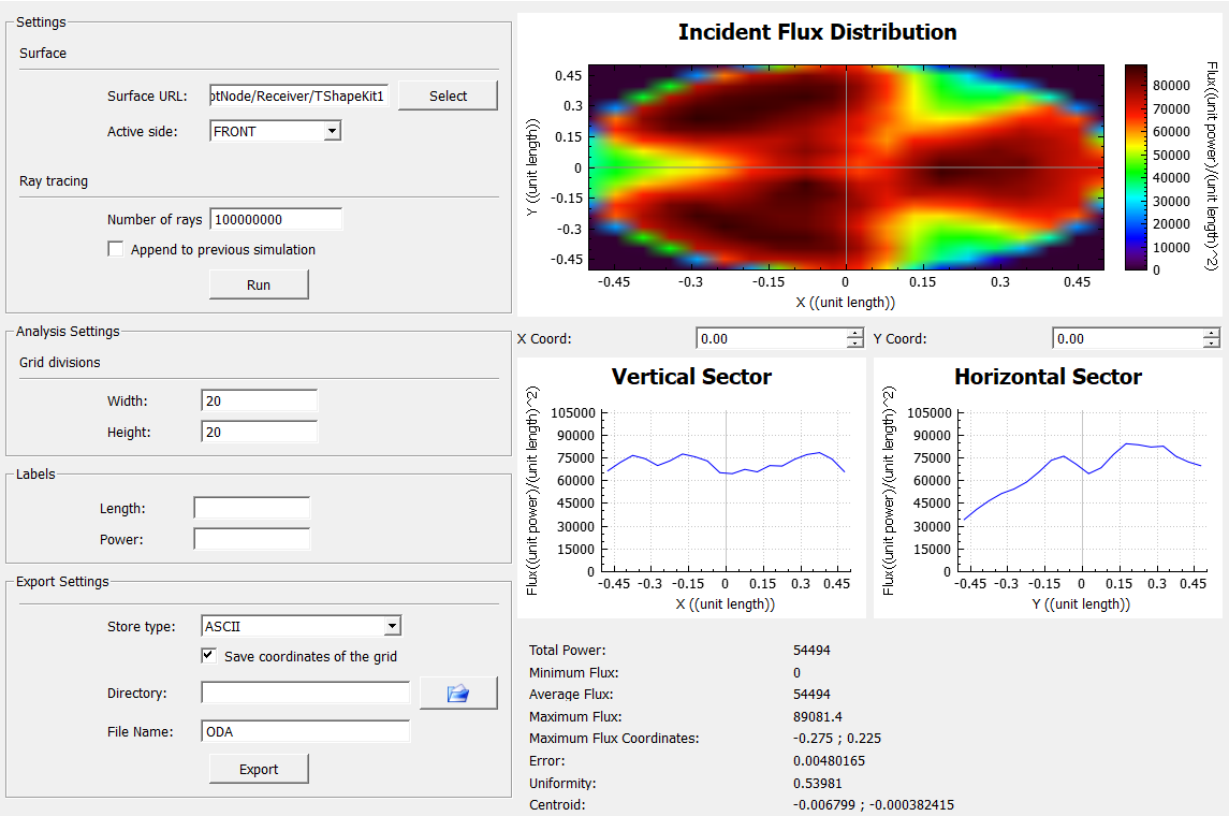

Figure A.12: The receiver is not at the optimum position.